Dissertation
submitted to the
Combined Faculties for the Natural Sciences and for Mathematics
of the Ruperto-Carola University of Heidelberg, Germany
for the degree of
Doctor of Natural Sciences

Presented by
Dipl.-Phys. *Frank Bigiel*
born in Augsburg, Germany

Oral examination: 27.06.2008

The Spatially Resolved Star Formation Law in Nearby Galaxies

Referees: Prof. Dr. Ralf S. Klessen
Dr. Fabian Walter

Abstract

This thesis presents a comprehensive analysis of the relationship between gas and star formation (SF) at sub-kpc resolution in a large sample of nearby galaxies. The analysis is based on recent very high quality radio, infrared and UV data. Key to this thesis are new, sensitive and high resolution atomic gas maps from 'The HI Nearby Galaxy Survey' (THINGS). A combination of these multiwavelength data are used to study the gas-SF relation across the H_2–dominated centers of the spirals as well as their HI–dominated outskirts and HI–rich late type/dwarf galaxies.

For the spiral galaxies, a Schmidt-type power law with index $N = 1.0 \pm 0.2$ relates star formation rate and H_2. This implies that H_2 forms stars at a constant efficiency, i.e. star formation rate per unit gas, in spirals. Most galaxies show little or no correlation between the star formation rate and HI. The star formation efficiency is observed to decrease with increasing radius in the spirals, while the dwarf galaxies in our sample display star formation efficiencies similar to those found in the outer optical disks of the spirals. There is a sharp saturation of HI at a certain column density in both the spiral and dwarf galaxies. In the case of spirals, gas in excess of this limit is observed to be molecular.

The decreasing star formation efficiency is observed to extend smoothly from the optical disk into the outskirts of galaxies. In this outer regime, SF is observed to decline 4 times more quickly than HI. As a result, the time that it takes SF to consume the gas reservoir is $\sim$10 times longer in the outer disks, corresponding to about a Hubble time, than in the centers of spiral galaxies. For very low HI columns, which are typically found at large radii, the depletion time is even longer, suggesting that SF at such low HI columns may be suppressed by inhospitable conditions in the interstellar medium.

Zusammenfassung

Im Rahmen der vorliegenden Doktorarbeit wurde mittels neuer Radio-, Infrarot- und UV-Daten eine umfassende Analyse der Beziehung zwischen Gas und Sternentstehung auf Skalen unterhalb eines Kiloparsecs in einer grossen Anzahl naher Galaxien durchgeführt. Entscheidend für die Ergebnisse dieser Arbeit sind hochauflösende Radiokarten des atomaren Wasserstoffs (HI), die im Rahmen des 'THINGS' Projekts gewonnen wurden ('The HI Nearby Galaxy Survey'). Durch kombinieren dieser Daten verschiedener Wellenlängen konnte die Beziehung zwischen dem Gas und Sternentstehung, ausgehend von den von molekularem Wasserstoffgas (H_2) dominierten Zentren der Spiralgalaxien bis in die von HI dominierten Aussenbereiche (sowie in den HI dominierten Zwerggalaxien), untersucht werden.

In den Spiralgalaxien zeigt sich, dass die Sternentstehungsrate mit dem molekularen Wasserstoffgas über ein Potenzgesetz ('Schmidt Gesetz') mit einem Exponenten $N = 1.0 \pm 0.2$ verbunden ist. Daraus folgt, dass in den Spiralgalaxien H_2 mit konstanter Effizienz in Sterne umgewandelt wird. HI ist jedoch für die meisten Galaxien nicht mit der Sternentstehungsrate korreliert. Es zeigt sich, dass die Effizienz mit der in Spiralgalaxien Gas in Sterne umgewandelt wird mit zunehmendem Abstand vom Zentrum der Galaxie abnimmt. Die Effizienz der Sternentstehung in Zwerggalaxien ist dabei ähnlich zu jener in den äusseren Bereichen der stellaren Scheiben von Spiralgalaxien. Es zeigt sich ferner ein deutlicher Sättigungseffekt des atomaren Wasserstoffs bei einer bestimmten HI Säulendichte, und zwar in Spiral- und Zwerggalaxien gleichermassen. Oberhalb dieser Schwelle kommt das Wasserstoffgas fast ausschliesslich in molekularer Form vor.

Die abnehmende Effizienz der Sternentstehung setzt sich bis in die Aussenbereiche der Galaxien fort. In diesen Aussenbereichen nimmt die Sternentstehungsrate etwa vier mal so schnell ab wie der atomare Wasserstoff. Das führt dazu, dass die Zeit, die benötigt würde um den gesamten Vorrat an Gas in Sterne umzuwandeln, in den Aussenbereichen etwa einen Faktor 10 länger ist, entsprechend etwa einer Hubble-Zeit, als in den Zentren der Spiralgalaxien. Diese Zeit ist nochmals erheblich grösser bei sehr grossen Abständen vom Zentrum der Galaxien für HI sehr niedriger Säulendichte. Dies legt nahe, dass unter solchen Bedingungen Sternentstehung vermutlich unterdrückt wird.

Contents

1 Introduction **1**
1.1 The Observed Star Formation Law in Nearby Galaxies 1
1.2 Simple Theoretical Expectations 3
1.3 Star Formation in Outer Disks 4
1.4 The Spatially Resolved Star Formation Law 5

2 THINGS - The HI Nearby Galaxy Survey **7**
2.1 The 21 cm Line 7
2.2 Pushing the Limits - The need for new HI Data on Nearby Galaxies . 8
2.3 Survey Parameters 10
2.4 Data Reduction 15
2.4.1 From Observations to Data Cubes 15
2.4.2 Getting nice Images - 'Cleaning' 17
2.4.3 Last Steps and Final Data Products 19

3 Ancillary Data **25**
3.1 CO Data 25
3.2 Deriving total Gas Maps 27
3.3 GALEX FUV Data 28
3.4 *Spitzer* Space Telescope 24 μm Data 29
3.5 Star Formation Rate Surface Density Maps 30

4 The Resolved Star Formation Law in Optical Disks **31**
4.1 Sample, Data, Units, and Measurements 32
4.1.1 Sample 32
4.1.2 Alignment, Units, and Convolution 32
4.1.3 Gas Surface Density Maps 34
4.1.4 Individual Data Points 34
4.1.5 Radial Profiles 38
4.2 The Star Formation Law in Individual Galaxies 38
4.2.1 Fits To $\Sigma_{\rm SFR}$ Versus $\Sigma_{\rm gas}$ 41
4.2.2 The Molecular Gas Schmidt Law 45
4.2.3 The Total Gas Schmidt Law 45
4.2.4 Star Formation Efficiencies 46
4.2.5 HI Saturation at High Column Densities 46
4.2.6 $\Sigma_{\rm SFR}$ vs. $\Sigma_{\rm gas}$ in HI-dominated Galaxies 47
4.2.7 Dependence on Resolution 47

4.3 Combined Distributions 49
4.3.1 HI Saturation in the Combined Distribution 53
4.3.2 HI, H_2, Total Gas, and the Star Formation Law 53
4.3.3 Comparison With Measurements Integrated Over Galaxy Disks 55
4.3.4 The Combined Molecular Schmidt Law 56
4.4 The SF Law and Environment 56
4.4.1 The Radial Dependence of the SFE 58
4.4.2 HI-dominated Galaxies and the Outer Disks of Spirals 59
4.4.3 The Molecular-to-Atomic Gas Ratio Σ_{H2} /Σ_{HI} as a Function of Radius 62
4.5 Summary & Discussion 63
4.5.1 Results 63
4.5.2 The Molecular Schmidt Law In Various Regimes 64

5 Gas and Star Formation in Outer Disks 67
5.1 Data 67
5.2 Deriving SFRs in the Outer Disks 68
5.2.1 Gas Column based Extinction Estimate for the Outer Disks . 70
5.3 Results 71
5.3.1 Outer Disk Profiles 71
5.3.2 Radial Profiles and Exponential Scalelengths 76
5.3.3 Rank Correlation 79
5.3.4 Σ_{SFR}–Σ_{gas} Scaling 81
5.3.5 The Star Formation Law in Outer Disks 85
5.3.6 Comparison to Measurements from inside r_{25} 91
5.4 Summary & Discussion 93

6 Summary 95

7 Outlook 97
7.1 Star Formation in the Outskirts of Galaxies 97
7.2 The Star Formation Law in Starbursts and (U)LIRGs 98

Acknowledgments 107

List of Figures

1.1 The Kennicutt Law 2
1.2 The star formation law from radial profiles 3
1.3 The star formation law in outer disks 5

2.1 The VLA 9
2.2 The THINGS sample 11
2.3 Exploring the ROBUST parameter 17
2.4 HI line spectra for NGC 2403 and IC 2574 18
2.5 Channel maps for NGC 6946 21
2.6 Channel maps for Ho II 22
2.7 Moment maps for NGC 6946 23
2.8 Moment maps for Ho II 24

3.1 The IRAM 30 m telescope 26
3.2 HERA CO intensity maps 27
3.3 HERA channel maps for NGC 6946 28

4.1 $\Sigma_{\rm HI}$ and $\Sigma_{\rm SFR}$ maps 35
4.2 Radial profiles for the spiral galaxies 39
4.3 Radial profiles for the HI-dominated galaxies 40
4.4 $\Sigma_{\rm SFR}$-$\Sigma_{\rm gas}$ scatter plots for individual galaxies 42
4.5 $\Sigma_{\rm SFR}$-$\Sigma_{\rm HI}$ scatter plots for HI- dominated galaxies 48
4.6 Resolution effects on pixel-by-pixel distributions 50
4.7 Resolution effects on power law fits 52
4.8 Results pixel-by-pixel analysis for the entire sample 54
4.9 Comparison pixel-by-pixel data to data from K98 55
4.10 Molecular gas Schmidt law and Monte Carlo realizations 57
4.11 Pixel-by-pixel: Variation of the SFE with radius I 59
4.12 Pixel-by-pixel: Variation of the SFE with radius II 60
4.13 Pixel-by-pixel: dwarfs compared to the outer disks of spirals 61
4.14 $\Sigma_{\rm H2}/\Sigma_{\rm HI}$ as a function of radius 62

5.1 Illustrating the outer disk regime 68
5.2 Radial Profiles 72
5.3 $\Sigma_{\rm SFR}$ versus $\Sigma_{\rm gas}$ scalelengths 78
5.4 Radial variation of the correlation coefficient for the spirals 80
5.5 Radial variation of the correlation coefficient for the spirals 82
5.6 $\Sigma_{\rm SFR}$ binned by $\Sigma_{\rm gas}$ 83

5.7 $\Sigma_{\rm gas}$ histograms for different radial regimes 84
5.8 SFE binned by $\Sigma_{\rm gas}$ for different radial regimes 85
5.9 Pixel-by-pixel plot for $\Sigma_{\rm SFR}$ versus $\Sigma_{\rm gas}$ in the outer disks 86
5.10 Pixel-by-pixel plot for $\Sigma_{\rm SFR}$ versus $\Sigma_{\rm gas}$ in the outer disks of spirals segregated by radius 88
5.11 Pixel-by-pixel plot for $\Sigma_{\rm SFR}$ versus $\Sigma_{\rm gas}$ in the outer disks of dwarfs segregated by radius 89
5.12 Power-law fit to pixel-by-pixel outer disk data 90
5.13 Optical disk versus outer disk pixel-by-pixel for the spirals 91
5.14 Optical disk versus outer disk pixel-by-pixel for the dwarfs 92

7.1 THINGS HI versus deep GALEX UV for M 83 98
7.2 Σ_{SFR}-Σ_{gas} phase space 99

List of Tables

2.1 THINGS galaxy sample 13

4.1 Resolved star formation law galaxy sample 33
4.2 Fitted power-law parameters at 750 pc resolution 44

5.1 Outer disk galaxy sample 69
5.2 Fit results for the outer disk radial profiles 77

Chapter 1

Introduction

A robust, quantitative measurement of the relationship between star formation rate (SFR) and gas density, SF law, is of major astrophysical importance in the context of galaxy evolution: It describes how effectively galaxies turn their gas into stars and constrains theoretical models of star formation; it serves as essential input to simulations and models of galaxy evolution (e.g. Springel & Hernquist, 2003; Boissier & Prantzos, 1999; Tan et al., 1999; Krumholz & McKee, 2005; Matteucci et al., 2006). Direct observations of this relationship at sub-kiloparsec scales are still very rare, because measuring the distributions of star formation, atomic gas, and molecular gas at high resolution and sensitivity is challenging and expensive in terms of telescope time.

This is beginning to change. The past few years have seen an explosion in multiwavelength data for nearby galaxies. From the 'GALEX Nearby Galaxy Survey' (Gil de Paz et al., 2007) and the '*Spitzer* Infrared Nearby Galaxies Survey' (SINGS, Kennicutt et al., 2003) the distribution of star formation is now known in a large suite of local galaxies. From the 'BIMA Survey of Nearby Galaxies' (Helfer et al., 2003) and recent observations with the IRAM 30 telescope (Leroy et al., in prep.) the CO distributions of many nearby galaxies are also known (see § 3.1). With 'The HI Nearby Galaxy Survey' (THINGS, Walter et al., 2008, see § 2) the last critical piece is in place: HI maps that match or exceed the angular resolution and sensitivity of the ultraviolet, infrared, and CO data are now available for 34 nearby galaxies.

1.1 The Observed Star Formation Law in Nearby Galaxies

Following the pioneering work of Schmidt (1959), it is common to relate gas density to the SFR density using a power law. He suggested the form $\rho_{\rm SFR} \sim (\rho_{\rm gas})^{\rm N}$, where $\rho_{\rm SFR}$ and $\rho_{\rm gas}$ denote the *volume* densities of the SFR and the gas. Studying the distribution of HI and stars perpendicular to the galactic plane, he derived a power-law index of $N \approx 2$. Sanduleak (1969) and Hartwick (1971) carried out first measurements of the Schmidt law in other galaxies. They used bright stars in the Small Magellanic Cloud and HII regions in M31, respectively, to trace star formation

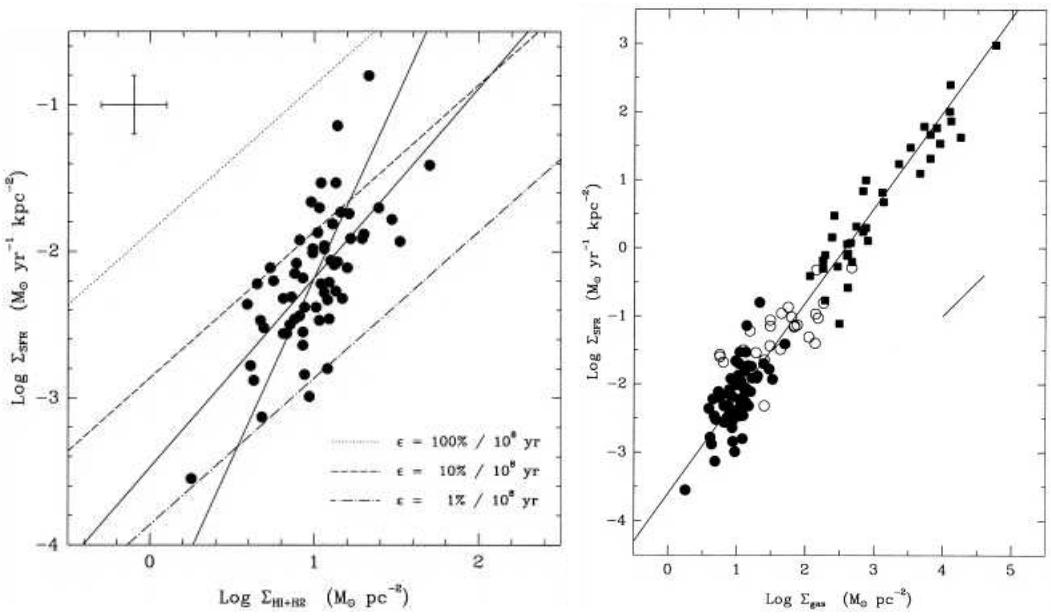

Figure 1.1: *Left:* Relation between the disk averaged $\Sigma_{\rm SFR}$ and $\Sigma_{\rm gas}$ for a sample of 61 nearby normally star forming spiral galaxies from Kennicutt (1998). The dashed and dotted lines indicate levels of constant star forming efficiency, $\Sigma_{\rm SFR}$ / $\Sigma_{\rm gas}$, and gas depletion timescales. The solid lines represent power-law fits to the data, whereas the steeper fit corresponds to the bisector slope of N≈2.47 quoted in the text. *Right:* The same relation for the composite sample of the 61 spirals (filled circles, also see left panel) and 31 infrared-selected starburst galaxies (squares), also from Kennicutt (1998). Datapoints representing the centers of the spirals are overplotted as open circles. The solid line represents a bisector fit which yields a slope of N≈1.4 (Figures from Kennicutt, 1998)

and focused their analyses on *surface* densities, $\Sigma_{\rm HI}$ and $\Sigma_{\rm SFR}$, which are directly observable. They found $N_{\rm SMC} = 1.84 \pm 0.14$ and $N_{\rm M31} = 3.50 \pm 0.12$.

Madore et al. (1974) compared stars and HII-regions to $\Sigma_{\rm HI}$ and derived different exponents as a function of radius in M33. Newton (1980) redid this analysis with higher-resolution HI data and also found a gradient of $N = 0.6 - 2.6$ with galactocentric radius. Tosa & Hamajima (1975) compared HII-regions to $\Sigma_{\rm HI}$ in M31 and the LMC, Hamajima & Tosa (1975) performed the same analysis in 7 nearby galaxies. They found radial variations in fitted power law indices N in the range 1.5-2.9.

Kennicutt (1989, 1998, hereafter K98) studied the globally averaged relationship between SFR and gas in a sample of 61 nearby normal spiral and 36 infrared-selected starburst galaxies. K98 showed that a Schmidt law relates the disk-averaged total gas surface density, $\Sigma_{\rm gas} = \Sigma_{\rm HI} + \Sigma_{\rm H2}$, to the disk-averaged star formation surface density, $\Sigma_{\rm SFR}$, over many orders of magnitudes. His subsample of normal spiral galaxies yields a power-law index $N = 2.47 \pm 0.39$; his composite sample, including the starburst galaxies, yields $N = 1.40 \pm 0.15$. These results from K98 are shown in Figure 1.1. Similar studies of the disk-averaged Schmidt Law used a range of

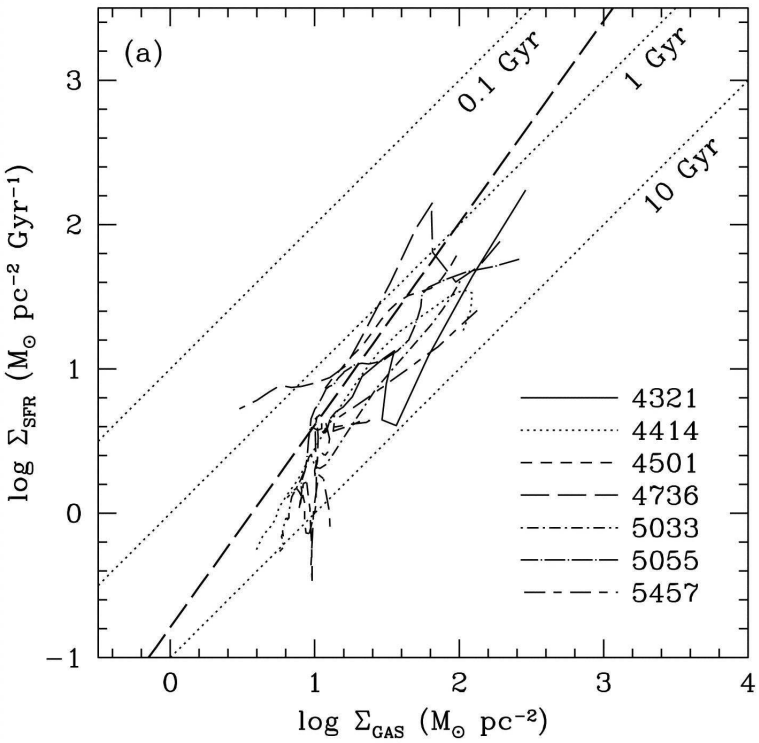

Figure 1.2: The $\Sigma_{\rm SFR}$ - $\Sigma_{\rm gas}$ relation for 6 nearby galaxies from Wong & Blitz (2002). Each line represents the radial profile datapoints for an individual galaxy. The thick dashed line shows the Schmidt Law as derived from Kennicutt (1998) with a power-law index of 1.4, which is in good agreement with the data. The dotted lines indicate levels of constant star forming efficiency and gas depletion time. (Figure from Wong & Blitz, 2002)

SFR tracers — such as Hα, UV, radio continuum, and FIR emission— and found $N = 0.9$ – 1.7 (e.g. Buat et al., 1989; Buat, 1992; Deharveng et al., 1994).

Other authors studied a local Schmidt law at higher resolutions using radial profiles (i.e. comparing azimuthally averaged values) of $\Sigma_{\rm SFR}$ and $\Sigma_{\rm gas}$. Wong & Blitz (2002) found $N = 1.2$ – 2.1 for 6 molecule-rich spiral galaxies (see Figure 1.2). Boissier et al. (2003) derived $N \approx 2$ for 16 galaxies and Misiriotis et al. (2006) obtained $N = 2.18 \pm 0.20$ for the Milky Way. Heyer et al. (2004) found $N = 3.3 \pm 0.1$ for M33, whereas Schuster et al. (2007) found $N = 1.4 \pm 0.6$ for M51.

1.2 Simple Theoretical Expectations

The large range of power-law indices in the literature, $N \approx 1$–3, suggests that either different star formation (SF) laws exist in different galaxies or N is very sensitive to systematic differences in methodology (e.g. the choice of SFR tracers, the spatial resolution of the data, etc.).

There are physically motivated, theoretical reasons to expect N in the range 0.75 – 2, and the precise value of N may vary with the regime one considers. Krumholz &

McKee (2005) argue that a giant molecular cloud (GMC) will convert its gas into stars over a free fall time, $t_{\rm ff} \propto \rho_{\rm gas}^{-0.5}$. If this is the case, then from the observation that the surface density of GMCs is constant (e.g. Solomon et al., 1987; Blitz et al., 2007), implying $\rho_{\rm gas} \propto M_{\rm GMC}^{-0.5}$, one expects $N \approx 0.75$ for the case where we measure the Schmidt law for individual GMCs. If we instead compare uniform populations of GMCs, where the different molecular gas surface densities reflect only different *numbers* of clouds (not different physical properties), then one expects $N \approx 1$ for the molecular gas exponent (assuming the population-averaged timescale over which a GMC converts its gas to stars is constant). If gravitational instability in the neutral (HI + H_2) ISM is the key process in star formation, the SFR may instead depend on the free-fall time of the *total* gas; in this case, if the gas scale height is constant, $t_{\rm ff} \propto \Sigma_{\rm gas}^{-0.5}$ and one would expect $N \approx 1.5$ (e.g. Madore, 1977). Finally, if one simply postulates that star formation is a fundamentally collisional process, e.g. because it depends on the formation of H_2 by collisions between hydrogen atoms and dust grains or the collision of small clouds to form larger clouds, one would expect $\rho_{\rm SFR} \propto \rho_{\rm gas}^2$, which will lead to $N \approx 2$ (again for a constant gas scale height system).

Another open question is whether the Schmidt law is fundamentally a molecular phenomenon or if a single, universal power law relates total gas and star formation. Because all stars are believed to form in molecular clouds, it would seem natural that H_2 and SFR are more immediately related than HI or total gas and SFR. Therefore it is is somewhat surprising that observations remain contradictory on this point. One of the most surprising findings by K98 was that $\Sigma_{\rm SFR}$ correlated better with $\Sigma_{\rm HI}$ than with $\Sigma_{\rm H2}$ in normal disks; the strongest correlation, between $\Sigma_{\rm SFR}$ and $\Sigma_{\rm gas}$, was only marginally stronger than the $\Sigma_{\rm SFR} - \Sigma_{\rm HI}$ correlation. Wong & Blitz (2002) found a much stronger relationship between $\Sigma_{\rm SFR}$ and $\Sigma_{\rm H2}$ than between $\Sigma_{\rm SFR}$ and $\Sigma_{\rm HI}$, even finding an anti-correlation between $\Sigma_{\rm SFR}$ and $\Sigma_{\rm HI}$ at high SFRs, but they focused on molecule-rich spirals and therefore did not include large amounts of the HI-dominated ISM. Even in H_2-rich spirals, the question is still open. Recently, Schuster et al. (2007) and Crosthwaite & Turner (2007) studied the molecule-rich spirals NGC 5194 and NGC 6946 and found that the total gas correlates better with the SFR than H_2 alone.

1.3 Star Formation in Outer Disks

Lower metallicities, less dust, higher rotation velocities (and shear in spirals) as well as the rarefied HI make the outer disks of galaxies a distinctly different environment as compared to the optical disks. The relatively recent discovery of wide spread recent star formation (SF), extending significantly beyond the optical disks and reaching far into the outer (extended HI) disks of galaxies, was one of the major achievements of the GALEX mission (Thilker et al., 2005; Gil de Paz et al., 2005; Thilker et al., 2007; Gil de Paz et al., 2007; Boissier et al., 2007). Also Hα and optical broad brand observations revealed populations of young stars in outer disks (Ferguson et al., 1998; Lelièvre & Roy, 2000; Cuillandre et al., 2001; de Blok & Walter, 2003). SF at large galactocentric radii, despite potentially low SF rates, should also result in chemical evolution and enrichment of outer disks. This agrees

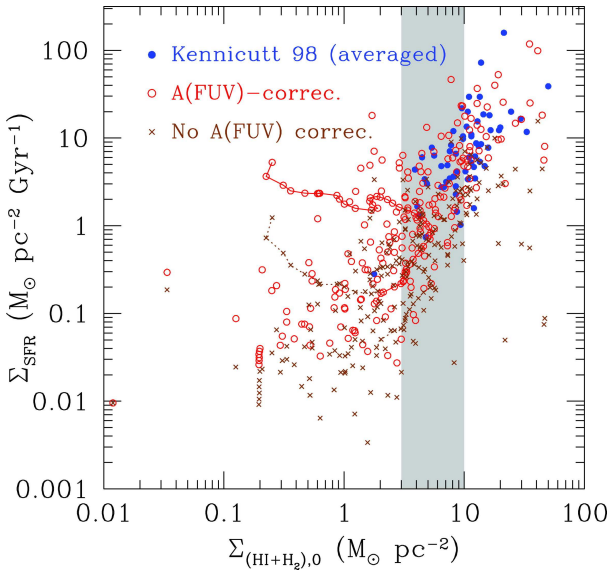

Figure 1.3: Σ_{SFR}, as derived from GALEX UV emission, versus Σ_{gas} for 48 nearby galaxies from Boissier et al. (2007). The open circles represent extinction corrected datapoints from radial profiles for each galaxy. The filled circles represent the datapoints from the sample of normal starforming spirals in Kennicutt (1998, , see left panel of Figure 1.1). (Figure from Boissier et al., 2007)

well with the observation that dust (Popescu & Tuffs, 2003) and CO emission (Braine & Herpin, 2004; Braine et al., 2007; Gardan et al., 2007) are detected in the extended HI envelopes of galaxies and that metallicities in these environments are low, but by no means primordial (Gil de Paz et al., 2007b). How SF in such environments relates to the ISM at high resolution is still largely unexplored.

Figure 1.3 shows the SFR-gas plot of one of the first studies assessing the star formation law systematically in radial profiles using the wide field-of-view GALEX UV data. These data allow to trace star formation further into the outer disks than e.g. typical optical narrow line observations. The plot shows that the trend of the Schmidt Law found by Kennicutt (1998) appears to be continued towards lower Σ_{SFR} and Σ_{gas}, albeit with significantly increased scatter.

1.4 The Spatially Resolved Star Formation Law

In this thesis, a suite of available state-of-the-art multiwavelength data is combined to measure the surface densities of neutral atomic hydrogen gas HI, molecular hydrogen gas, H_2, and SFR (Σ_{HI}, Σ_{H2}, and Σ_{SFR}) for a large sample of nearby galaxies at high spatial resolution. In § 4, these measurements are used to systematically assess the relationships among these three quantities in a sample of 19 nearby within their optical disks (i.e. within the fiducial radius r_{25}) pixel-by-pixel. Power laws, relating Σ_{HI}, Σ_{H2} and $\Sigma_{gas} = \Sigma_{HI} + \Sigma_{H2}$ to Σ_{SFR} are also derived. A particular focus lies on whether there is a common power law index, N, and whether a Schmidt law better relates Σ_{SFR} to Σ_{H2} or Σ_{gas}. In § 5, these studies are extended out to $2\times r_{25}$,

thus reaching into the outer (HI dominated) disks of galaxies. The relation between $\Sigma_{\rm HI}$ and $\Sigma_{\rm SFR}$ is studied in this regime for 26 galaxies using radial profiles, binned profiles and pixel-by-pixel sampling. We also assess how these relationships vary between the optical and the outer disks.

Specifically, this thesis addresses the following questions: How do the SFR, H_2, and HI surface densities relate to one another in nearby galaxies pixel-by-pixel? Which of these relationships are common across galaxies, and which vary with environment? Differences in these SFR-gas relationships for the H_2-dominated centers of spiral galaxies, their HI-dominated outskirts, and HI-rich late type galaxies are elaborately assessed. By probing out to *twice* the optical radius and including late-type galaxies, we are able to strongly constrain the universality of the various Schmidt laws.

Chapter 2

THINGS - The HI Nearby Galaxy Survey

The analyses presented in this thesis depend crucially on sensitive, high-resolution HI data. These data are provided by THINGS, 'The HI Nearby Galaxy Survey' (Walter et al., 2008). Because a significant part of this thesis was dedicated towards THINGS data reduction and processing, as well as towards preparation of the final data products, this dataset and the major steps of the data reduction will be presented in somewhat greater detail than the ancillary datasets that will be introduced in the subsequent chapter. First off though, some basics about the emission mechanism behind the 21 cm HI line will be recapitulated.

2.1 The 21 cm Line

The 'forbidden' HI line at a frequency of 1.42 GHz, corresponding to a wavelength of about 21 cm, which was predicted already in 1945 (Van de Hulst, 1945) and first detected 1951 by Ewen & Purcell (1951), opens up a window into the universe that allows to obtain a picture of the distribution of the most abundant atom in space: hydrogen. The extremely low frequency, i.e. low energy difference, of this transition is due to the fact that it arises from a hyperfine structure transition F(1→0) in the hydrogen atom, which corresponds to a flip of the proton and electron spin-configuration from parallel to antiparallel. The transition is highly forbidden (magnetic dipole transition), leading to an extremely low transition probability, i.e. an extremely long half-life time of about 10 Megayears.

Observational evidence has shown over the last decades that about half of the HI is in a cold phase (cold neutral medium, CNM) at temperatures of around 100 K, and half of it is in a warm phase (warm neutral medium, WNM) at temperatures of about 7000 K. Disentangling these two phases is challenging, but feasible observationally, because the HI absorption coefficient favors the cold phase (whereas both phases are seen in emission!).

Strictly speaking, the long life-time of the transition is only true in extremely rarefied environments (with no interaction between the hydrogen atoms) with densities up to a few atoms per cm^3. At densities greater than that, collisional processes will

dominate de-excitation of the hydrogen atoms and significantly lower half-life times of the excited hyperfine-structure state. Because hydrogen is so abundant in the universe, this radiation is still observable in emission despite the long life-times.

The dominating process leading to excitation in typical interstellar environments are hydrogen-hydrogen collisions. Because the energy difference between the two fine structure levels is so low, collisional excitation of the HI requires only a temperature as low as about 0.07 K (given high enough densities, like those that prevail in the CNM). This temperature is readily provided by the 3 K radiation from the cosmic microwave background (CMB). Quite unfortunately, the observed brightness temperature in an otherwise not heated (e.g. intergalactic) HI cloud will also be at 3 K, which means the emission from the cloud cannot be disentangled from the CMB emission surrounding it. Hence, further heating of the HI in excess of the CMB is required to make HI observationally accessable. There are other processes too that may have significant impact on excitation and de-excitation, like e.g. hydrogen-hydrogen and hydrogen-electron spin exchange. These processes depend on boundary conditions like hydrogen and electron densities or on the temperature of the surrounding medium and the radiation field. A complete assessment of this topic is beyond the scope of this thesis and the reader is referred to canonical textbooks on radio astronomy or the interstellar medium (e.g. Rohlfs & Wilson, 1996; Spitzer, 1978).

The 21 cm line lies in the microwave window of the Earth's atmosphere and is so readily observable with radio telescopes from the ground. Due to the long wavelength (as compared to e.g. optical observations), the line is also very robust to atmospheric turbulence or changing weather conditions. HI is typically optically thin and because the energy of the transition is very low, the ratio of populations in the two energy levels is merely determined by the statistical weights. Therefore, the number of hydrogen atoms along a given line of sight can be unambiguously determined. This allows to derive total HI masses of e.g. galaxies or HI clouds in the Milky Way. Because the HI line traces the bulk of the gas in a galaxy, and because HI can be found at all radii, it is also ideally suited to derive galaxy rotation curves. The long life-time of the excited state leads to an extremely small natural line width, mostly broadened by Doppler-motions of individual gas parcels. It so allows to also accurately measure the velocity dispersions in the hydrogen gas along a line of sight and also, by its offset from the rest frame frequency, the radial Doppler-motions of objects, like e.g. galaxies, relative to the observer.

2.2 Pushing the Limits - The need for new HI Data on Nearby Galaxies

Early studies using the 21 cm line at the first single dish radio telescopes, operated at resolutions of the order 10'. Thus, they focused mainly on studies of Galactic HI for spatially resolved studies, or on nearby extragalactic targets to perform integrated measurements (e.g. determining total HI masses of nearby galaxies). With the advent of more advanced receiver technology and radio interferometers, high resolution measurements and much better sensitivities could be achieved. Extragalactic

Figure 2.1: *The National Radio Astronomy Observatory's Very Large Array (VLA). The radio interferometer consists of 25 antennas, each 27 m in diameter. The maximum antenna separation (A array configuration) is 36 km. Its sensitivity corresponds to what could be achieved with a single dish 130 m in diameter. (Image courtesy of NRAO/AUI)*

targets could be spatially resolved, and more distant objects could be detected in HI emission. With state-of-the-art interferometers like the VLA (see Figure 2.1), ATCA or WSRT, angular resolutions of ∼10" or better became feasible.

To date, numerous studies of individual galaxies, e.g. M 101 (Kamphuis et al., 1991), M 31 (Brinks & Bajaja, 1986) or the Magellanic Clouds (Staveley-Smith et al., 1997; Kim et al., 1999), and the first HI surveys (e.g. Braun, 1995; Swaters et al., 2002) were carried out at high spatial resolution. Nevertheless, the need for a systematic HI survey at high spatial and velocity resolution, covering nearby galaxies of various morphological types (including dwarf irregulars), total HI masses, Hubble types and luminosities remained. In order to achieve these goals, THINGS consists of observations that represent the frontier of technical feasibility with the NRAO[1] VLA (see Figure 2.1). THINGS observations cover 34 galaxies, most of which are also part of the '*Spitzer* Infrared Nearby Galaxies Survey' (SINGS, Kennicutt et al., 2003). This ensures a diverse set of ancillary multiwavelength observations for most THINGS galaxies.

Key science questions that are addressed by the THINGS team members include: Derivation of high-precision rotation curves, assessment of the velocity fields re-

[1]The National Radio Astronomy Observatory is a facility of the National Science Foundation operated under cooperative agreement by Associated Universities, Inc.

garding e.g. non-circular motions and careful mass modeling (efforts led by Erwin de Blok, University of Cape Town, South Africa); Studying the small scale structure of the ISM (efforts led by Elias Brinks, University of Hertfordshire, United Kingdom); Assessing SF properties and testing SF recipes (efforts led by Fabian Walter, Max-Planck Institute for Astronomy, Germany). In this context, this thesis represents one of two projects regarding the analysis of the SF characteristics in THINGS, with emphasis on the SF law (i.e. a pixel-by-pixel assessment of the Schmidt-Kennicutt relation) and on SF in the outer disks of galaxies.

2.3 Survey Parameters

The THINGS sample consists of 34 nearby galaxies. The sample covers a wide range of luminosities, metallicities, total HI masses and Hubble types, including dwarf galaxies. THINGS thus allows to probe a range of physical conditions in the neutral atomic hydrogen gas. Early type galaxies, due to the lack of significant amounts of HI, and starburst galaxies are not part of the sample. Furthermore edge-on galaxies are excluded, because these systems do not facilitate assessing the key science questions mentioned above, like e.g. detailed studies of the disk kinematics. Particularly this thesis work relies on low inclination angles of the target galaxies to be able to sample their disks and their outskirts pixel-by-pixel. Figure 2.2 shows the THINGS HI intensity maps for the entire sample and illustrates the range of sizes and HI masses that this survey probes. See § 2.4 for more information on how these HI maps are created.

As noted above, most THINGS galaxies also overlap the SINGS sample. This ensures comprehensive multi-wavelength coverage from the x-ray over UV and optical to IR and radio continuum data and HI data from THINGS. For reasons of target visibility, all but 4 galaxies are on the northern hemisphere (NGC 3521 has a declination of $\sim$0°and the targets with significantly negative declinations are: NGC 3621, NGC 5236 (M 83) and NGC 7793). Eventually, galaxies that are further away than 15 Mpc are excluded to ensure a spatial resolution of below 500 pc at an angular resolution of $\sim$6", which is the typical resolution in our 'robust weighted' maps (see § 2.4.1). Local Group galaxies are also excluded due to their large angular extent on the sky, where full mapping would have consumed a large amount of observing time. The final list of all THINGS galaxies along with their major parameters is provided in Table 2.1 (adopted from Walter et al., 2008).

The velocity resolution of the data is 5 km/s or better (depending on the HI line width of each galaxy and constrained by the available VLA correlator settings). This allows to fully sample HI lines in the WNM with typical linewidths of 15 km/s FWHM. All THINGS galaxies were observed with the VLA in B, C and D configuration (i.e. in all but the most extended A configuration). Observations in B configuration (where the maximum antenna separation between two VLA antennas is 10 km) allow to achieve angular resolutions of $\sim$6" at 21 cm, which is directly comparable to e.g. the resolution of the *Spitzer* Space Telescope at 24 μm or of the GALEX UV observatory in its near UV band. Because the more extended configurations are more sensitive to the lower surface brightness emission on small angular

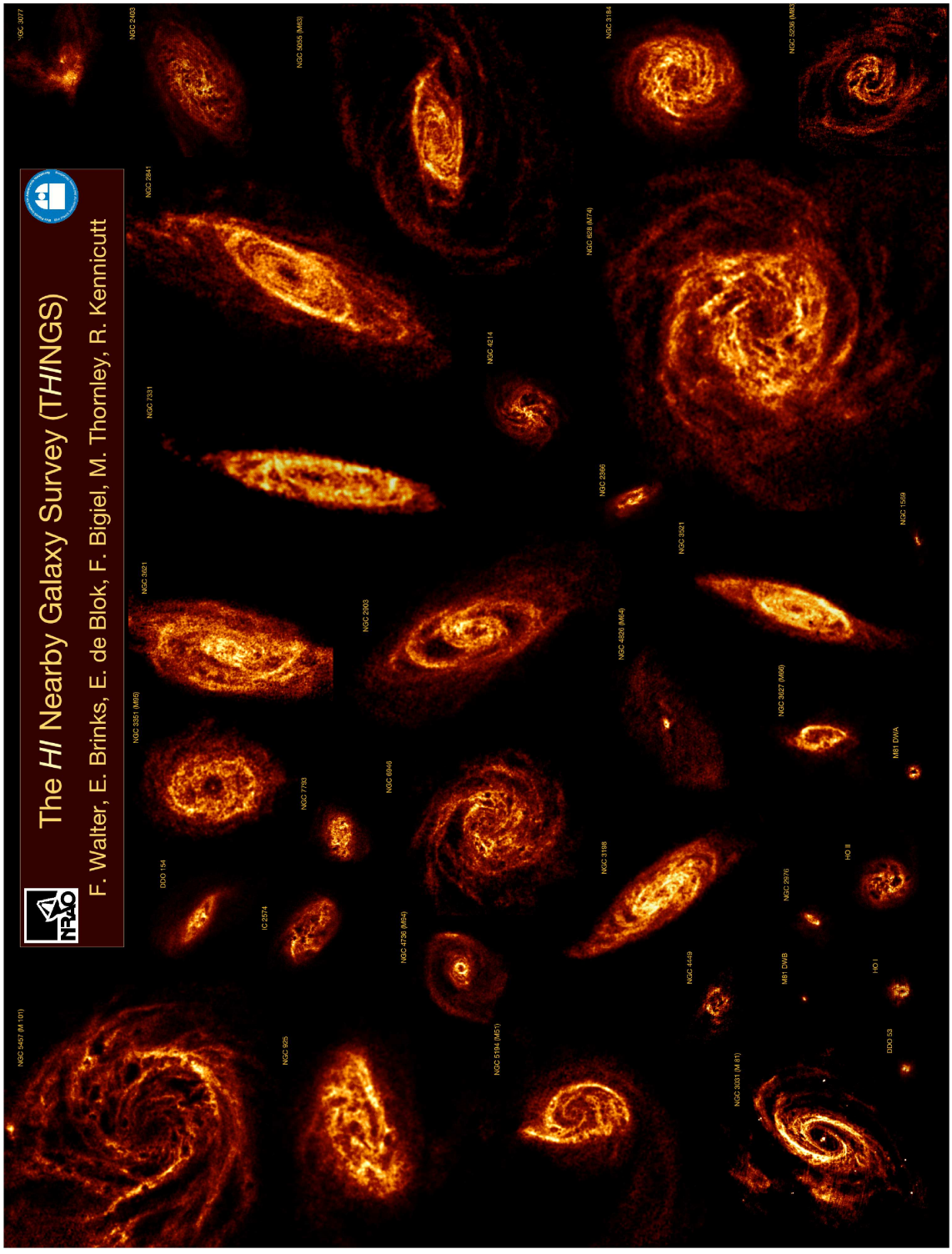

Figure 2.2: *The THINGS sample. Shown are HI intensity maps of the 34 THINGS galaxies all on the same physical scale, thus galaxy sizes can be directly compared. A comparison between the maps of some of the small dwarf galaxies and grand-design spirals reflects the large range in HI mass and the diverse morphologies covered by THINGS.*

scales, including observations from the more compact C and D configurations make sure that also diffuse and extended HI emission covering large angular scales on the sky is observed (in D configuration, the VLA is sensitive to emission from angular scales up to 15'). This also ensures excellent flux recovery even for extended galaxies. The required integration time for each configuration is estimated from the key science driver to investigate the HI-SF relation in THINGS. Therefore, a sensitivity at least 3 times better than the canonical SF threshold of $\sim 10^{21}\,cm^{-2}$ (e.g. Schaye, 2004) is required. A 7 hour integration in B configuration yields at least a 3σ sensitivity of $3.2 \times 10^{20}\,cm^{-2}$ in two adjacent 5 km/s channels and for a 6" beam. Because, as opposed to the compact configurations, the more extended configurations are sensitive to the fainter small scale structure, the observing time for an individual galaxy was split between the different configurations as B:C:D = 7h:2.5h:1.5h. The sensitivities estimated above can be increased significantly by using the 'natural weighted' maps (see § 2.4.1) or by convolving the maps to lower resolutions. Such maps are then ideally suited to study e.g. the diffuse emission in extended HI disks. Altogether, including some archival data that already existed for individual galaxies, the VLA observations for THINGS total ∼500 h and were carried out between 2003 and 2005.

Galaxy	RA(2000.0)	Dec(2000.0)	D	V_{sys}	$\log(D_{25})$	m_B	M_B	Incl	P.A.	Metal.	SFR	Type
	hh mm ss.s	dd mm ss.s	Mpc	km s^{-1}	$\log(0.1')$	mag	mag	°	°	12+log(O/H)	$M_\odot$ yr^{-1}	—
NGC 628	01 36 41.8	+15 47 00	7.3 [K04]	659.1	1.99	9.35	-19.97	7	20 [T08]	8.33 [M08]	1.21 [L08]	5
NGC 925	02 27 16.5 [T08]	+33 34 44	9.2 [F01]	552.5	2.03	9.77	-20.04	66	287 [dB08]	8.24 [M08]	1.09 [L08]	7
NGC 1569	04 30 49.0	+64 50 53	2.0 [K04]	-85.6	1.60	8.33	-18.12	63	112 [M05]	8.16 [S89]	0.06 [K98]	10
NGC 2366	07 28 53.4 [O08]	+69 12 51	3.4 [H01]	100.1	1.64	10.51	-17.17	64	40 [O08]	7.96 [S89]	—	10
NGC 2403	07 36 51.1 [T08]	+65 36 03	3.2 [F01]	133.1	2.20	8.11	-19.43	63	124 [dB08]	8.31 [M08]	0.85 [L08]	6
Ho II	08 19 05.0	+70 43 12	3.4 [K04]	157.1	1.82	10.78	-16.87	41	177 [P92]	7.68 [M08]	0.07 [L08]	10
M81 DwA	08 23 56.0	+71 01 45	3.6 [K04]	112.0	1.1*	16.26	-11.49	23	49 [B06]	—	—	10
DDO 53	08 34 07.2	+66 10 54	3.6 [K04]	17.7	0.89	14.31	-13.45	31	132 [B06]	7.77 [M08]	0.008 [L08]	10
NGC 2841	09 22 02.6 [T08]	+50 58 35	14.1 [M01]	635.2	1.84	9.54	-21.21	74	153 [dB08]	8.52 [M08]	0.20 [K03]	3
NGC 2903	09 32 10.1 [T08]	+21 30 04	8.9 [D00]	556.6	2.07	8.82	-20.93	65	204 [dB08]	9.12 [Z94]	—	4
Ho I	09 40 32.3	+71 10 56	3.8 [K04]	140.4	1.52	13.12	-14.80	12	50 [O01]	7.54 [M08]	0.006 [L08]	10
NGC 2976	09 47 15.3 [T08]	+67 55 00	3.6 [K02]	2.6	1.86	9.98	-17.78	65	335 [dB08]	8.30 [M08]	0.10 [L08]	5
NGC 3031	09 55 33.1 [T08]	+69 03 55	3.6 [F01]	-39.4	2.33	7.07	-20.73	59	330 [dB08]	8.41 [M08]	1.06 [L08]	2
NGC 3077	10 03 19.1	+68 44 02	3.8 [K04]	5.0	1.73	10.16	-17.75	46	45	8.64 [S94]	0.09 [K98]	10
M81 DwB	10 05 30.6	+70 21 52	5.3 [K04]	346.4	1.05	14.39	-14.23	44	321	7.85 [M08]	0.005 [L08]	10
NGC 3184	10 18 17.0	+41 25 28	11.1 [L02]	593.3	1.87	10.31	-19.92	16	179 [T08]	8.48 [M08]	1.43 [L08]	6
NGC 3198	10 19 55.0 [T08]	+45 32 59	13.8 [F01]	658.9	1.81	9.95	-20.75	72	215 [dB08]	8.32 [M08]	0.85 [K03]	5
IC 2574	10 28 27.7 [O08]	+68 24 59	4.0 [K02]	48.6	2.11	9.91	-18.11	53	56 [O08]	7.94 [M08]	0.12 [L08]	9
NGC 3351	10 43 57.7	+11 42 14	10.1 [K04]	779.0	1.86	10.13	-19.88	41	192 [T08]	8.60 [M08]	0.71 [L08]	3
NGC 3521	11 05 48.6 [T08]	–00 02 09	10.7 [vflow]	798.2	1.92	9.21	-20.94	73	340 [dB08]	8.36 [M08]	3.34 [L08]	4
NGC 3621	11 18 16.5 [T08]	–32 48 51	6.6 [F01]	730.1	1.99	9.06	-20.05	65	345 [dB08]	8.24 [M08]	2.09 [L08]	7
NGC 3627	11 20 15.0 [T08]	+12 59 30	9.3 [F01]	717.3	2.01	9.09	-20.74	62	173 [dB08]	8.43 [M08]	2.44 [L08]	3
NGC 4214	12 15 39.2	+36 19 37	2.9 [K04]	292.9	1.83	9.91	-17.43	44	65	8.34 [S89]	0.05 [K98]	10
NGC 4449	12 28 11.9	+44 05 40	4.2 [K04]	202.7	1.67	8.98	-19.14	60	230 [H98]	8.32 [S89]	—	10
NGC 4736	12 50 53.0 [T08]	+41 07 13	4.7 [K04]	307.6	1.89	8.54	-19.80	41	296 [dB08]	8.31 [M08]	0.43 [L08]	2
DDO 154	12 54 05.9 [T08]	+27 09 10	4.3 [K04]	375.5	1.29	13.94	-14.23	66	230 [dB08]	7.54 [M08]	0.004 [L08]	10
NGC 4826	12 56 43.6 [T08]	+21 41 00	7.5 [K04]	407.9	2.02	8.74	-20.63	65	121 [dB08]	8.59 [M08]	0.82 [L08]	2
NGC 5055	13 15 49.2 [T08]	+42 01 45	10.1 [vflow]	499.3	2.07	8.90	-21.12	59	102 [dB08]	8.42 [M08]	2.42 [L08]	4
NGC 5194	13 29 52.7	+47 11 43	8.0 [K04]	456.2	1.89	8.48	-21.04	42	172 [T08]	8.54 [M08]	6.05 [L08]	4
NGC 5236	13 37 00.9	–29 51 57	4.5 [K04]	510.0	2.19	7.48	-20.77	24	225 [T93]	9.16 [Z94]	2.52 [K98]	5
NGC 5457	14 03 12.6	+54 20 57	7.4 [K04]	226.5	2.38	8.29	-21.05	18	39 [B81]	8.52 [Z94]	2.49 [K98]	6
NGC 6946	20 34 52.2 [T08]	+60 09 14	5.9 [K04]	42.2	2.06	8.24	-20.61	33	243 [dB08]	8.40 [M08]	4.76 [L08]	6
NGC 7331	22 37 04.1 [T08]	+34 24 57	14.7 [F01]	815.6	1.96	9.17	-21.67	76	168 [dB08]	8.36 [M08]	4.20 [K03]	3
NGC 7793	23 57 49.7 [T08]	–32 35 28	3.9 [K04]	227.2	2.02	9.17	-18.79	50	290 [dB08]	8.22 [M08]	0.51 [L08]	7

Table 2.1: Properties of the THINGS galaxy sample. Please see next page for comments on individual columns. Adopted from Walter et al. (2008).

Comments on columns:
column 1: galaxy name
column 2/3: Coordinates in J2000.0. No entry: coordinates taken from NED; T08: Trachternach et al. 2008
column 4: distances in Mpc. vflow: distances calculated from NED using Hubble flow distances (corrected for Virgo infall); dB08: de Blok et al. 2008, O08: Oh et al. 2008, K02: Karachentsev et al. 2002, K04: Karachentsev et al. 2004, H01: Hunter et al. 2001, F01: Freedman et al. 2001, L02: Leonard et al. 2002, M01: Macri et al. 2001, D00: Drozdovsky & Karachentsev 2000
column 5: velocity of the HI spectra, derived from the central velocity of the 20% level of the HI profile.
column 6: optical size (taken from LEDA); K04: Karachentsev et al. 2004; Note: Holmberg diameter is given for M 81 dwA
column 7: apparent blue magnitude, corrected for Galactic foreground extinction and extinction internal to the galaxy from LEDA (LEDA.UNIV-LYON.FR); B06: Begum et al. 2006
column 8: absolute B magnitude derived from columns 7 and 4
column 9/10: Inclination and position angle; No entry: taken from LEDA, dB08: de Blok et al. 2008, B06: Begum et al. 2006, O01: Ott et al. 2001, P92: Puche et al. 1992, O08: Oh et al. 2008, M05: Mühle et al. 2005, T08: Tamburro et al. 2008, H98: Hunter et al. 1998, T93: Tilanus & Allen 1993, B81: Bosma et al. 1981
column 11: metallicities. M08: Moustakas et al. 2008, S89: Skillman et al. 1989, Z94: Zaritzky et al. 1994, S94: Storchi et al. 1994
column 12: Star formation rates. Derived from fluxes published in the literature and corrected for our adopted distances: L08: Lee et al. 2008, K98: Kennicutt 1998, K03: Kennicutt et al. 2003
column 13: Morphological type from LEDA (LEDA.UNIV-LYON.FR).

2.4 Data Reduction

In the following, the major steps of the process to turn the observed raw data into calibrated datacubes and moment maps are addressed. A few peculiarities that occur when dealing with radio interferometry data, like THINGS, will be explained in more detail. Eventually, the final data products will be introduced and exemplary channel maps from HI data cubes as well as HI intensity maps will be presented.

2.4.1 From Observations to Data Cubes

The entire data reduction is carried out using AIPS[2]. The flux scale for the data is determined by observing the VLA standard primary calibrators, which are typically distant quasars. One of these calibrators is observed at the beginning and the end of each observation. To calibrate the phases and amplitudes of the observed interferometric signals, which are time variable, so-called secondary calibrators (also mostly quasars) are observed that have to be unresolved for the respective array configuration. The calibrator source is observed approximately every 30 minutes to allow for accurate phase and amplitude calibration of the data. In order to avoid time consuming repositioning of the telescope dishes every 30 minutes, the calibrator is selected to be located as close as possible to the target galaxy on the sky.

What is actually measured with an interferometer, are amplitudes and phases in Fourier space. Each baseline, i.e. an imaginary line connecting two telescopes, is sensitive to emission from a specific angular scale (which is determined by the length of the baseline, see discussion on the different VLA configurations in § 2.3). In this Fourier space, also called uv-plane, each baseline is represented by a specific point in this plane at any given time. A Fourier transformation basically converts these uv-data into, eventually, HI intensity distributions. Because during the Fourier transformation data from each baseline contributes to the entire image, also corrupt data from *individual* baselines have impact on the *entire* image. Thus, for all observations, the amplitudes and phases for the data from all baselines have to be inspected by eye. Particularly important is temporal stability during an observation. A thorough inspection and removal of corrupt baselines dramatically contributes to obtaining the best possible image quality in the final data products. Such corrupt baselines or baseline segments may be caused by interference between antennae or even antennae failure and must be flagged during data reduction. Another cause for corrupt data on specifically the short baselines, which means that observations in the compact D-array are particularly affected, is solar interference. This can be partly avoided by scheduling respective observations during nighttime (as it has been the case for the THINGS observations). Eventually, all the data that were observed in the different array configurations can be combined into a single dataset.

Because the frequency bandwidth of the VLA correlator at a wavelength of 21 cm exceeds the widths of typical HI lines by construction, the channels (i.e. frequency 'bins') that do not contain HI line emission, and thus only show the underlying radio continuum, must be identified by eye. In order to subtract the continuum from the

[2]The Astronomical Image Processing System (AIPS) has been developed by the NRAO.

channels containing line emission, a polynomial (usually first order) is fit to the line free channels and the derived continuum values are subsequently subtracted from the emission in each channel.

The data are then 'imaged', which means turning them into 3-dimensional position-position-frequency 'datacubes' (this is in principle the Fourier transformation mentioned above). Thus, stepping through this datacube along the frequency axis, every plane of the cube (which typically contains ∼100 planes) shows the observed area on the sky in a distinct frequency interval (and so samples the Doppler-broadened HI line). In other words, each pixel in this datacube represents a spectrum (along the frequency axis) at a particular position on the sky.

As part of the imaging process, different weight can be given to the measurements from different baselines. As longer baselines are more sensitive to emission from smaller angular scales, they provide data with higher spatial resolution at the cost of higher noise from the small scale emission. The shorter baselines in turn provide data with lower spatial resolution and are therefore more sensitive to the diffuse larger scale structure, which is less noisy. Thus, by weighing the data from more extended and more compact baselines differently, one can put more emphasis either on spatial resolution or sensitivity. In order to find the best tradeoff for the data, datacubes were imaged applying several weighting schemes. Such a scheme is parameterized by a single number, which is called the ROBUST parameter. A value of +5 corresponds to 'natural weighting'. This gives equal weight to data from all baselines and therefore retains the highest surface density sensitivity at moderate spatial resolution. A value of -5, which is referred to as 'uniform weighting', on the other hand assigns less weight to the data from the shorter baselines, leading to higher resolution but lower sensitivity. Anything inbetween these extreme values is often referred to as 'robust weighting' and goes back to Briggs (1995). This 'robust scheme' allows to chose any weighting inbetween the natural and the uniform schemes.

Figure 2.3 illustrates how the effective area of the synthesized beam, i.e. resolution, and the 1σ RMS noise, i.e. sensitivity, of the HI intensity map of NGC 3198 vary as a function of the ROBUST parameter. Ideally, one wants to determine a value for this parameter where reasonably good resolution and sensitivity are achieved simultaneously. Figure 2.3 shows that this is the case between 0 and 0.5 for this particular galaxy. Assessing many of the THINGS galaxies this way, a robust value of 0.5 turned out to yield the best compromise between achieving good resolution and low noise for HI data in the THINGS sample (the according datacubes will be referred to as RO cubes in the following). Furthermore a full set of natural weighted datacubes (NA cubes in the following) was produced, particularly for science cases that require better sensitivity to diffuse and extended emission, like studies of the extended HI disks for instance.

Figure 2.4 illustrates the different flux recovery capabilities of the natural and robust weighted datacubes. It shows the HI line spectra for 2 galaxies: NGC 2403, a spiral galaxy, and IC 2574, a gas rich dwarf irregular. These flux spectra are obtained by integrating the emission in each channel map for both galaxies and for the NA and RO cubes. The spectra for NGC 2403 show the characteristic double-horned profile, which indicates differential rotation. Also, the Doppler-broadened HI linewidths for

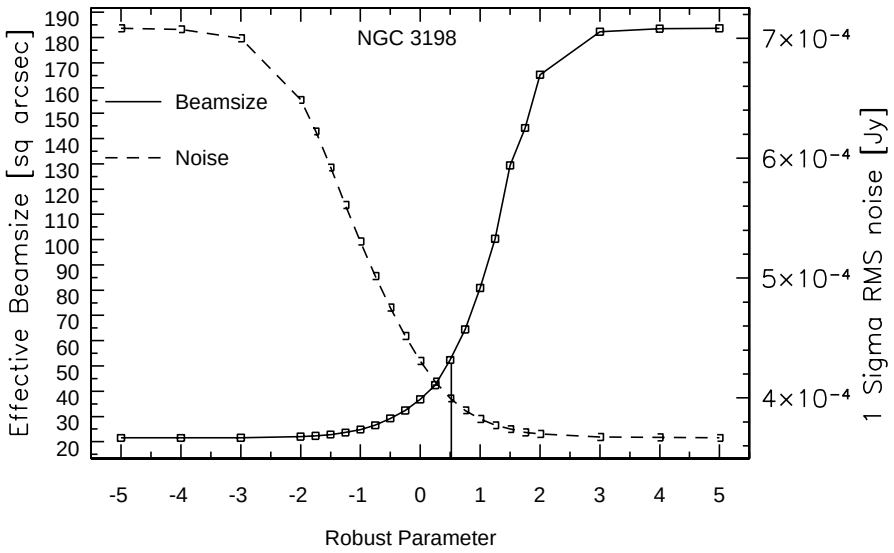

Figure 2.3: *Resolution and sensitivity versus ROBUST parameter for NGC 3198. This figure illustrates how the synthesized beam size decreases, whereas the noise in the HI intensity map increases, as more weight is given to the longer baselines in the 'imaging' process. One finds that a value of ∼0.5 for the ROBUST parameter yields a good compromise between resolution and sensitivity.*

this galaxy are significantly larger than for IC 2574, due to the much higher rotation velocities in NGC 2403. This figure nicely illustrates that, as discussed above, more flux is recovered in the natural weighted data (blue spectra) than in the robust weighted data (green spectra).

2.4.2 Getting nice Images - 'Cleaning'

Something else that is specific to interferometric observations happens when data are imaged: 'Cleaning'. Unlike for single dish telescopes, where the beam resembles a spherical gaussian (this is often referred to as a 'clean beam'), the synthesized beam for interferometers resembles more a gaussian with sidelobes and more or less pronounced wings ('dirty beam'). The situation is similar to light hitting a plane with multiple slits versus the incidence of light on a plane with a single slit: A screen behind the plane will show an interference pattern whose envelope resembles a 'dirty gaussian' with sidelopes and wings in the multi-slit case and a diffraction pattern whose envelope resembles a 'clean gaussian' in the single-slit case. Mathematically, a Fourier transformation of the so-called 'sampling function', which describes the distribution of the slits on the plane, yields a function (which, for a point source, is called the 'response function') that describes the envelope of the interference (or diffraction) pattern. Technically speaking, the non-gaussian features in the synthesized beams of interferometers are caused by the non-uniform coverage of the previously mentioned uv-plane (which corresponds to the plane with the slits above). The slit example above is a strong simplification though: For astronomical obser-

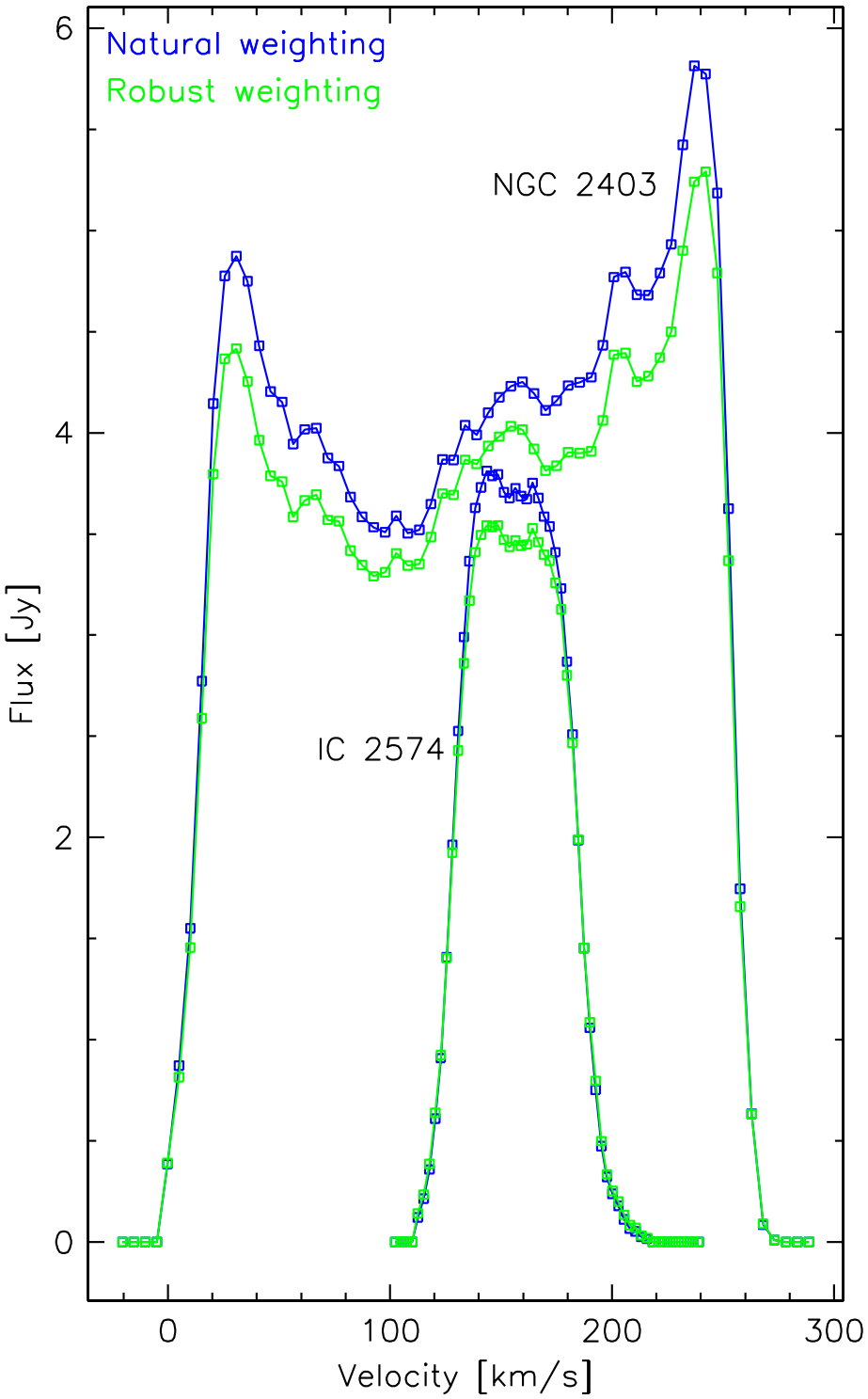

Figure 2.4: *HI line spectra for NGC 2403 and IC 2574 derived from the natural (blue) and robust (green) weighted datacubes respectively.*

vations with an interferometer, the array configuration changes with respect to the source as the earth rotates.

Because the emission in the sidelobes and wings for the individual beams adds up and thus degrades the image quality, so-called 'cleaning' algorithms attempt to substitute the dirty beams in the image for clean beams. The most commonly used algorithm and the one most other algorithms are based on is described in Högbom (1974). Practically, such an algorithm iteratively determines emission peaks in the image (or in the case of datacubes, in every channel map), 'subtracts a dirty beam' at this position and writes the pixel position and associated flux in a table (the 'cleaning table'). The dirty beam is known because it can be computed via Fourier transformation from the sampling function mentioned above. After a user provided cleaning threshold is met (typically several *sigma* above the noise in the image or image plane), the cleaning stops. At that stage, one has a 'residual map' along with the entries in the cleaning table. A clean (gaussian) beam is then fit to the central maximum of the dirty beam. Eventually, clean beams are restored at the positions given in the cleaning table. This map is then referred to as the 'clean map'.

One has to be careful when measuring fluxes in such a cleaned map though. As first noted by Jorsater & van Moorsel (1995), a cleaned map actually consists of the sum of the residual map, whose flux is in e.g. Jansky per *dirty* beam, while the restored flux from the cleaning components is in Jansky per *clean* beam. Quite often, the unit Jansky per clean beam is assumed for the entire map though. This leads to an overestimation of the total flux in the map by a factor equal to the ratio of the beam areas $r = \Omega_{dirty}/\Omega_{clean}$. This is particularly important for extended objects like in THINGS. The AIPS task IMAGR provides the necessary functionality though to scale the residual image down by this factor to obtain correct fluxes in the cleaned datacubes. A more elaborate discussion of this topic can be found in Jorsater & van Moorsel (1995) and Walter & Brinks (1999).

2.4.3 Last Steps and Final Data Products

In order to distinguish noise from real emission, a datacube is created for each galaxy, whose resolution is convolved to 30". In this cube, all pixels in all channel maps that are not 2σ above the noise in three consecutive channels are blanked. This 'master cube' is subsequently used as a mask on the original datacube. The remaining regions in the original cube are considered to contain real emission. The datacubes are at that stage also corrected for the attenuation of the primary beam towards the edge of the field-of-view.

In a last step, moment maps are computed from the datacubes. These comprise integrated HI maps (moment 0), velocity maps (moment 1) and velocity dispersion maps (moment 2). To derive zeroth moment maps, the datacube is collapsed along its frequency (velocity) axis. Thus, this map represents the distribution of HI intensities, which are typically quoted in units of column density (cm^{-2}) or surface density ($M_{\odot}pc^{-2}$). The first moment maps represent the intensity weighted velocity distribution and the second moment maps the intensity weighted RMS velocity dispersion (both in km/s).

Figure 2.5 shows individual channel maps for the cleaned and masked NA cube for the spiral galaxy NGC 6946. The 'butterfly pattern' (or 'flapping wings') is characteristic for the differential rotation in spiral galaxies. Figure 2.6 shows channel maps for one of the dwarf galaxies in the THINGS sample: Ho II. Figures 2.7 and 2.8 show all 3 moment maps for NGC 6946 and Ho II along with an optical image for comparison. The rich structure in the interstellar medium that is visible in both, the channel maps and the intensity (moment 0) maps, like holes and shells of various sizes, is quite remarkable. The velocity maps (moment 1) show very detailed structure in the velocity fields of both galaxies. Such high-resolution velocity fields can be used for instance to study non-circular motions, i.e. inflow or outflow motions, of the HI. The high spatial and velocity resolution of the THINGS data thus allows to study many dynamical and kinematic properties on unprecedented scales for a large and diverse set of nearby galaxies.

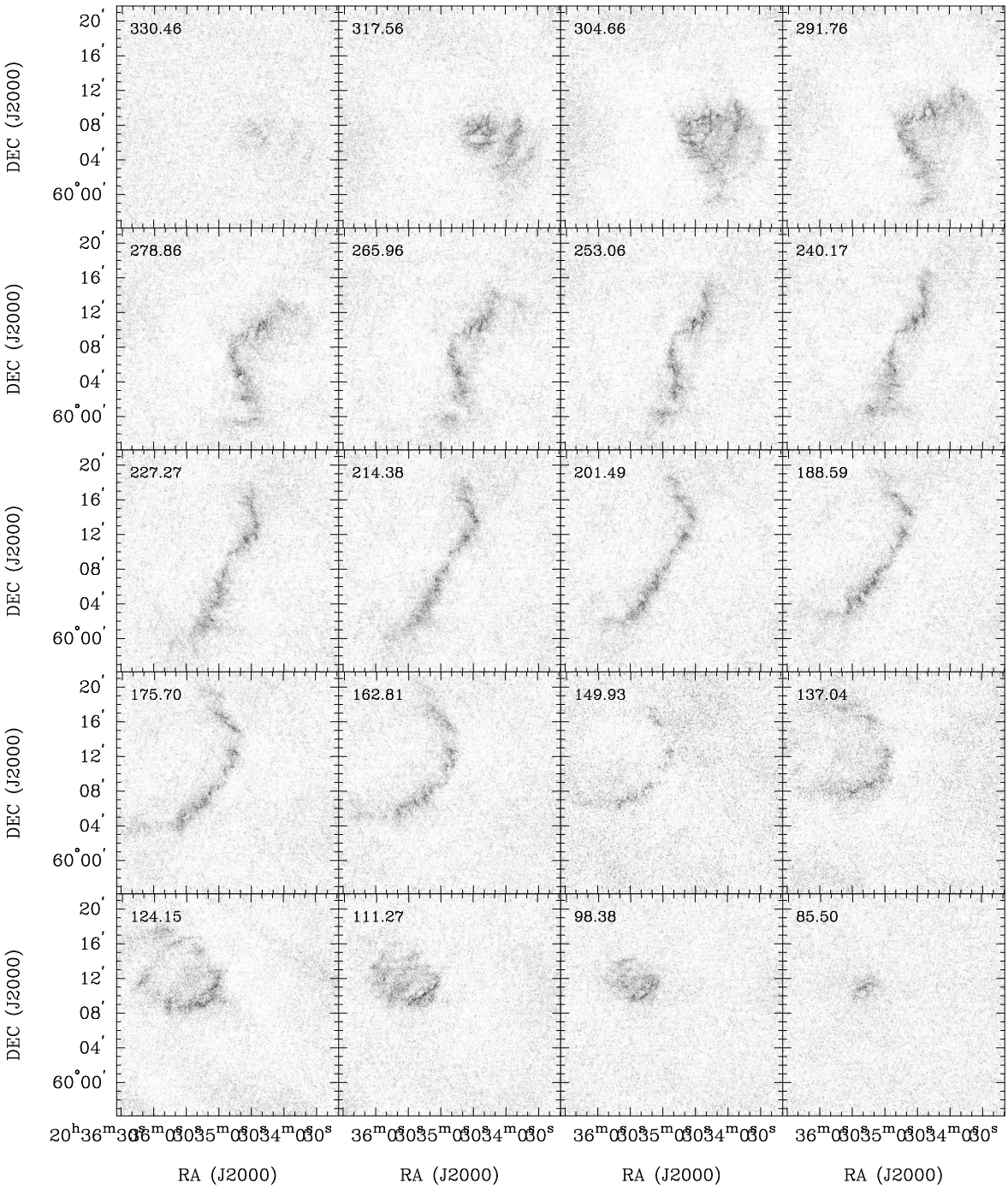

Figure 2.5: *Channel maps for NGC 6946. The grey scale range indicates -0.02 to 6 mJy/beam. Shown is every fifth channel map and the channel width is 2.6 km/s. The number in the corner of each panel indicates the central velocity of the respective channel map. (Figure from Walter et al. (2008)).*

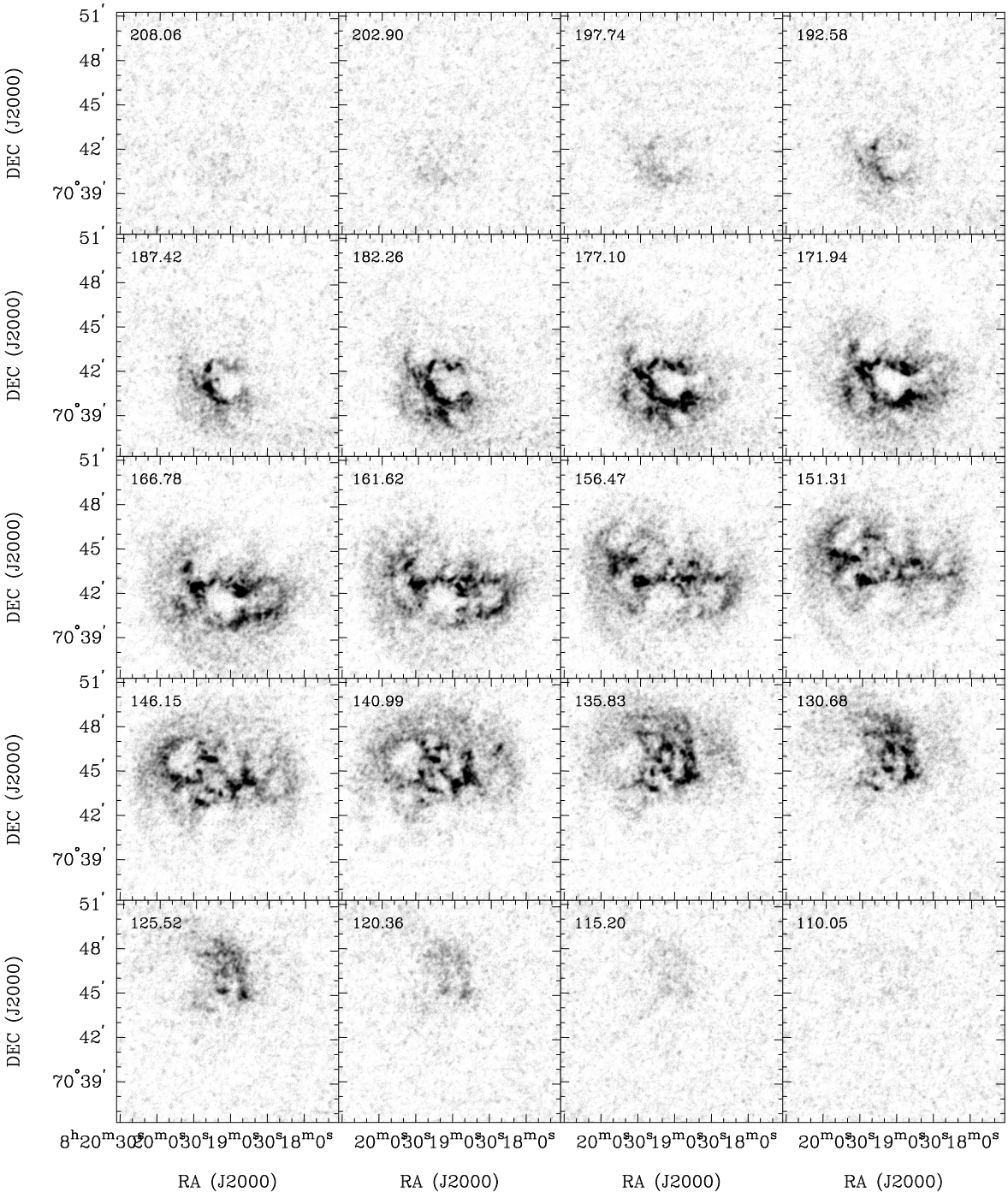

Figure 2.6: *Channel maps for Ho II. The grey scale range indicates -0.02 to 13 mJy/beam. Shown is every second channel map and the channel width is 2.6 km/s. The number in the corner of each panel indicates the central velocity of the respective channel map. (Figure from Walter et al. (2008))*

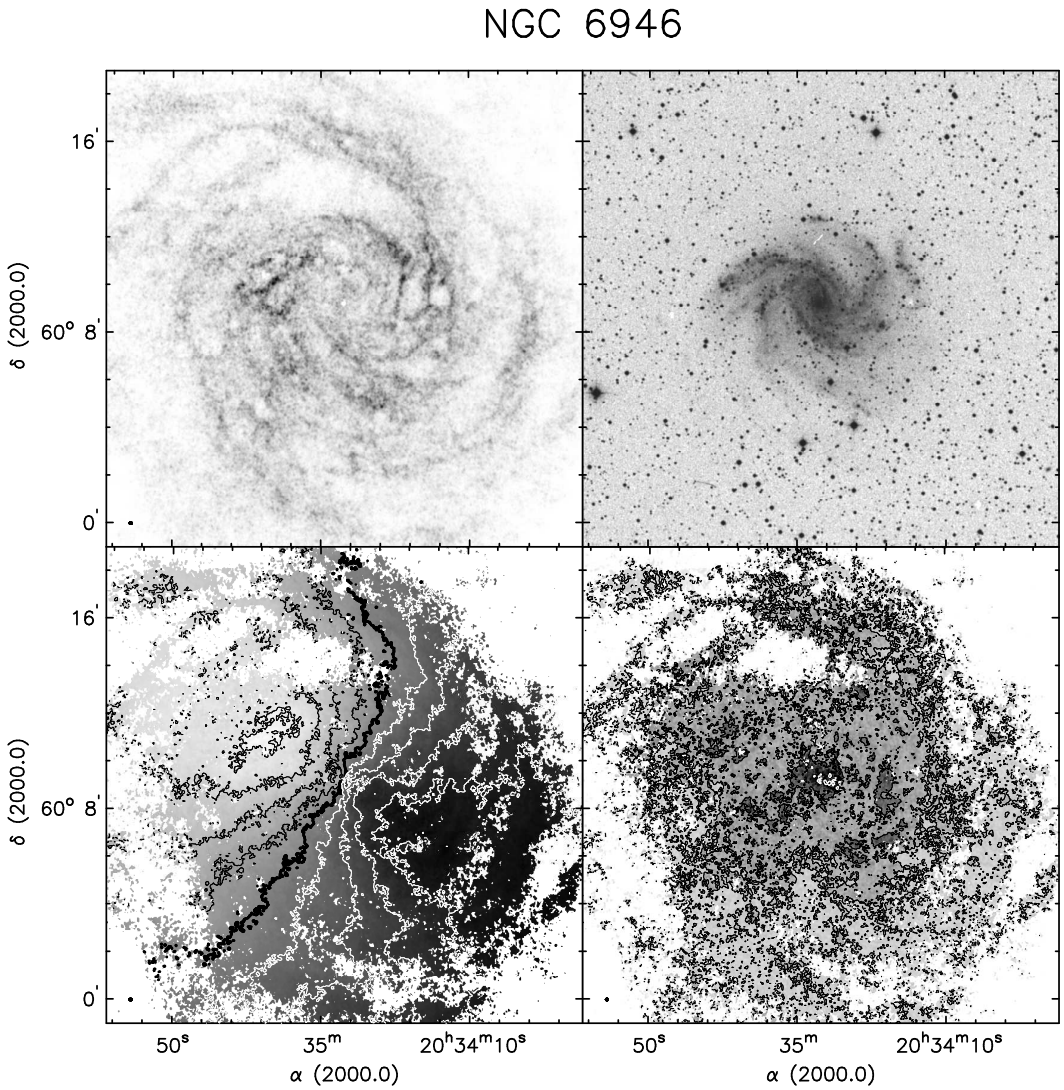

Figure 2.7: *Moment maps and optical image for NGC 6946. Top left: Integrated HI map (moment 0). The grey scale range indicates 0 to 121 Jy km/s. Top right: Optical image from the digitized sky survey (DSS) for comparison. Bottom left: Velocity map (moment 1). The contours are iso-velocity lines, spaced by 25 km/s. The black contours on the lighter grey part of the map represent approaching emission, whereas the white contours on the darker grey part represent receding emission. The thick black contour represents the systemic velocity of 200.0 km/s. Bottom right: Velocity dispersion map (moment 2). The contours indicate dispersions of 5, 10 and 20 km/s. (Figure from Walter et al. (2008))*

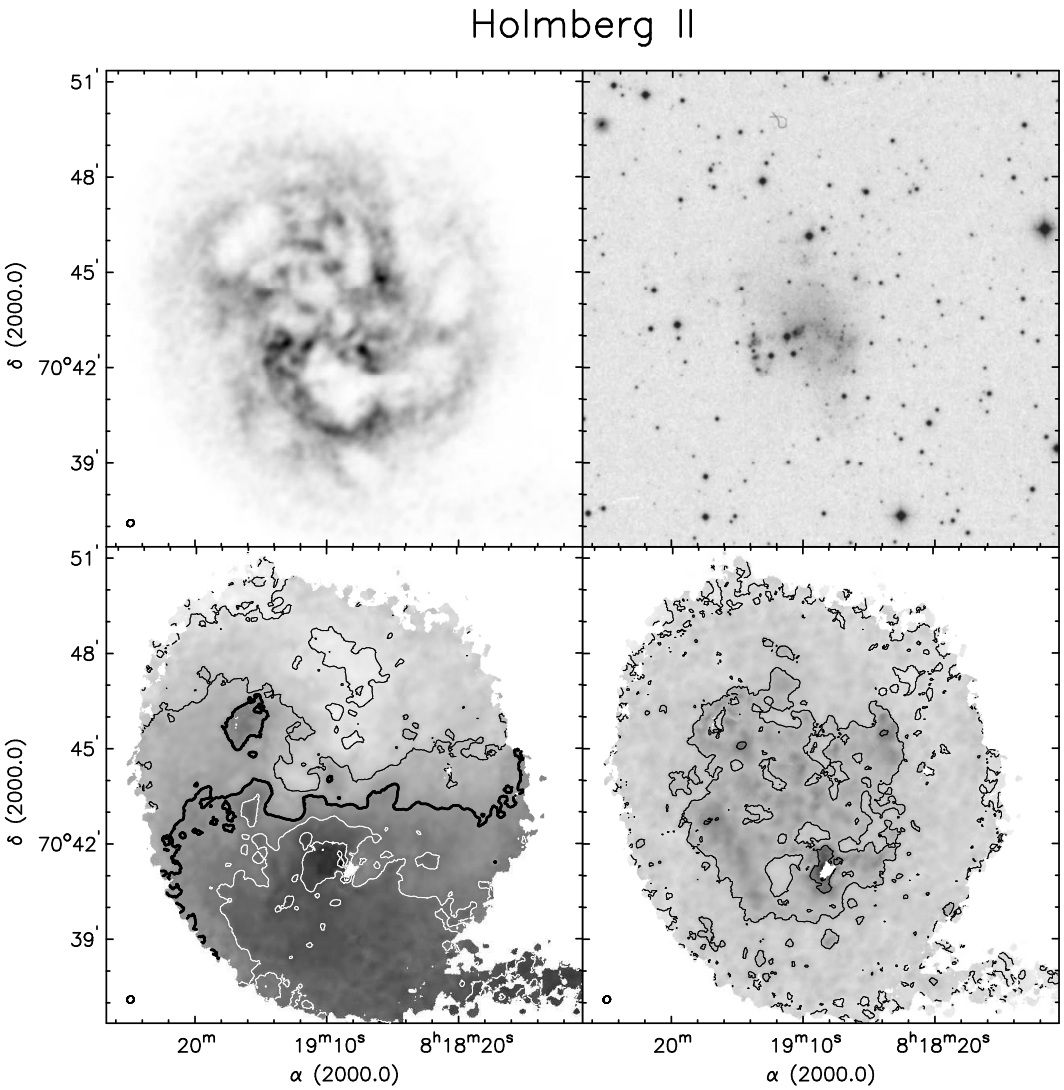

Figure 2.8: *Moment maps and optical image for Ho II. Top left: Integrated HI map (moment 0). The grey scale range indicates 0 to 599 Jy km/s. Top right: Optical image from the digitized sky survey (DSS) for comparison. Bottom left: Velocity map (moment 1). The contours are iso-velocity lines, spaced by 12.5 km/s. The black contours on the lighter grey part of the map represent approaching emission, whereas the white contours on the darker grey part represent receding emission. The thick black contour represents the systemic velocity of 157.1 km/s. Bottom right: Velocity dispersion map (moment 2). The contours indicate dispersions of 5, 10 and 20 km/s. (Figure from Walter et al. (2008))*

Chapter 3

Ancillary Data

This chapters provides an overview of the other datasets that were used to carry out the analyses presented in this thesis. In order to study the relation between gas and star formation from the star forming disks to the outskirts of nearby galaxies, the data have to meet high requirements: They have to provide very sensitive, high resolution state-of-the-art measurements of both, gas and SF, and they have to provide a large field-of-view for the often very extended targets on the sky. Maps of the distribution of atomic hydrogen gas are provided by THINGS (see § 2).

The molecular gas phase, i.e. H_2, is most directly related to star formation and is often the major component in the interstellar medium in the centers ($\lesssim 0.4\ r_{25}$) of spiral galaxies. Because it is very hard to measure H_2 emission directly, and because such measurements only trace warm H_2 components, emission from the CO molecule provides the most reliable way to trace the distribution of the bulk of H_2. In order to be able to asses the relation between gas and star formation inside the star forming disks (i.e. within $\sim r_{25}$), sensitive maps of CO emission are a key component.

A combination of FUV data from GALEX and 24 μm IR data from the *Spitzer* Space telescope is used to trace star formation and derive star formation rates. The FUV emission from GALEX traces photospheric emission from O and early B stars and can be reliably calibrated as a tracer for recent ($\lesssim 10^8$ yrs) star formation. Because FUV emission is heavily affected by dust, the 24 μm IR data are used to correct the FUV data for extinction. For the analysis of star formation in the outer disks, where dust is much less abundant, only the FUV data are used to derive star formation rates (see § 5).

Below is described how maps of neutral atomic hydrogen surface density, $\Sigma_{\rm HI}$, molecular hydrogen surface density, $\Sigma_{\rm H2}$, and star formation rate surface density, $\Sigma_{\rm SFR}$, are derived. These maps form the basis of the analyses of the relation between gas and star formation in nearby galaxies in this thesis.

3.1 CO Data

Distributions of molecular hydrogen surface densities, $\Sigma_{\rm H2}$ are derived from two sources: An ongoing nearby galaxy survey using the HERA focal plane array on the IRAM 30m telescope (hereafter HERA, Leroy et al., in prep.)and the 'BIMA

Figure 3.1: The IRAM 30 m telescope in the Sierra Nevada. The 3 mm CO data that is used in this thesis was obtained with the HERA heterodyne array. (Image courtesy: IRAM)

Survey of Nearby Galaxies' (BIMA SONG, Helfer et al., 2003). An image of the IRAM 30 m telescope is shown in Figure 3.1. Radial profiles, i.e. azimuthally averaged measurements in tilted rings, from the two sets of CO maps agree with one another and also with data from the FCRAO survey (Young et al., 1995). The HERA maps are preferentially used, where available, because they have good extent and sensitivity, often measuring CO well into the HI dominated regime. Capturing the transition from the H_2 dominated ISM to the HI dominated outer disk is critical to differentiate between a molecular and total gas Schmidt law.

The HERA heterodyne array (Schuster et al., 2004) on the IRAM 30 m telescope maps CO $J = 2 \rightarrow 1$ emission with an angular resolution of 11" from 19 nearby galaxies. What distinguishes this survey from most previous CO observations in nearby galaxies is the mapped area: the full optical disk of each galaxy. Also, the sample of galaxies is chosen to complement THINGS (Walter et al., 2008) and the *Spitzer* Infrared Nearby Galaxies Survey (SINGS Kennicutt et al., 2003). This ensures extensive multiwavelength coverage for all HERA galaxies.

HERA maps are used for 6 spiral galaxies in this thesis: NGC 628, NGC 3184, NGC 3521, NGC 4736, NGC 5055 and NGC 6946. These were obtained at the IRAM 30m telescope during January and October 2007 and will be described in Leroy et al., in prep. After masking, these maps are sensitive to surface densities $\Sigma_{H2} \approx 3$ $M_\odot$ pc^{-2}. The Figures 3.2 and 3.3 illustrate the superb quality of the HERA data products. Presented are CO intensity maps for 4 galaxies and channel maps for the spiral galaxy NGC 6946. The CO maps for the almost face-on galaxies NGC 628 and NGC 6946 in the two bottom panels of Figure 3.2 show a beautiful spiral pattern in the inner parts of these galaxies. The overplotted relatively high

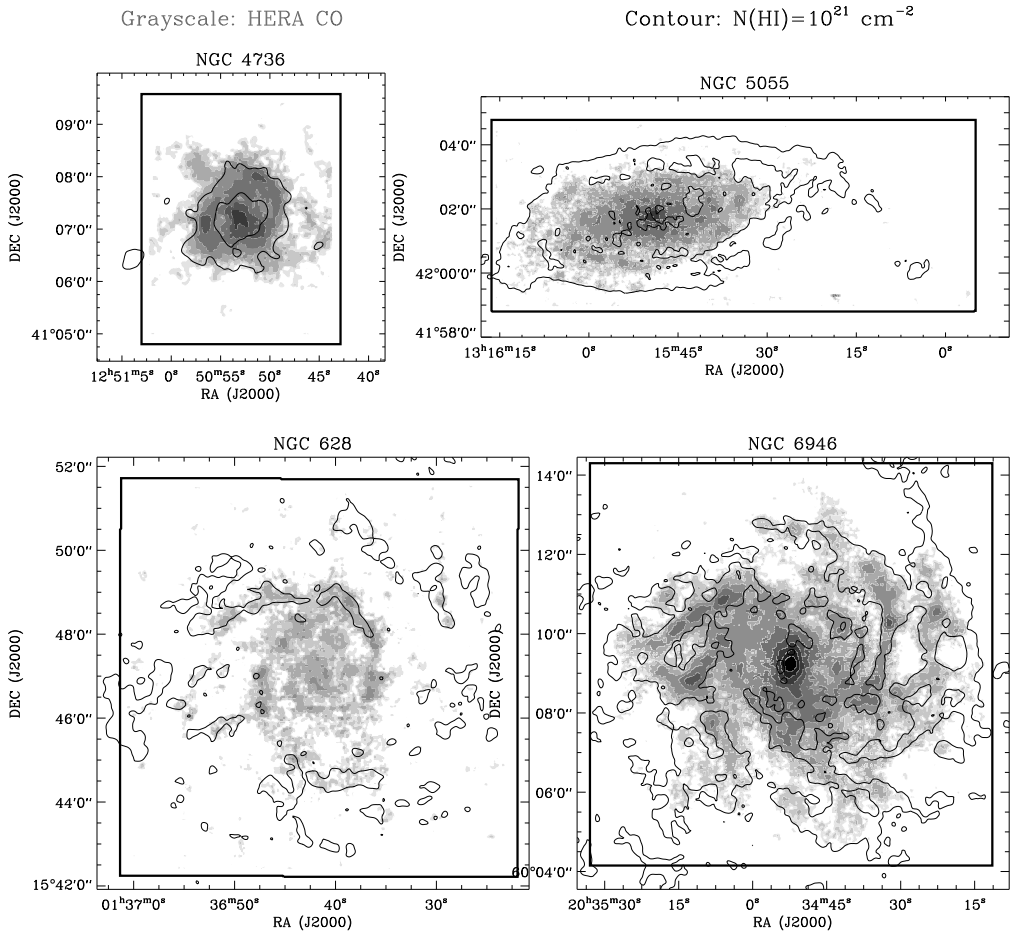

Figure 3.2: HERA CO intensity maps for NGC 4736, NGC 5055, NGC 628 and NGC 6946. The overplotted contours represent an HI column of $10^{21}\,\mathrm{cm}^{-2}$. The HERA maps cover roughly the optical disks of the target galaxies.

HI contour indicates nicely that the CO emission, and thus molecular hydrogen, dominates in the centers of galaxies.

BIMA SONG produced maps of CO $J = 1 \rightarrow 0$ emission with good resolution, $\sim 7''$, but limited field of view. We use these for two galaxies, NGC 3627 and NGC 5194. Both maps include zero-spacing data from the Kitt Peak 12 m telescope, making them sensitive to extended structure. After masking, the BIMA SONG maps are sensitive to surface densities above $\Sigma_{\mathrm{H2}} \approx 10\ \mathrm{M}_\odot\ \mathrm{pc}^{-2}$.

3.2 Deriving total Gas Maps

The total gas surface density, Σ_{gas}, is the sum of the atomic gas surface density, Σ_{HI}, from THINGS and the molecular gas surface density, Σ_{H2}, from HERA and BIMA SONG (ionized gas is not considered). Where Σ_{H2} is below the sensitivity limit (see § 3.1), $\Sigma_{\mathrm{gas}} = \Sigma_{\mathrm{HI}}$ is assumed, which is formally a lower limit. This is always the case in the outer galaxy disks (see § 5). These quantities all have units of $\mathrm{M}_\odot\ \mathrm{pc}^{-2}$

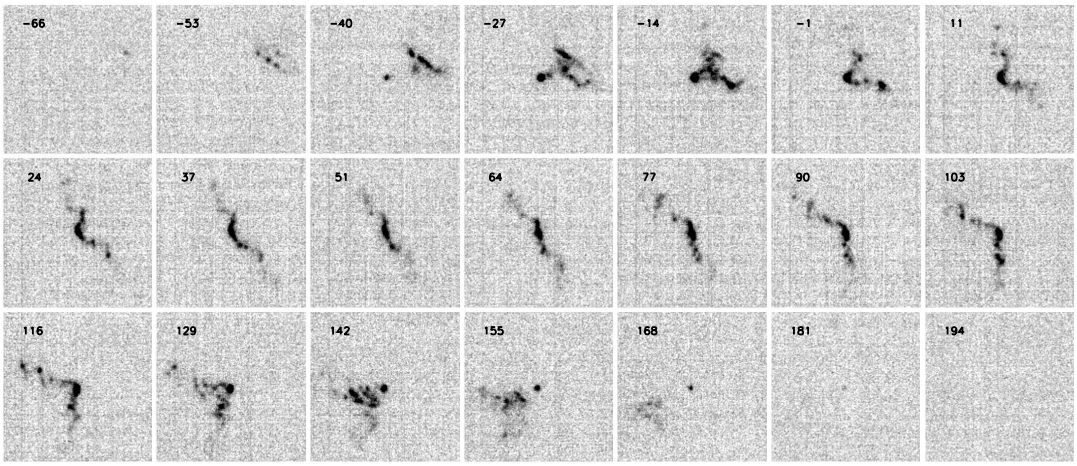

Figure 3.3: HERA channel maps for NGC 6946. Each panel shows the emission within a velocity channel and covers the same patch on the sky like the intensity map for NGC 6946 in Figure 3.2. The number in the upper left corner provides the central velocity of each channel. The systemic velocity of NGC 6946 is 48 km/s.

and are *hydrogen* surface densities, i.e. they do not include any contribution from helium. To scale the quoted surface densities to account for helium, one should multiply them by a factor of ~ 1.36. All surface and column densities quoted in this thesis have been corrected for the inclinations given in Table 2.1.

The adopted CO line ratio for the HERA data is $I(2 \rightarrow 1)/I(1 \rightarrow 0) = 0.89$, the mean value for the centers of 36 nearby galaxies (Braine et al., 1993). To convert from $\Sigma_{\rm CO}$ to $\Sigma_{\rm H2}$, a CO-to-H_2 conversion factor of 2.0×10^{20} cm^{-2} (K km s^{-1})$^{-1}$ is used. This value is appropriate for the Milky Way according to γ-ray and FIR studies (e.g. Strong & Mattox, 1996; Dame et al., 2001), but slightly lower than the conversion factor suggested by virial mass methods (e.g. Solomon et al., 1987; Blitz et al., 2007). Any changes in the conversion factor with metallicity or other environmental factors is neglected. For comparison, the applied conversion factor is identical to the one adopted by Wong & Blitz (2002), but Kennicutt (1998) adopts a higher value of 2.8×10^{20} cm^{-2} (K km s^{-1})$^{-1}$.

3.3 GALEX FUV Data

FUV data from the 'GALEX Nearby Galaxy Survey' (NGS, Gil de Paz et al., 2007) is used to estimate $\Sigma_{\rm SFR}$ (see § 3.5). The GALEX observatory provides simultaneous imaging in a far UV (FUV) and a near UV (NUV) broadband filter. The FUV band covers the wavelength range 1350 - 1750 Å, the NUV covers 1750 - 2800 Å. The angular resolutions (FWHM) are 4.0" and 5.6" for the FUV and the NUV respectively, and the field-of-view of the instrument is 1.25 °. For technical details on the detector and data products see Morrissey et al. (2005).

A single set of foreground stars is removed from the GALEX and 24μm maps (see § 3.4). Foreground stars are prominent in the NUV images, which are not explicitly

used in this thesis, but much less so in the FUV images, and they are easily identified via their UV colors. Star candidates are found in the NUV maps by applying an NUV/FUV ratio cut of $NUV/FUV > 10$. We apply this to all emission above $5\,\sigma$ in the NUV maps, below this stars cannot be distinguished from noise. In a few cases, a cut-off higher than $NUV/FUV > 10$ was necessary to remove particularly bright foreground stars.

A small background can be identified from the FUV maps and is subsequently removed. This is measured away from the galaxy by discarding emission with intensities $> 3\sigma$ above the median value of the image. The background adopted is the median of this residual map and is subsequently subtracted from the original map. The backgrounds in the GALEX maps are very well behaved and this simple subtraction yields good results in most cases. For three galaxies — NGC 4214, NGC 5194 (M51), and NGC 6946 — portions of the map that show the edge of the GALEX field-of-view, obvious artifacts, or bright stars not entirely removed by the color-cut (including M51b) are blanked. These are usually away from the galaxy and have minimal impact on this study.

The FUV maps are corrected for the effects of Galactic extinction. $\mathrm{E}(B-V)$ is estimated from the extinction maps of Schlegel, Finkbeiner & Davis (1998) and converted to FUV extinction using $\mathrm{A}_{FUV} = 8.24 \times \mathrm{E(B\text{-}V)}$ (Wyder et al., 2007).

3.4 *Spitzer* Space Telescope 24 μm Data

FUV data are heavily affected by internal extinction. To estimate the amount of star formation obscured by dust (see § 3.5), 24 μm data are used. They were obtained by the '*Spitzer* Infrared Nearby Galaxies Survey' (SINGS, Kennicutt et al., 2003). The map of NGC 4214 comes from the public archive. These data are scan maps taken with the MIPS instrument on board the *Spitzer* Space Telescope (Rieke et al., 2004). Full details of the observing strategy and target sensitivity are described by (Kennicutt et al., 2003).

The SINGS observations were designed to detect emission out to the optical radius and in most of our targets this goal was achieved. The FWHM of the MIPS PSF at 24 μm is 6", though the beam is substantially non-Gaussian outside the central peak. This is only a minor concern for this study because to achieve a common spatial resolution for all data, we work with a typical angular resolution of ~ 20".

The following additional processing is performed on the SINGS maps: First, a region is blanked at the edges of the scan maps parallel to the direction of the scan; in these regions the noise increases and artifacts are more common. Also, stars that were identified from the GALEX images are blanked. Eventually, a background is subtracted which is usually quite small, using the same procedure as for the GALEX images. In a few maps – Ho I, NGC 3521 and NGC 6946 – regions with unreliable background can be identified which are subsequently blanked by hand. These regions are usually far away from the galaxy and so have minimal effect on this analysis.

3.5 Star Formation Rate Surface Density Maps

Throughout this thesis, star formation rate surface densities, $\Sigma_{\rm SFR}$, are measured in units of $M_\odot$ yr^{-1} kpc^{-2}. For the analysis of the star formation law across the optical disks of galaxies (see § 4), such maps are obtained by combining FUV and 24μm maps. The GALEX FUV images trace predominantly O and early B stars and therefore offer a picture of recent, unobscured star formation. FUV emission can be heavily affected by dust, however, making it difficult to derive unbiased measurements of $\Sigma_{\rm SFR}$ from the FUV alone. Fortunately, the dust that obscures the FUV emission from young stars is heated and reradiates in the mid-infrared. The 24 μm maps thus allow to estimate the amount of ongoing dust-obscured star formation.

This approach was proposed and validated for individual star forming regions and large portions of galactic disks by Calzetti et al. (2007) and Kennicutt et al. (2007). They showed that 24 μm emission could be used to accurately estimate the amount of extinction that affects Hα emission. Here, an analogous approach is used: FUV and 24 μm emission is combined using the following formula:

$$\begin{aligned} \Sigma_{\rm SFR}\left[{\rm M}_\odot\ {\rm yr}^{-1}\ {\rm kpc}^{-2}\right] &= 3.2\times10^{-3} I_{24}\left[{\rm MJy\ ster}^{-1}\right] \\ &+ 8.1\times10^{-2} I_{FUV}\left[{\rm MJy\ ster}^{-1}\right]\ , \end{aligned} \tag{3.1}$$

where $\Sigma_{\rm SFR}$ denotes the star formation rate surface density, and I_{24} and I_{FUV} are the 24 μm and FUV intensities respectively. Leroy et al. (2008) motivate the choice of coefficients in Equation 3.1. $\Sigma_{\rm SFR}$ derived from Equation 3.1 agree well with values derived using the Hα + 24 μm calibration from Calzetti et al. (2007) at 750 pc resolution and when $I_{24} = 0$, Equation 3.1 reduces to the FUV-SFR calibration by Salim et al. (2007). Furthermore, so-derived SFRs integrated over whole galaxies as well as in radial profiles also agree well with those based on extinction-corrected Hα emission alone.

Following this approach, we create maps of $\Sigma_{\rm SFR}$. The RMS noise varies from map to map, but a typical limit for the sensitivity of the SFR maps is $\approx 1\times10^{-4}$ $M_\odot\,{\rm yr}^{-1}\,{\rm kpc}^{-2}$. The derived values of $\Sigma_{\rm SFR}$ assume the IMF of Kroupa (2001). To convert to the truncated Salpeter (1955) IMF adopted by e.g. Kennicutt (1989, 1998) or Kennicutt et al. (2007), one should multiply the $\Sigma_{\rm SFR}$ quoted in this work by a factor of 1.5.

Because this particular combination of FUV and mid-IR maps is new, the results were compared to those obtained using maps of Hα and Hα+24μm wherever these are available. The Hα maps are from the SINGS Data Release 4. Backgrounds are fit and removed from these maps and any region with a particularly problematic background is masked out. A correction for [NII] in the bandpass following Calzetti et al. (2007) and a correction for Galactic extinction using the dust maps of Schlegel, Finkbeiner & Davis (1998) is also performed.

Chapter 4

The Resolved Star Formation Law across the Optical Disks of Galaxies

As indicated in § 1, a large range of power-law indices, $N \approx 1$–3, have been derived in the literature to relate $\Sigma_{\rm SFR}$ to $\Sigma_{\rm gas}$ via a Schmidt-type power law. This study assesses the star formation law systematically pixel-by-pixel on high spatial resolution in a representative set of nearby galaxies to look into the question of whether different star formation (SF) laws exist in different galaxies or whether N is very sensitive to systematic differences in methodology (e.g. the choice of SFR tracers, the spatial resolution of the data, etc.). Another currently open question that this study deals with is whether the Schmidt law is fundamentally a molecular phenomenon or if a single, universal power law relates total gas and star formation. Because all stars are believed to form in molecular clouds, it would seem natural that H_2 and SF are more immediately related than HI or total gas and SF. Therefore it is somewhat surprising that observations remain contradictory on this point so far.

This analysis is therefore organized as follows: The galaxy sample will be introduced and the procedure to convert the data (see § 2 and § 3), into physical units are presented in § 4.1. The process used to generate a set of independent measurements over the disk of each galaxy will also be described. In §4.2 we show the observed relationships between $\Sigma_{\rm HI}$, $\Sigma_{\rm H2}$, and $\Sigma_{\rm SFR}$ for individual galaxies. We carry out power law fits to each distribution and assess whether there is a common Schmidt law shared by all of our galaxies. We show results for spirals and HI-dominated late-type galaxies separately to highlight the range of environments in our sample. In §4.3 we combine our galaxies into two data sets (spirals and HI-dominated galaxies) to draw general conclusions about HI, H_2, and the SFR. In §4.4 we explore the effect of environment by comparing the Schmidt law in the inner, H_2-dominated parts of spirals to their HI-dominated outer disks and to HI-dominated dwarf and late-type galaxies. We show that the relationship between total gas and SFR is a clear function of environment and fit the radial dependence of the molecular-to-atomic gas ratio in spirals. In §4.5 we summarize our results and give our conclusions.

4.1 Sample, Data, Units, and Measurements

4.1.1 Sample

Our sample of spiral galaxies is the overlap of THINGS, SINGS, the GALEX 'Nearby Galaxy Survey' and the HERA or BIMA-SONG CO surveys. Galaxies that are known to be HI-dominated are not required to be part of HERA or BIMA-SONG. This ensures that we measure at least the dominant component of the neutral ISM and the SFR along most lines of sight. Table 4.1 lists our sample along with their adopted properties: distance, inclination, position angle, radius and morphology. We separate the galaxies into two groups: 8 large spiral galaxies that have H_2-dominated ISMs in their centers and and 11 late-type galaxies that are HI-dominated throughout.

We do not study galaxies with inclinations $> 70°$ that would otherwise qualify for the sample. High inclinations yield very few sampling points and result in a beam elongated parallel to the minor axis in the plane of the galaxy, making fits difficult to carry out and interpret. We also do not include any galaxies more distant than 12 Mpc. This is the maximum distance at which the typical angular resolution of our data (see below) corresponds to our common spatial resolution of 750 pc.

We work without CO maps for 4 late-type spirals, NGC 925, NGC 2403, NGC 2976, NGC 4214 and 7 dwarf irregular galaxies. For most of these galaxies, the CO content is either measured or constrained by a significant upper limit: major axis profiles by Young et al. (1995) for NGC 925, NGC 2403, and NGC 2976 (which is also part of BIMA SONG); Kitt Peak 12m mapping of the inner disk of NGC 2403 (Thornley & Wilson, 1995); OVRO mapping of NGC 4214 by Walter et al. (2001); single dish pointings toward NGC 4214, Holmberg I and DDO 154 by Taylor et al. (1998); central pointings for DDO 053, IC 2574, and Holmberg II by Leroy et al. (2005). In each case, the ISM is well-established to be HI-dominated. M81 DwA and M81 DwB, two extremely low-mass dwarf irregular companions to M81, both lack CO measurements, but should also be HI-dominated. Of these galaxies, 8 have absolute B-band magnitudes fainter than -18 mag and maximum rotation velocities $\lesssim 100$ km s^{-1} (i.e. the mass of the LMC or less). NGC 925 and NGC 2403 have $M_B \sim -20$ mag and maximum rotational velocities ~ 100 km s^{-1}; they are probably intermediate in mass between the LMC and M 33.

4.1.2 Alignment, Units, and Convolution

From the data described in § 2 and § 3, we construct maps of star formation rate surface density, $\Sigma_{\rm SFR}$, atomic hydrogen surface density, $\Sigma_{\rm HI}$, molecular hydrogen surface density, $\Sigma_{\rm H2}$, and total gas surface density, $\Sigma_{\rm gas}$.

We place all of these maps on the THINGS astrometric grid (pixel scale: 1.5") at a common spatial resolution of 750 pc. We carry out most of our work at 750 pc resolution but also create versions of each map at a range of spatial resolutions from the native resolution to 10 kpc (in steps of 50 pc below 1 kpc, and 500 pc up to 10 kpc). When degrading the resolution of a map, we convolve with a circular Gaussian beam (on the sky) and take no account of the inclination of the galaxy. For

Galaxy	D [Mpc]	i [deg]	PA [deg]	r_{25} [arcmin]	Hubble type
HI-dominated Galaxies					
DDO 154	4.30	66.0	229.7	0.97	Irr
DDO 53	3.56	31.0	132.0	0.39	Irr
Ho I	3.84	12.0	50.0	1.66	Irr
Ho II	3.39	41.0	177.0	3.30	Irr
IC 2574	4.02	53.4	55.7	6.44	SABm
M 81 DwA	3.55	23.0	49.0	0.63	Irr
M 81 DwB	5.30	44.0	321.0	0.56	Irr
NGC 0925	9.16	66.0	286.6	5.36	Scd
NGC 2403	3.22	62.9	123.7	7.92	SABc
NGC 2976	3.56	64.5	334.5	3.62	Sc
NGC 4214	2.94	43.7	65.0	3.38	Irr
Spirals With H_2-Dominated Centers					
NGC 0628	7.30	7.0	20.0	4.89	Sc
NGC 3184	11.10	16.0	179.0	3.71	SABc
NGC 3521	10.70	72.7	339.8	4.16	SABb
NGC 3627	9.25	61.8	173.0	5.12	SABb
NGC 4736	4.66	41.4	296.1	3.88	Sab
NGC 5055	10.10	59.0	101.8	5.87	Sbc
NGC 5194	8.00	42.0	172.0	3.88	Sbc
NGC 6946	5.90	32.6	242.7	5.74	SABc

Table 4.1: Galaxy sample. See Walter et al. (2008) for further information on individual galaxies and for references to the values quoted in this table.

a given spatial resolution, this exercise may be thought of as placing every galaxy in the sample at the same distance.

4.1.3 Gas Surface Density Maps

The total gas surface density, $\Sigma_{\rm gas}$, is the sum of the atomic gas surface density, $\Sigma_{\rm HI}$, and the molecular gas surface density, $\Sigma_{\rm H2}$ (we do not consider ionized gas). Where $\Sigma_{\rm H2}$ is below the sensitivity limit (see § 3.1), we take $\Sigma_{\rm gas} = \Sigma_{\rm HI}$, which is formally a lower limit. These quantities all have units of $M_\odot$ pc^{-2}. These are *hydrogen* surface densities, i.e. they do not include any contribution from helium. To scale our quoted surface densities to account for helium, one should multiply them by a factor of ~ 1.36. All surface and column densities quoted in this paper have been corrected for the inclinations given in Table 4.1.

4.1.4 Individual Data Points

With maps of $\Sigma_{\rm HI}$, $\Sigma_{\rm H2}$, and $\Sigma_{\rm SFR}$(see § 3.5) in hand, the next step is to generate individual data points. We compare these quantities over the entire optical disk of each galaxy, out to $r_{25} = d_{25}/2$. This is a departure from previous studies, which used integrated measurements over galaxy disks (e.g. Kennicutt, 1989, 1998), radial profiles (Wong & Blitz, 2002, e.g.), or apertures centered on star forming peaks (e.g. Kennicutt et al., 2007).

We choose r_{25} as an outer cut. Most star formation takes place within this radius (e.g. see the profiles of Martin & Kennicutt, 2001; Wong & Blitz, 2002) and our FUV, 24μm, and HI maps detect emission at $> 3\sigma$ over most of this area. This outer radius cut at r_{25} takes into account the inclination and position angle of the galaxy; that is, this is a cut in deprojected galactocentric radius. The ellipses in Figure 4.1 show the projected optical radius, i.e. the extent of the region that we study, on the THINGS HI and $\Sigma_{\rm SFR}$ maps.

We draw independent data points from our maps so that each data point corresponds to non-overlapping resolution elements and the data together cover the optical disk. This may be thought of as either reducing the oversampled map (rebinning the map) so that 1 pixel corresponds to a resolution element or as covering the disk with non-overlapping apertures equal in size to a resolution element. For each independent data point we measure $\Sigma_{\rm HI}$, $\Sigma_{\rm H2}$, $\Sigma_{\rm gas} = \Sigma_{\rm HI} + \Sigma_{\rm H2}$, and $\Sigma_{\rm SFR}$.

When convolving the maps with progressively larger beams (see § 4.1.2), flux from outside the outer radius cut (r_{25}) would be convolved into the optical disk. To avoid this, the outer radius cut we use will be decreased by half a beam width and is actually $r_{max} = r_{25} - 0.5\,\theta_{\rm beam}$, where θ_{beam} is the FWHM of the beam in the same units as the radius. Note that $\theta_{\rm beam}$ is subtracted in the plane of the sky, not the plane of the galaxy because the convolution takes place in the plane of the sky.

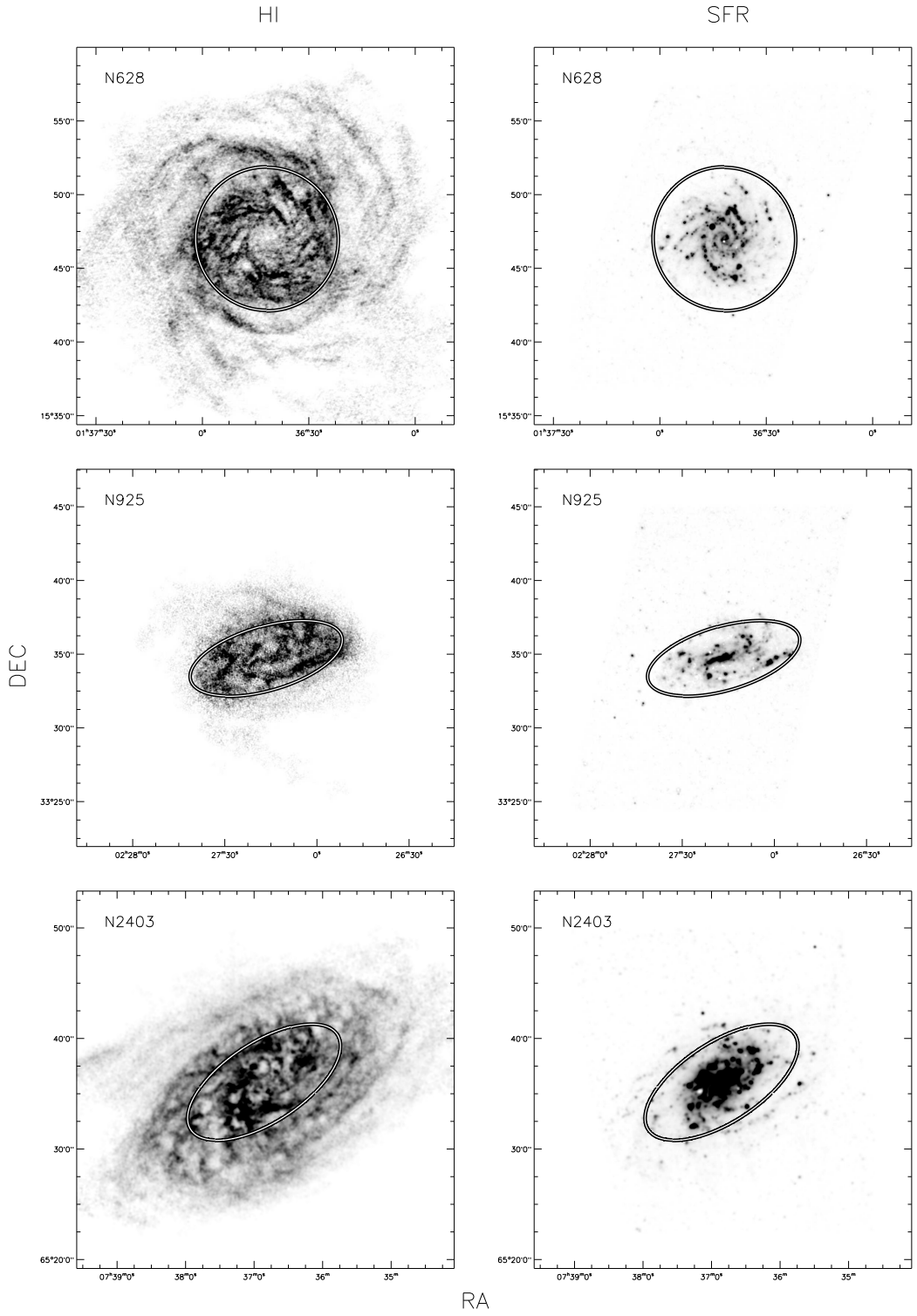

Figure 4.1: Maps of $\Sigma_{\rm HI}$ (left) and $\Sigma_{\rm SFR}$ (right) at the best available resolution for our sample of 8 spiral galaxies with H_2-dominated centers and the 2 largest HI-dominated galaxies, NGC 925 and NGC 2403. The ellipse indicates the optical radius (r_{25}), within which we compare $\Sigma_{\rm HI}$, $\Sigma_{\rm H2}$, and $\Sigma_{\rm SFR}$. Almost all star formation occurs within this radius, although the HI often extends much beyond r_{25}.

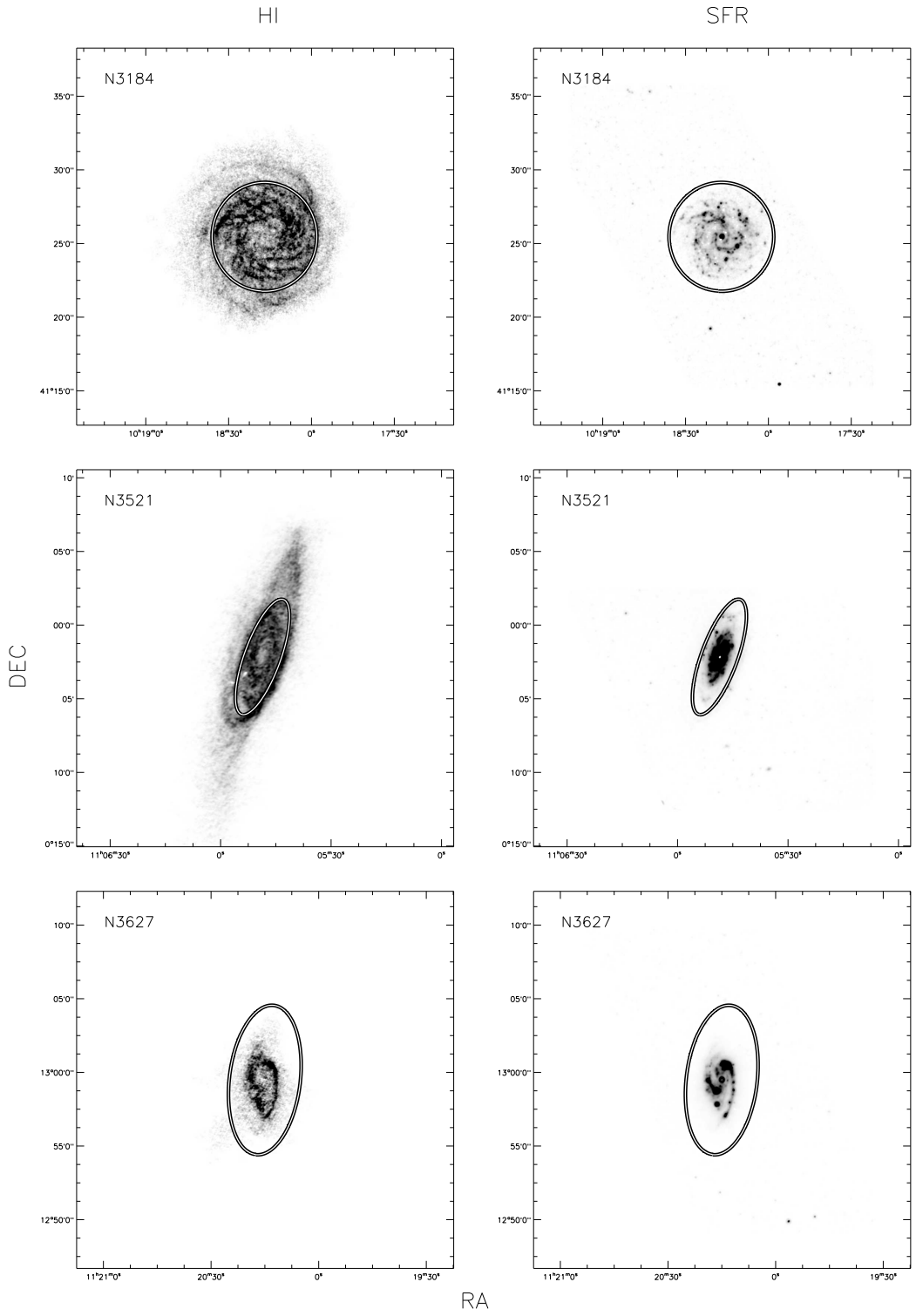

Figure 4.1: continued.

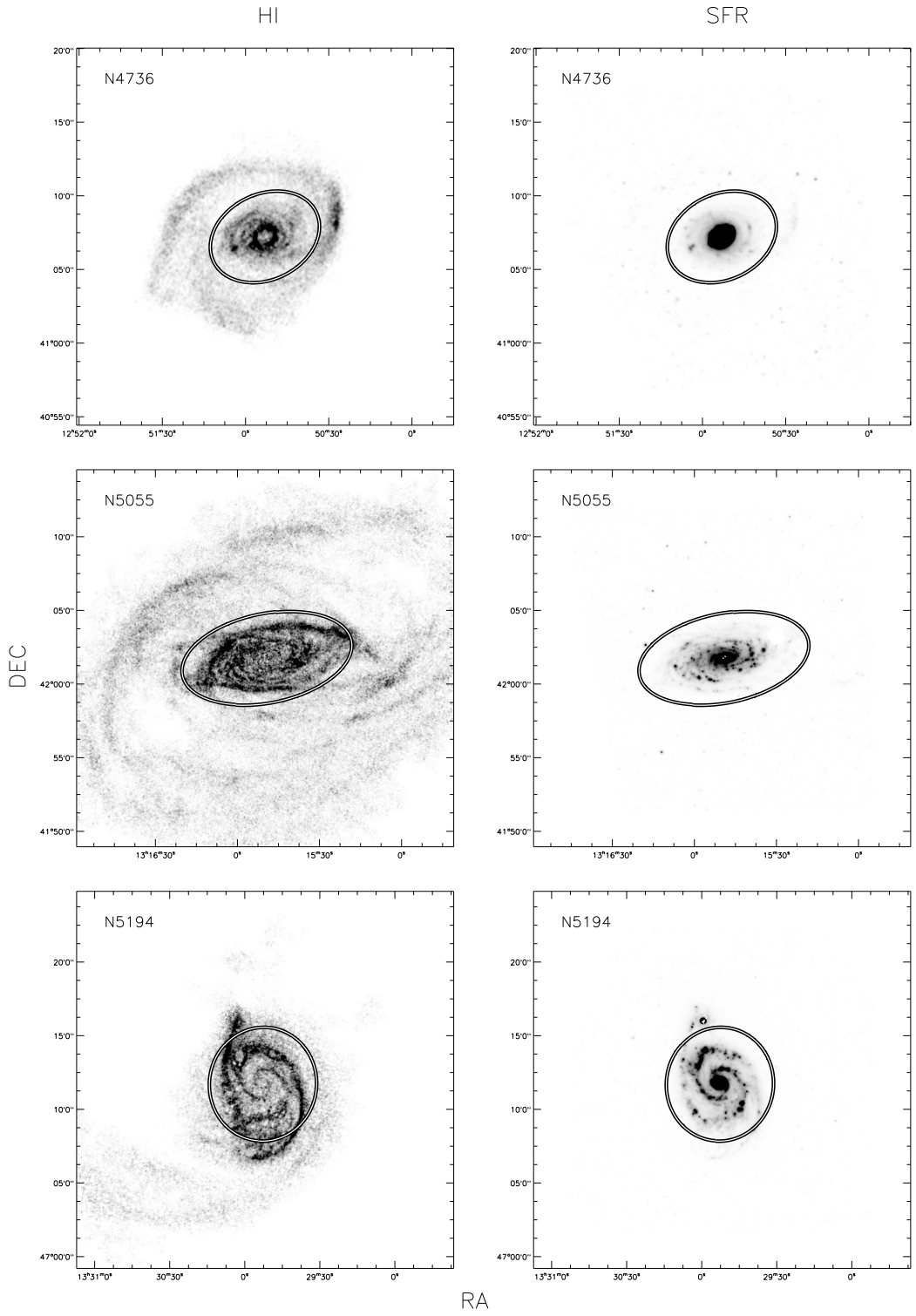

Figure 4.1: continued.

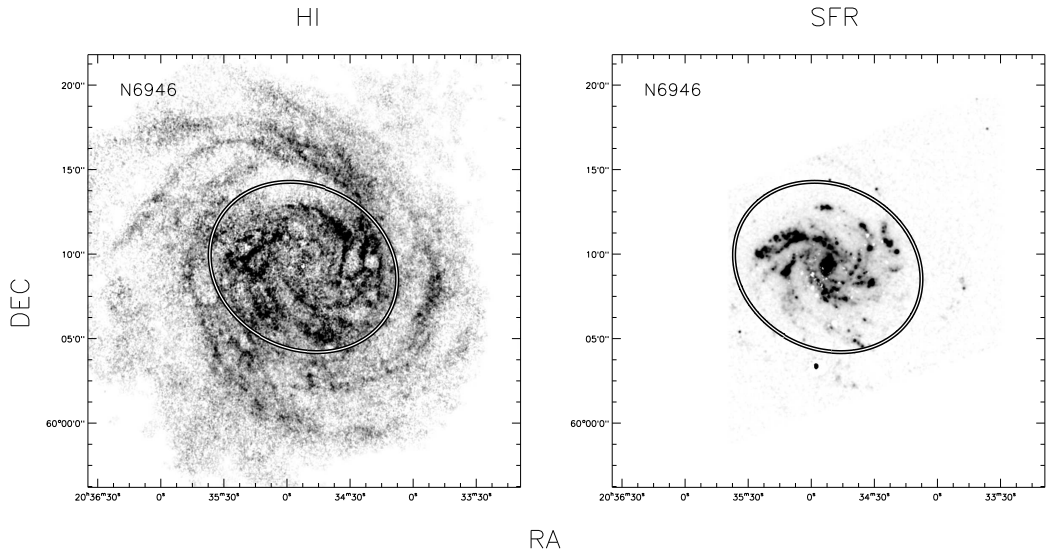

Figure 4.1: continued.

4.1.5 Radial Profiles

We also extract from our maps radial profiles of $\Sigma_{\rm HI}$, $\Sigma_{\rm H2}$, and $\Sigma_{\rm SFR}$ and examine them along with the pixel-by-pixel data. These are mean values within 60° of the major axis taken across tilted rings that use the parameters in Table 4.1. We show the profiles for spirals and HI-dominated galaxies in Figures 4.2 and 4.3. These plots show $\Sigma_{\rm SFR}$, $\Sigma_{\rm HI}$ and $\Sigma_{\rm H2}$ as a function of galactocentric radius. The bottom axis indicates the radius normalized by r_{25}. The top axis gives the radius in kiloparsecs. Each point represents the average value in an individual 10″-wide tilted ring using the structure parameters given in Table 4.1. For the HI-dominated galaxies, we show only $\Sigma_{\rm SFR}$ and $\Sigma_{\rm HI}$.

4.2 The Star Formation Law in Individual Galaxies

Figure 4.4 shows the relationship between gas and and star formation surface densities in individual spiral galaxies. Color contours show the results from pixel–by–pixel sampling the optical disks of the 8 spiral galaxies in our sample. Each row shows results for a different galaxy. The columns left to right show $\Sigma_{\rm SFR}$ on the y-axis as a function of $\Sigma_{\rm HI}$ (left), $\Sigma_{\rm H2}$ (middle), and $\Sigma_{\rm gas}$ (right) on the x-axis. Shading shows the density of data points in cells of size 0.05 dex wide (in both axes). Green, orange, red, and magenta cells show contours of 1, 2, 5, and 10 sampling points per cell. Individual cells that are not connected and contain only 1 data point are marked in grey. All data in Figure 4.4 are at a common resolution of 750 pc.

We plot points from the radial profiles (Figures 4.2 and 4.3) on the same plot as black crosses. Generally speaking, the radial profile data lie near the middle of

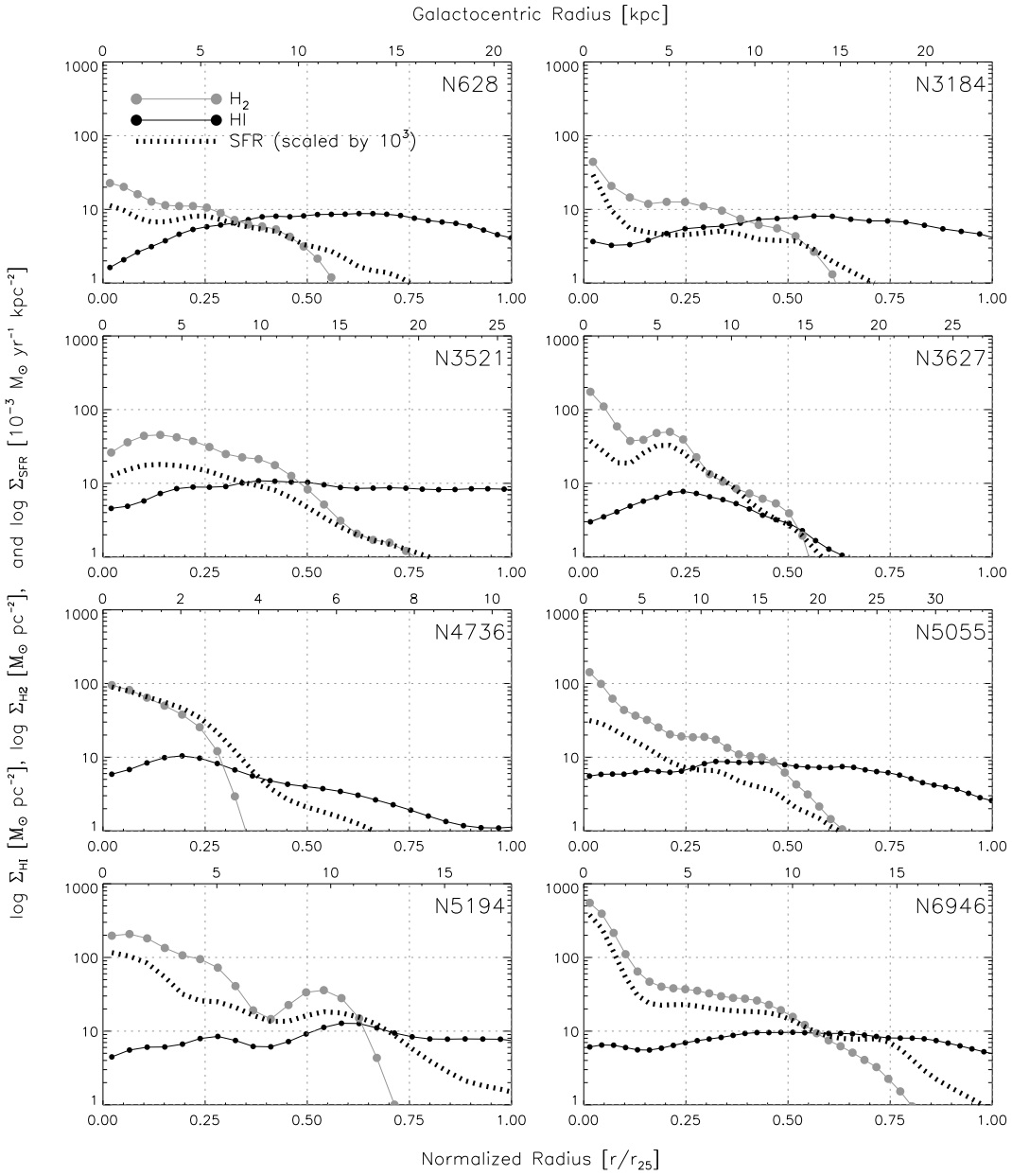

Figure 4.2: Azimuthally averaged radial profiles of $\Sigma_{\rm HI}$, $\Sigma_{\rm H2}$, and $\Sigma_{\rm SFR}$ for spiral galaxies with H_2-dominated centers. The y-axis shows $\Sigma_{\rm HI}$ and $\Sigma_{\rm H2}$ in units of $M_\odot$ pc^{-2} or $\Sigma_{\rm SFR}$ in units of 10^{-3} $M_\odot$ yr^{-1} kpc^{-2} (the scaling is chosen to bring the profiles onto the same plot). The x-axis shows Galactocentric radius (bottom) normalized by r_{25} and (top) in kiloparsecs. Profiles of $\Sigma_{\rm SFR}$ and $\Sigma_{\rm H2}$ are strongly covariant. $\Sigma_{\rm HI}$ varies weakly over the optical disk with the main features often being a central depression and a universal upper limit of $\Sigma_{\rm HI} \sim 9$ $M_\odot$ pc^{-2}.

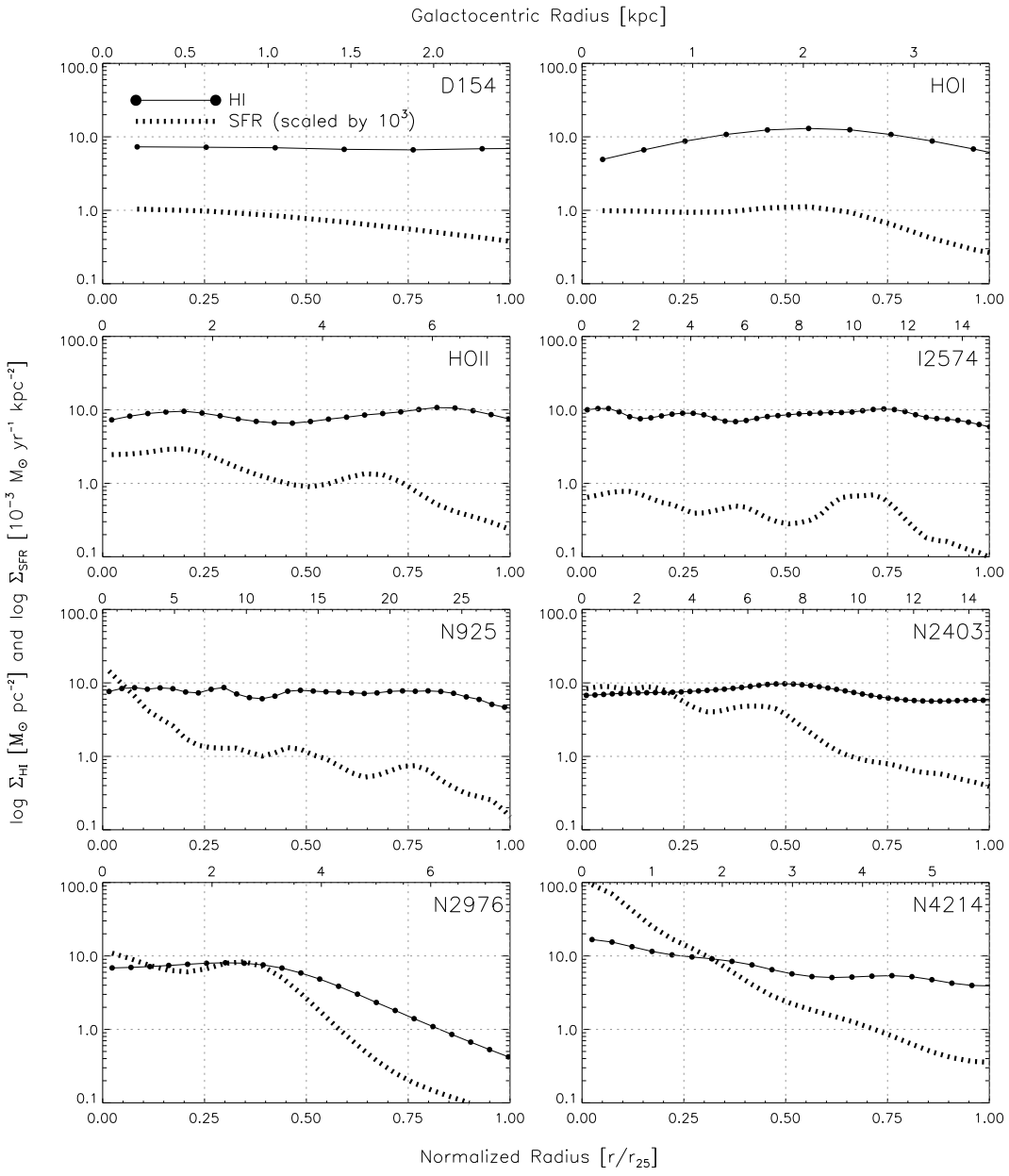

Figure 4.3: Azimuthally averaged radial profiles of $\Sigma_{\rm HI}$ and $\Sigma_{\rm SFR}$ for 8 of our 11 HI-dominated galaxies, all late-type spirals or dwarf irregulars. The y-axis shows $\Sigma_{\rm HI}$ in units of $\rm M_\odot$ $\rm pc^{-2}$ or $\Sigma_{\rm SFR}$ in units of $10^{-}3$ $\rm M_\odot$ $\rm yr^{-1}$ $\rm kpc^{-2}$ (the scaling is chosen to bring the profiles onto the same plot). The x-axis shows Galactocentric radius (bottom) normalized by r_{25} and (top) in kiloparsecs. $\Sigma_{\rm HI}$ shows the same maximum value seen in spiral galaxies and similarly flat profiles.

the distribution of the pixel-by-pixel data, as expected. In many cases, features at high $\Sigma_{\rm gas}$ and high $\Sigma_{\rm SFR}$ are clearer in the radial profile data because small central rings with high surface densities have small areas and thus contribute only a few individual points to the pixel-by-pixel data.

A common way to parameterize the relationship between star formation and gas is via the gas depletion time or its inverse, the star formation efficiency SFE = $\Sigma_{\rm SFR}/\Sigma_{\rm gas}$. This is the time needed for the present rate star formation to consume the existing gas reservoir. In Figure 4.4, we plot levels of constant depletion time/SFE as diagonal dotted lines. From bottom to top, these correspond to gas depletion times of 10^{10}, 10^{9} and 10^{8} years or equivalently depleting 1%, 10% and 100% of the gas reservoir per 10^{8} years; these values include helium and so are true depletion times.

4.2.1 Fits To $\Sigma_{\rm SFR}$ Versus $\Sigma_{\rm gas}$

Solid black lines in Figure 4.4 show the results of fitting a power-law of the form

$$\Sigma_{\rm SFR} = a \left(\frac{\Sigma_{\rm gas\ or\ H2}}{10\ {\rm M}_\odot\ {\rm pc}^{-2}} \right)^N . \tag{4.1}$$

using the ordinary least–squares (OLS) bisector. The free parameters are the power law index, N, and a, which is $\Sigma_{\rm SFR}$ at the fiducial gas surface density of 10 $\rm M_\odot\ pc^{-2}$. Figure 4.4 and Table 4.2 give the best fit values of N, $A = \log_{10} a$, and the RMS scatter in $\log \Sigma_{\rm SFR}$ about the fit. Because there is not a clear independent variable, we carry out the fit using the OLS bisector (Isobe et al., 1990) with equal weighting to each point. We treat the problem in log space, where fitting a line yields N as the slope and $A = \log_{10} a$ as the intercept. By centering the fit at 10 $\rm M_\odot\ pc^{-2}$, a surface density near the middle of our range, we minimize the covariance between N and a (N.B. readers interested in comparison with previous work should take note of this difference, most fits in the literature quote 'A' at 1 $\rm M_\odot\ pc^{-2}$ rather than our fiducial 10 $\rm M_\odot\ pc^{-2}$).

We fit $\Sigma_{\rm SFR}$ vs. $\Sigma_{\rm H2}$ (middle panel) in the regime $\Sigma_{\rm H2} > 3\ {\rm M}_\odot\,{\rm pc}^{-2}$ for the HERA data and $\Sigma_{\rm H2} > 10\ {\rm M}_\odot\,{\rm pc}^{-2}$ for the BIMA SONG data. These sensitivities are shown as dotted vertical lines in the middle panels of Figure 4.4. We fit $\Sigma_{\rm SFR}$ vs. $\Sigma_{\rm gas}$ to all data points (right panel). The formal errors on the fits are small and the fits are robust to the removal of individual data points. We test the latter via bootstrapping (i.e. repeatedly drawing a new, equal-sized, random subsample from our data allowing repetition) and find the resulting uncertainties to be typically ~ 0.01 in N and ~ 0.05 in A. Methodology, e.g. the decision to fit X vs. Y, Y vs. X, or use the OLS bisector, drives the resulting fits as much as any other statistical factor. Because both variables are independent, we use the OLS bisector, but estimate the uncertainty by carrying out ordinary least-squares (OLS) fits of $\Sigma_{\rm SFR}$ vs. $\Sigma_{\rm H}$ and $\Sigma_{\rm H}$ vs. $\Sigma_{\rm SFR}$. The differences in N and A that we obtain are taken as the uncertainties on the fit. We find that this brackets the range of reasonable 'by eye' fits well. We note that these uncertainties represent only the uncertainty in fitting the data as are. They do not reflect systematics such as uncertainty or variations in the CO-to-H_2 conversion factor, the IMF, etc.

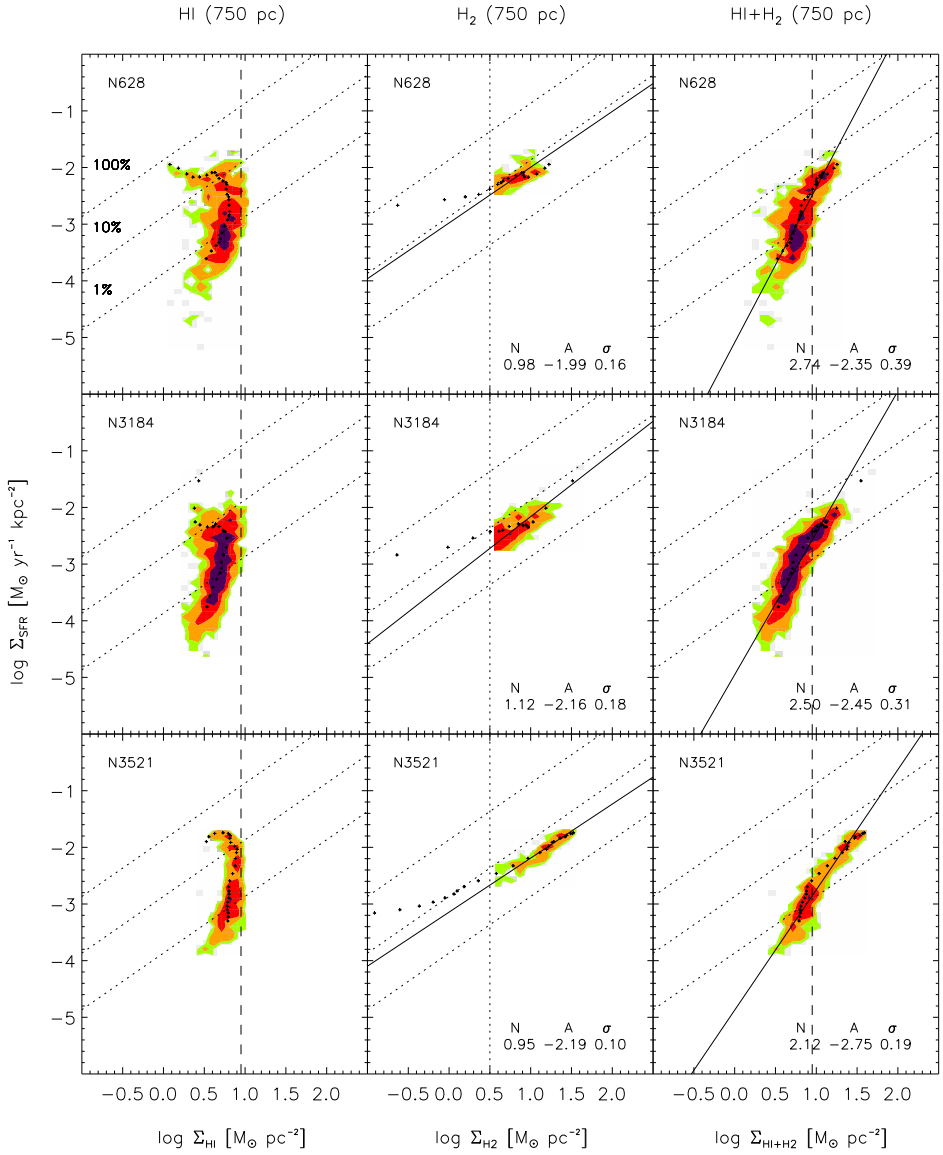

Figure 4.4: $\Sigma_{\rm SFR}$ as a function of $\Sigma_{\rm HI}$ (left), $\Sigma_{\rm H2}$ (middle), and $\Sigma_{\rm gas} = \Sigma_{\rm HI} + \Sigma_{\rm H2}$ (right) in spiral galaxies at 750 pc resolution. Each row shows results for one galaxy. Green, orange, red, and magenta cells show contours of 1, 2, 5, and 10 independent data points per 0.05 dex-wide cell (for H_2 in NGC 4736 we use a scatter plot due to the low number of sampling points.). Crosses show average measurements over tilted rings from the radial profiles. Dashed vertical lines in the HI (left) and total gas (right) plots show the surface density where the HI saturates (see § 4.2.5). Dotted vertical lines in the middle plots show the typical sensitivity for our CO data. We show OLS bisector fits to the H_2 and total gas data with a solid line and quote the results. Diagonal lines show constant gas depletion times (or star formation efficiencies) taking helium into account, from top to bottom: 10^8, 10^9, and 10^{10} yrs.

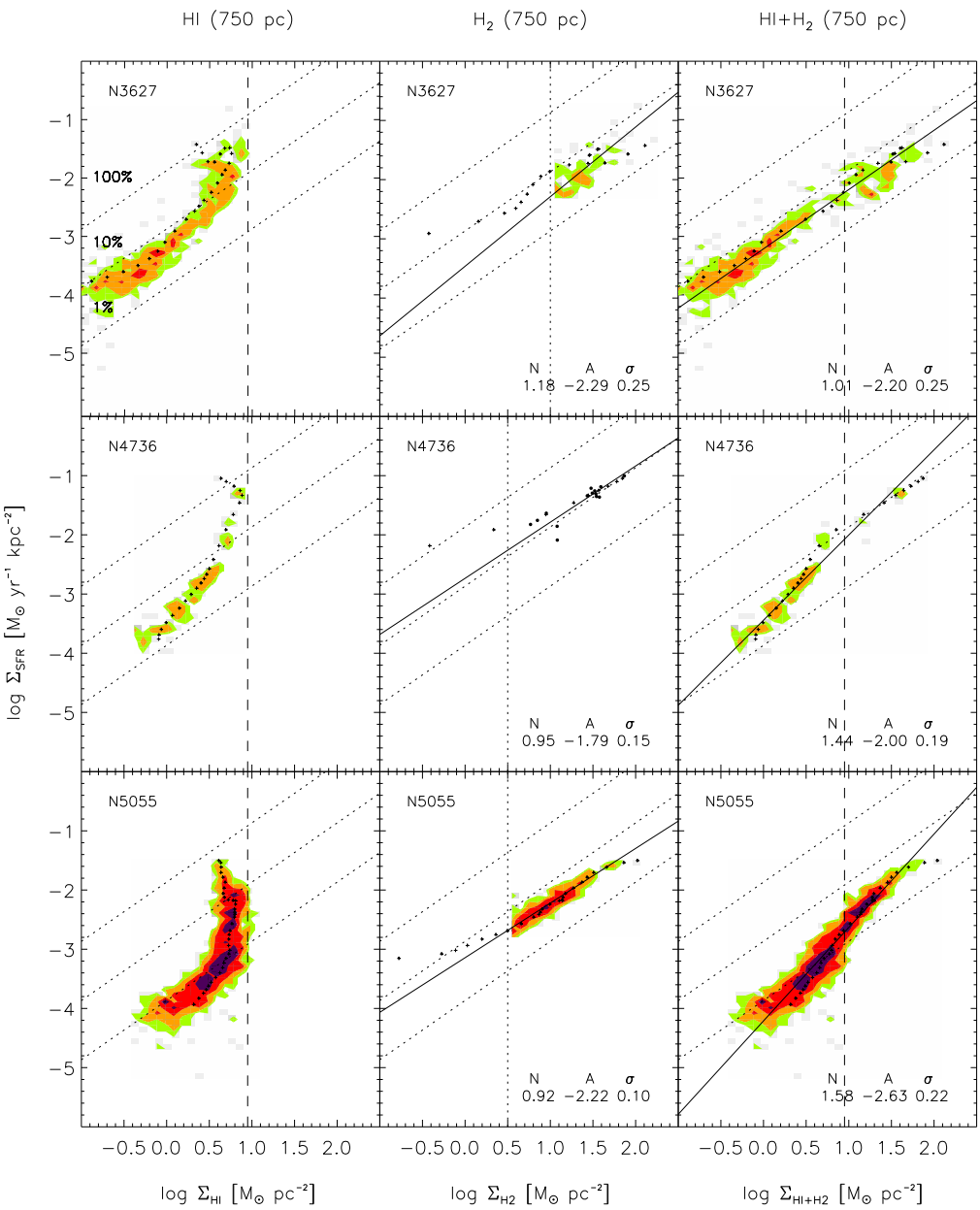

Figure 4.4: continued.

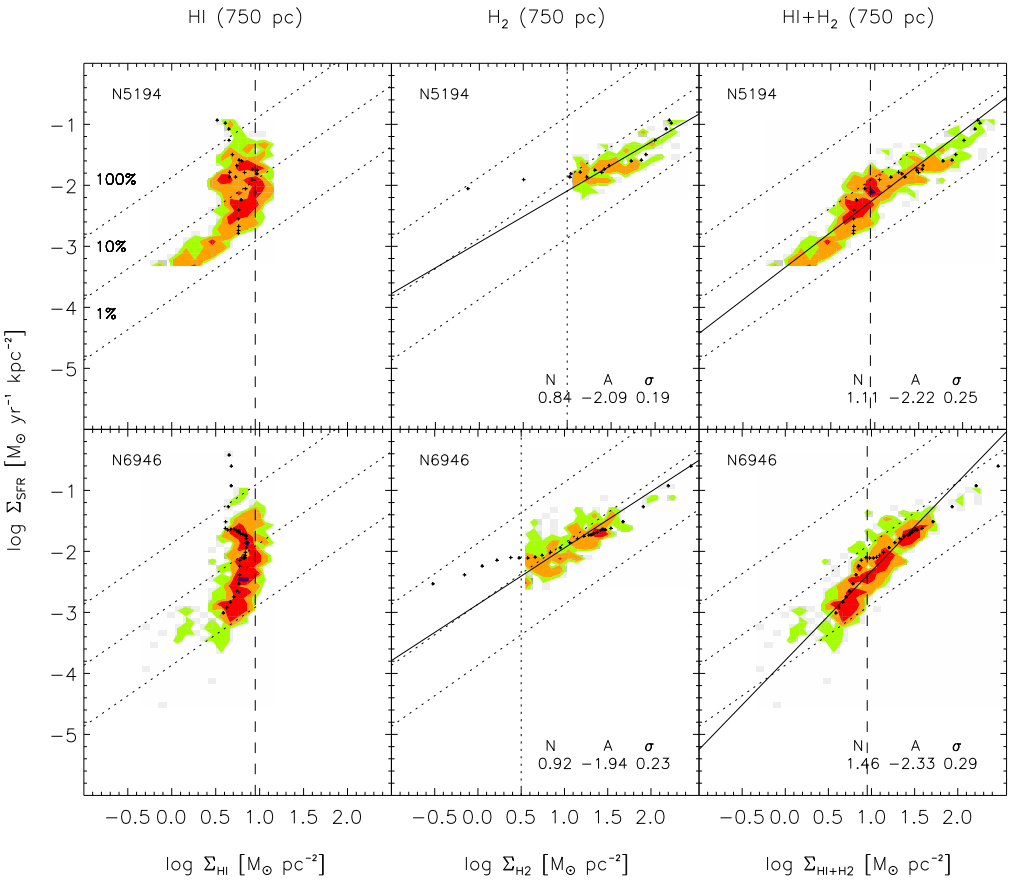

Figure 4.4: continued.

	H_2			$HI + H_2$		
Galaxy	Coefficient (A)	Index (N)	Scatter	Coefficient (A)	Index (N)	Scatter
N0628	-1.99	0.98	0.16	-2.35	2.74	0.39
N3184	-2.16	1.12	0.18	-2.45	2.50	0.31
N3521	-2.19	0.95	0.10	-2.75	2.12	0.19
N3627	-2.29	1.18	0.25	-2.20	1.01	0.25
N4736	-1.79	0.95	0.15	-2.00	1.44	0.19
N5055	-2.22	0.92	0.10	-2.63	1.58	0.22
N5194	-2.09	0.84	0.19	-2.22	1.11	0.25
N6946	-1.94	0.92	0.23	-2.33	1.46	0.29
Average	-2.08 ± 0.18	0.98 ± 0.11	...	-2.37 ± 0.26	1.74 ± 0.71	...

Table 4.2: Fitted Power-Law Parameters at 750 pc Resolution.

4.2.2 The Molecular Gas Schmidt Law

Fitting $\Sigma_{\rm SFR}$ to $\Sigma_{\rm H2}$ alone yields power law indices, N, near unity, 0.98 ± 0.11 and coefficients $A = -2.08 \pm 0.18$ with a typical scatter of ~ 0.2 dex. That is our 8 spirals display power law indices consistent with an $N = 1$ molecular Schmidt law and only mild variations in the normalization. Another statement of this is that the molecular gas in our sample shows a nearly constant ratio of $\Sigma_{\rm SFR}$ to $\Sigma_{\rm H2}$ that corresponds to star formation consuming the H_2 gas reservoir in $\approx 2 \times 10^9$ yrs (i.e. a constant gas depletion time; also see § 4.3.4).

4.2.3 The Total Gas Schmidt Law

The relationship between the $\Sigma_{\rm gas}$ and $\Sigma_{\rm SFR}$ show a much larger range of behavior as compared to the behavior with respect to H_2. The power law indices, N, for these fits range from 1.01 to 2.74 with the mean 1.74 ± 0.71 and a scatter of ~ 0.3 dex. This range is similar to that found by studies of individual galaxies in the literature ($0.9 < {\rm N} < 3.3$, see § 1). The fits are driven to this steep index by a sharp drop in $\Sigma_{\rm SFR}$ over a narrow range of surface densities just below $\Sigma_{\rm gas} \sim 9$ $M_\odot$ pc^{-2} (see § 4.2.5).

There is less variation in the coefficient, A, than in the power law index. A varies from -2.75 to -2.00 with a mean of -2.37 and an RMS scatter of 0.26. This is lower than $A = -2.08$ obtained for the molecular gas above as expected, given the apparently more direct link between molecular gas and star formation. The ratio of mean coefficients for the total gas and the H_2 is ~ 0.3 dex; that is, a particular surface density of molecular gas will form stars at about twice the rate of the same surface density of total gas.

It is further evident that there is no universal behavior in the right hand column of Figure 4.4. That is, the distribution of points in $\Sigma_{\rm gas}$-$\Sigma_{\rm SFR}$ parameter space varies from galaxy to galaxy. In some cases, e.g. NGC 5194, a single power law appears to relate the two. In other cases, e.g. NGC 3184, $\Sigma_{\rm SFR}$ and $\Sigma_{\rm gas}$ are essentially uncorrelated where $\Sigma_{\rm HI} > \Sigma_{\rm H2}$. In these cases, there is not a clear one-to-one relationship between total gas and SFR across the whole disk.

What causes some galaxies to display a power law spanning from the HI-dominated to H_2-dominated ISM while others do not? The data-driven answer is that galaxies which show a single power law have comparatively low HI-surface densities within their optical disks. Galaxies with uncorelated $\Sigma_{\rm gas}$-$\Sigma_{\rm SFR}$ distributions (e.g. NGC 3184) by contrast do not have many lines of sight with HI at low surface densities within their optical disks.

One possible explanation is that galaxies with well-defined total gas Schmidt laws (and low HI surface densities) may have lost diffuse HI unassociated with star formation in interactions. Many show signs of tidal disruption or ongoing interactions. This underlying reason for the range of distributions in the right hand part of Figure 4.4 is beyond the scope of this paper, the key observation here is that there *is* a range of distributions and that many galaxies are not described by a single power law relating $\Sigma_{\rm gas}$ to $\Sigma_{\rm SFR}$.

4.2.4 Star Formation Efficiencies

The SFE provides another way to express the results discussed above. Most galaxies show a fixed SFE relating their $\Sigma_{\rm SFR}$ and $\Sigma_{\rm H2}$. Some galaxies (e.g. NGC 5194) also show a constant SFE in their total gas spanning from high to low surface densities. The case of NGC 5194 is particularly striking; this galaxy displays a nearly constant SFE spanning surface densities from 0.1 $M_\odot$ pc^{-2} to 100 $M_\odot$ pc^{-2}. Over three orders of magnitude in gas surface density, the power law index remains near unity and $\Sigma_{\rm SFR}$ shows only a factor of ~ 2 scatter about a constant SFE.

On the other hand, several galaxies, e.g. NGC 628, NGC 3184 or NGC 3521, show steep distributions in the right hand column of Figure 4.4 and high power law indices. This may be phrased as large internal variations in their SFE. The variations in SFE are as striking in their own way as the correlation in NGC 5194: these galaxies span nearly an order of magnitude in SFE at an almost constant $\Sigma_{\rm gas} \sim 5$ $M_\odot$ pc^{-2}. This is clear evidence that the total gas surface density *cannot* be the critical quantity setting the SFR over the HI-dominated parts of these galaxies.

There is also variation in the SFE *among* galaxies. This can be seen from the range of coefficients to our power law fits. At a particular $\Sigma_{\rm gas}$, the average $\Sigma_{\rm SFR}$ shows an RMS scatter of ~ 0.3 dex. Galaxy-to-galaxy variations thus account for a factor of 2 scatter in the SFE in our sample.

4.2.5 HI Saturation at High Column Densities

Figure 4.4 and the radial profiles in Figure 4.2 also illuminate the relationship between $\Sigma_{\rm HI}$ and $\Sigma_{\rm H2}$. Both show a striking absence of high surface density HI; this is seen as a sharp right-hand edge to the distributions shown in the left-hand column of Figure 4.4 and the failure of *any* of our radial profiles (spirals or HI-dominated galaxies) to cross $\Sigma_{\rm HI} \approx 9$ $M_\odot$ pc^{-2}. The only gas in excess of this limiting surface density appears to be in the molecular phase. Wong & Blitz (2002) showed a similar 'saturation' effect in azimuthally averaged profiles for their molecule-rich spirals, as did Martin & Kennicutt (2001). The data plotted in Figure 4.4 show that this effect is present at 750 pc resolution and that it is remarkably universal. $\Sigma_{\rm SFR}$ and $\Sigma_{\rm H2}$ show no comparable limiting values.

The vertical dashed line in the left and the right columns of Figure 4.4 shows $\Sigma_{HI,\rm saturation} \approx 9$ $M_\odot$ pc^{-2}. In Section § 4.3.1 we will see that 95 % of the Σ_{HI} values for the combined distribution of all 8 spiral galaxies in our sample are below $\Sigma_{HI,\rm saturation}$.

A second effect is seen best in the radial profile points in the left column of Figure 4.4: at high SFRs there is often an *anti*-correlation between $\Sigma_{\rm HI}$ and $\Sigma_{\rm SFR}$. This occurs in the central HI-holes of spirals where the gas is overwhelmingly molecular and the star formation rate is very high. All 8 of our spiral galaxies show some degree of this effect, i.e. at least a mild central depression in HI.

4.2.6 Σ_{SFR} vs. Σ_{gas} in HI-dominated Galaxies

We have already seen that there are variations in the relationship between Σ_{gas} and Σ_{SFR} among spiral galaxies, mainly in the HI-dominated parts. Figure 4.5 shows the relationship between Σ_{SFR} and $\Sigma_{HI} \approx \Sigma_{gas}$ for 6 HI-dominated galaxies. Color contours for the two largest galaxies are coded as in Figure 4.4. For these two galaxies we plot points from the radial profiles (Figures 4.2 and 4.3) on the same plot as black crosses. Because the other 4 dwarf galaxies are small, we show scatter plots instead of density contours. Figure 4.5 shows individual plots for Ho II, IC 2574, NGC 2976 and NGC 4214. Note that the remaining galaxies, Ho I, DDO 154, DDO 53, M81 DwA and M81 DwB are so small that they yield only 1 – 10 sampling points each. We include these data only later in Figure 4.13, which shows aggregate data for all of our dwarf irregular galaxies.

Figure 4.5 shows that these galaxies display the same saturation value for Σ_{HI} as the large, centrally H_2-dominated spirals. This is somewhat surprising, as one would expect conditions in the ISM of many of these galaxies to be less favorable to the formation of H_2 from HI because of comparatively low metallicities (and thus lower dust content), shallow potential wells, lower gas densities, and more intense radiation fields. We might therefore have expected large reservoirs of HI to survive in these galaxies at columns where the ISM is mostly molecular in a spiral.

For the most part these galaxies show low SFEs and a steep distribution of Σ_{SFR} as a function of Σ_{HI}. This includes IC 2574, Holmberg II, and all of the 'small' irregulars not plotted. The notable exception is NGC 2976, which shows an SFE similar to that found in spiral galaxies and a clear relationship between Σ_{SFR} and Σ_{gas}. As with NGC 3627 and NGC 4736, this is driven largely by the presence of low gas surface densities in NGC 2976 that are not present over the optical disks of many of the other dwarf galaxies. NGC 2976 shows a steadily declining HI profile, perhaps curtailed by interactions with other members of the M81 group.

We know from mapping and single dish measurements that these galaxies are not H_2-dominated (for a Galactic conversion factor), so Σ_{HI} is likely to be a good proxy for the total gas over most lines of sight. However, if the CO-to-H_2 conversion factor were to vary dramatically, as has been suggested for dwarf irregular galaxies, or $\Sigma_{H2} > \Sigma_{HI}$ locally, then Σ_{HI} may severely underestimate Σ_{gas} toward the star forming peaks. The topic is too complex to address here, but we note the sense of the uncertainty: If $\Sigma_{gas} > \Sigma_{HI}$ then the points in Figure 4.5 will move to the right, to higher gas surface densities for the same Σ_{SFR}. Most dwarf irregulars already show lower SFEs than most spiral galaxies; the inclusion of a substantial reservoir of molecular gas would lower the SFE further, thus widening the difference.

4.2.7 Dependence on Resolution

We have so far considered the relationship between gas and star formation at 750 pc spatial resolution. Cloud formation, stellar feedback, and indeed a breakdown in our SFR tracers may all be strong functions of spatial scale. Therefore we investigate how the relationships between Σ_{SFR} and Σ_{gas} or Σ_{H2} changes with spatial scale. To do this, we convolve all of our data to a variety of spatial resolutions (see §4.1.2)

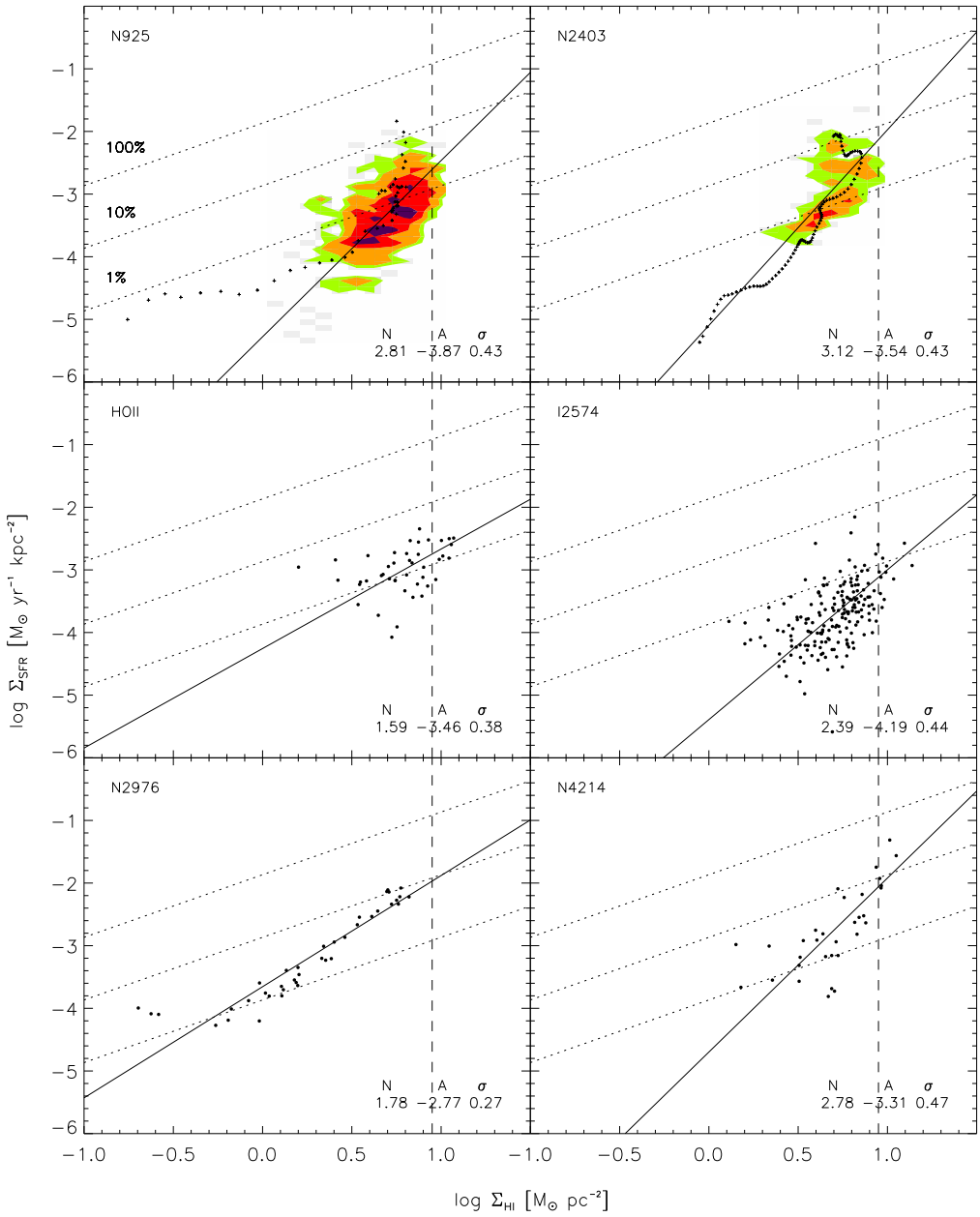

Figure 4.5: Contour and scatter plots respectively of $\Sigma_{\rm SFR}$ versus $\Sigma_{\rm HI}$ for 2 HI-dominated spirals and 4 dwarf irregular galaxies at 750 pc resolution. Contour levels and color coding are identical to Figure 4.4. For NGC 925 and NGC 2403, crosses show average measurements over tilted rings from the radial profiles. Diagonal lines show constant gas depletion times (or star formation efficiencies) taking helium into account, from top to bottom: 10^8, 10^9, and 10^{10} yr. The dashed vertical line shows the $\Sigma_{\rm HI}$ saturation level that was found for spiral galaxies.

spanning from the original (highest) resolution to 10 kpc and repeat the analysis above.

Figure 4.6 shows the distribution of $\Sigma_{\rm gas}$ versus $\Sigma_{\rm SFR}$ for a range of spatial resolutions in two spiral galaxies, NGC 5194 (M51) and NGC 6946. We show the $\Sigma_{\rm SFR}$ versus $\Sigma_{\rm gas}$ for 4 spatial resolutions, the original (best) spatial resolution, and then 500 pc, 750 pc and 1 kpc. Contours and other details are identical to Figure 4.4. Aside from the expected decrease in the number of independent sampling points and some narrowing of the distribution as a result of averaging, we do not observe any strong effects of the resolution in Figure 4.6.

To look more quantitatively at the effects of resolution on our results, we fit power laws to the data at each resolution. A single power law is an inadequate description of the data for many galaxies, but the fit here serves as a shorthand to characterize the data distribution. Figure 4.7 shows the results of power law fits as a function of resolution for 7 of our 8 spiral galaxies with associated CO emission (star formation in NGC 4736 is too concentrated for this exercise). The fits become more uncertain as the number of sampling points dwindle and averaging substantially lowers our dynamic range for many galaxies. Therefore we can carry out this test between the best available resolution and a spatial resolution of 1 kpc. The left panels in Figure 4.7 show the power-law indices, N, as a function of resolution; the right panels show the power-law coefficients, A. For the upper panels, we fit all CO data above the respective sensitivity limit (see § 3.1). For the bottom panels, we fit all total gas data within 0.4 r_{25}.

Figure 4.7 shows that the derived fits change slowly as the spatial resolution decreases from 200–500 pc to $\sim$ 1 kpc. If stellar feedback and cloud formation exert a strong influence on the relation between star formation and neutral gas (and indeed one would expect them to) then they do so on scales $\lesssim$ 300 pc. This finding agrees with results from Tamburro et al. (2008), who measured the offset between HI and star forming peaks near spiral density waves in some of the same data sets we study. They found a typical offset $\sim$ 100 pc or less between peaks in the star formation and HI maps.

4.3 Combined Distributions

In the previous section we saw that the relationship between $\Sigma_{\rm gas}$ and $\Sigma_{\rm SFR}$ varied among spiral galaxies and between spirals and HI-dominated galaxies. We saw that the value at which the atomic gas saturates appears constant across our entire sample and we found a well-defined power law index relating $\Sigma_{\rm H2}$ and $\Sigma_{\rm SFR}$. In this section we collapse the individual scatter plots in Figure 4.4 into a single pixel–by–pixel plot using our whole sample to draw general conclusions about the star formation law in our galaxy sample.

Figure 4.8 shows the distribution of $\Sigma_{\rm SFR}$ vs. $\Sigma_{\rm HI}$ (top left), $\Sigma_{\rm H2}$ (top right), and $\Sigma_{\rm gas}$ (middle right) for all sampling points in 7 spirals[1].

[1]We omit NGC 3627 from Figure 4.8 because including this galaxy makes it difficult to highlight trends in the other 7 galaxies.

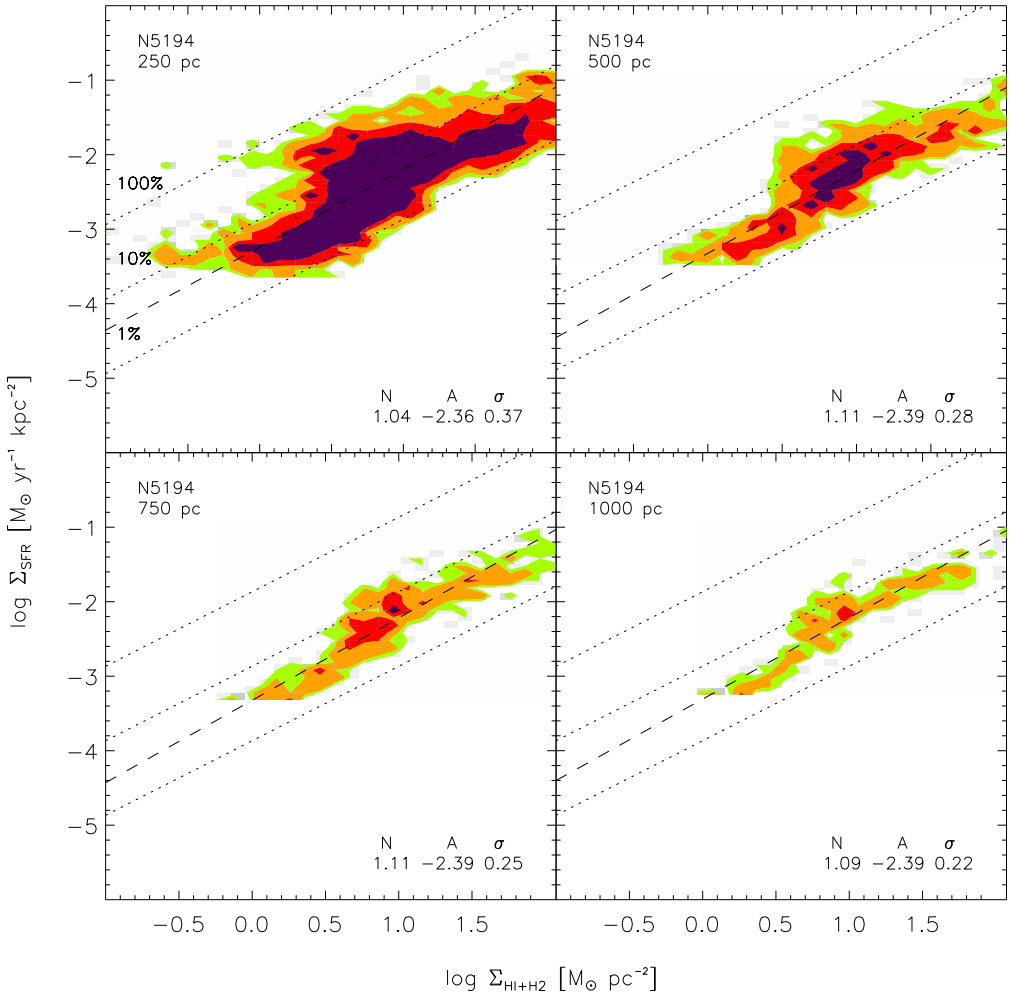

Figure 4.6: Log-log density plot of $\Sigma_{\rm SFR}$ versus $\Sigma_{\rm gas}$ for NGC 5194 (M51) and NGC 6946 at 4 different spatial resolutions: the individual maximum resolution, and then 500, 700 and 1000 pc. Contour levels and other features of the plots are identical to those in Figure 4.4. Although the number of independent data points dwindle, we do not see the distribution change markedly with resolution.

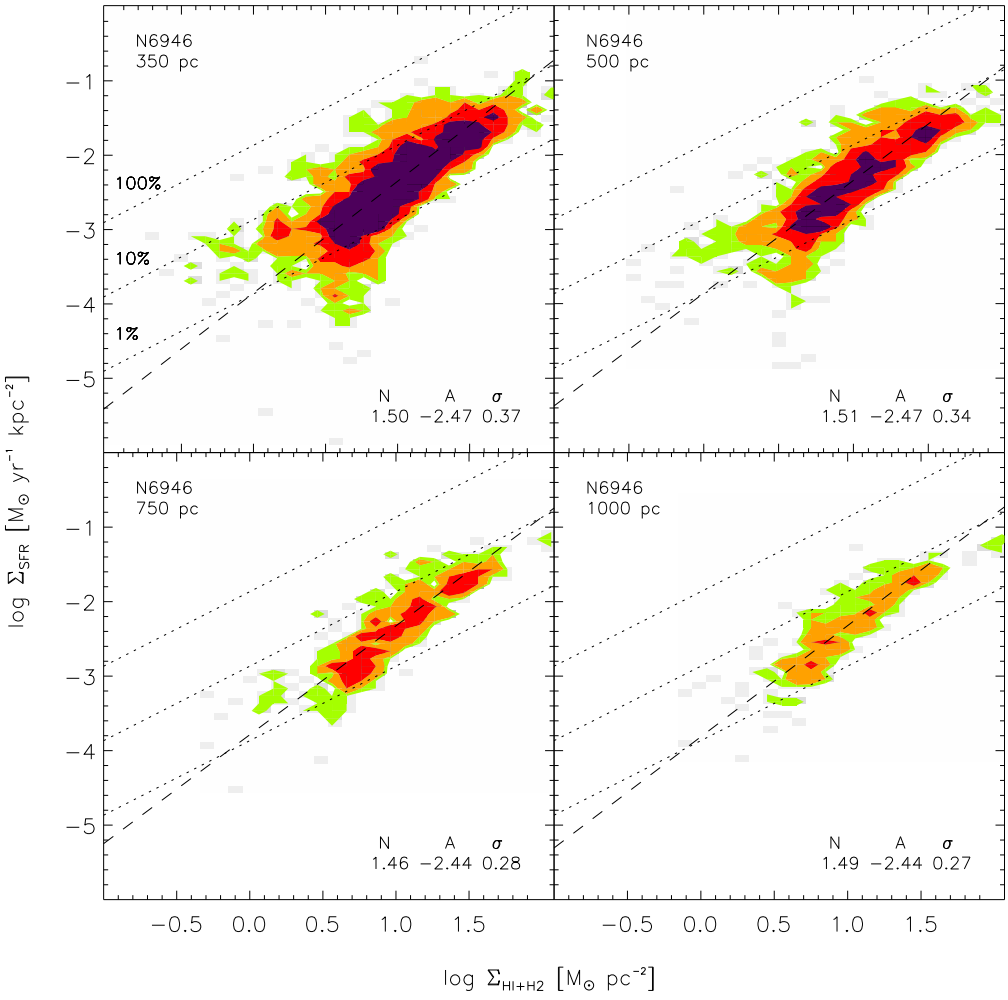

Figure 4.6: continued.

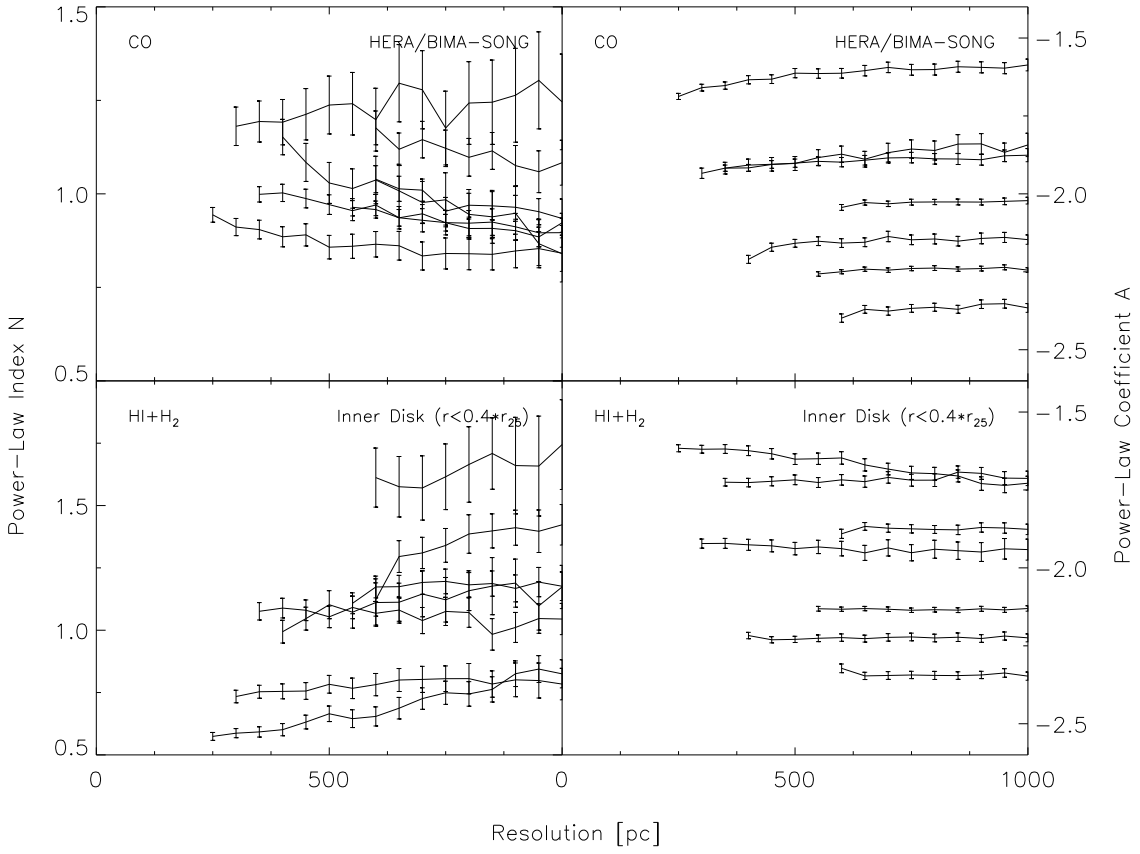

Figure 4.7: Power-law fit parameters, power law index N and coefficient A, for 7 of our 8 spiral galaxies (NGC 4736 is omitted). Left panels: N vs. spatial resolution. Right panels: A vs spatial resolution. The top panels show fits to HERA/BIMA-SONG CO data, the bottom panels to the total gas within $0.4\,r_{25}$. Both parameters vary only weakly with changing spatial resolution.

We also assess the impact of our choice of star formation tracer. The bottom two panels in Figure 4.8 show the relationship between $\Sigma_{\rm SFR}$ and $\Sigma_{\rm gas}$ using Hα (bottom left) or a combination of Hα and 24 μm emission following Calzetti et al. (2007) but applied pixel-by-pixel (bottom right). These plots include data for 6 spiral galaxies: NGC 628, NGC 3184, NGC 3521, NGC 5055, NGC 5194, and NGC 6946. All plot parameters are identical to those in Figure 4.4. The assumed IMF matches that in our SFR maps and the Hα-only plot includes a correction of 1.1 magnitudes of extinction for every point (a typical value over integrated galaxy disks, Kennicutt, 1998b). The dashed horizontal line in both panels indicates the estimated sensitivity limit in our Hα maps. For ease of comparison, the orange contour from the middle right plot is overplotted as the black contour on both bottom plots.

In summary, the bottom two distributions in Figure 4.8, which are based on different SF tracers, agree very well with the middle right distribution (black contour) that represents the SF tracer used throughout this paper. That is, our choice of star formation tracer does not appear to affect the derived relationship between $\Sigma_{\rm gas}$ and $\Sigma_{\rm SFR}$.

4.3.1 HI Saturation in the Combined Distribution

The top left panel of Figure 4.8 shows $\Sigma_{\rm SFR}$ vs. $\Sigma_{\rm HI}$. This plot clearly demonstrates the saturation effect discussed for the individual galaxies (see § 4.2.3) and shows that it is a universal feature in our sample. The middle left plot shows normalized histograms of $\log \Sigma_{\rm HI}$ and $\log \Sigma_{\rm H2}$. The HI shows a clear truncation near the threshold. By contrast, $\log \Sigma_{\rm H2}$ shows no such cutoff. This indicates that the HI saturation corresponds to a phase transition from the atomic to molecular ISM. The HI saturation value we quote of $\Sigma_{HI,\rm saturation} \approx 9$ M$_\odot$ pc^{-2} represents the 95th percentile of the HI distribution. This value coincides with the HI saturation value derived from Wong & Blitz (2002) using radial profiles in a sample of 6 molecule-rich spiral galaxies and agrees with our own radial profiles.

4.3.2 HI, H_2, Total Gas, and the Star Formation Law

The top two panels in Figure 4.8 show that $\Sigma_{\rm HI}$ and $\Sigma_{\rm H2}$ relate very differently to $\Sigma_{\rm SFR}$. In the top left plot, a very narrow range $\Sigma_{\rm HI}$ corresponds to a very large range of $\Sigma_{\rm SFR}$ and/or SFE. Over less than one order of magnitude in $\Sigma_{\rm HI}$, $\Sigma_{\rm SFR}$ covers ~ 3 orders of magnitude and the SFE spans 2 orders of magnitude. $\Sigma_{\rm HI}$ *cannot* be used to predict either $\Sigma_{\rm SFR}$ or the SFE in spiral galaxies. By contrast, the top right panel shows that $\Sigma_{\rm H2}$ exhibits a clear, monotonic relationship with $\Sigma_{\rm SFR}$ with a slope of unity (see § 4.3.4) down to the sensitivity of our CO data.

It is clear from Figure 4.8 that a single power law *can* describe the relationship between $\Sigma_{\rm SFR}$ and $\Sigma_{\rm H2}$ while $\Sigma_{\rm SFR}$ and $\Sigma_{\rm gas}$ show a clear 'knee' at the transition from an HI- to an H_2-dominated ISM.

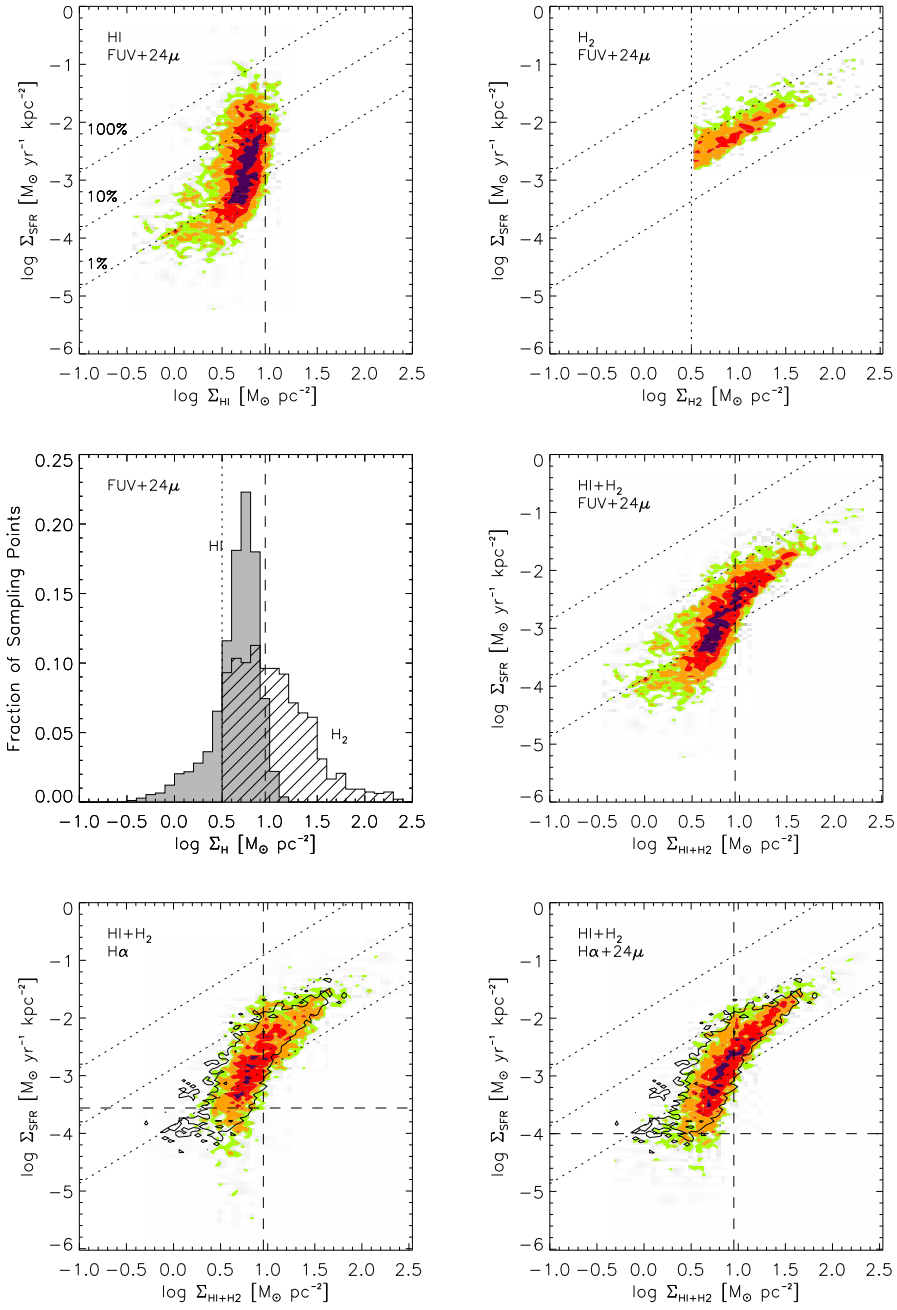

Figure 4.8: Results for all spiral galaxies plotted together. Top left: $\Sigma_{\rm SFR}$ vs. $\Sigma_{\rm HI}$; top right: $\Sigma_{\rm SFR}$ vs. $\Sigma_{\rm H2}$; middle right: $\Sigma_{\rm SFR}$ vs. $\Sigma_{\rm gas}$. We plot 7 of our 8 spirals with significant associated CO emission here (omitting NGC 3627). The lower left and right panels show $\Sigma_{\rm SFR}$ vs. $\Sigma_{\rm gas}$ using Hα and a combination of Hα and 24 μm emission as SF tracers for a subsample of 6 spirals. The black contour in the bottom panels corresponds to the orange contour in the middle right panel. All plot parameters are the same as in Figure 4.4. The middle left panel shows the normalized distribution of HI and H_2 surface densities in the sample.

4.3.3 Comparison With Measurements Integrated Over Galaxy Disks

We have shown that our pixel-by-pixel plots agree well with our radial profile results and are not affected by the choice of a particular SF tracer. Another key anchor to established results is shown in Figure 4.9, where we compare our combined data distribution to the integrated galaxy-disk measurements by K98. We show $\Sigma_{\rm SFR}$ vs. $\Sigma_{\rm gas}$ for all of our spirals as contours (identical to the middle right panel in Figure 4.8). We overplot the data points from Figure 6 of K98 after adjusting his $\Sigma_{\rm SFR}$ and $\Sigma_{\rm H2}$ to match our adopted IMF and CO-to-H_2 conversion factor. Figure 4.9 shows that our data distribution matches the K98 spirals well. This is discussed in more detail in § 4.5.

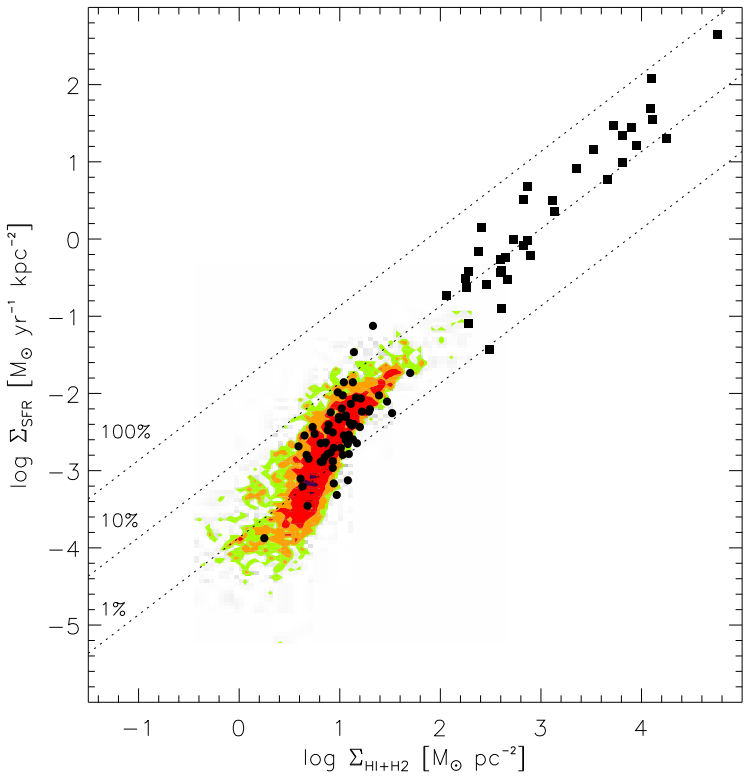

Figure 4.9: $\Sigma_{\rm SFR}$ versus $\Sigma_{\rm gas}$ in colored contours for spiral galaxies in our sample; these are the same data and contour levels as the middle right panel in Figure 4.8. We overplot data from K98. These are $\Sigma_{\rm SFR}$ and $\Sigma_{\rm gas}$ integrated across the optical disk for 61 normal spiral galaxies (filled circles) and 36 starburst galaxies (filled squares). We normalize his values to use our adopted IMF and CO-to-H_2 conversion factor. There is good agreement between our pixel-by-pixel data and disk-integrated measurements of normal galaxies.

4.3.4 The Combined Molecular Schmidt Law

We saw above that the common features in our data are the saturation of the HI and the linear relationship between $\Sigma_{\rm H2}$ and $\Sigma_{\rm SFR}$. Here we examine the 'molecular Schmidt law' for the data from all spiral galaxies combined. In the top left panel in Figure 4.10 we show the results of a power law fit to $\Sigma_{\rm SFR}$ vs. $\Sigma_{\rm H2}$ for CO data from HERA/BIMA-SONG in spiral galaxies (where $\Sigma_{\rm gas} \approx \Sigma_{\rm H2}$). Contour levels and other plot parameters are identical to the ones in Figure 4.4. The power-law fit is shown as a solid black line. The best fit parameters are $N = 1.01$ and $A = -2.12$; the RMS scatter of $\Sigma_{\rm SFR}$ about the fit is 0.20 dex, a factor of ≈ 1.6. In this regime, our data suggest a direct proportionality between $\Sigma_{\rm SFR}$ and $\Sigma_{\rm H2}$. The mean H_2 gas depletion time is $1.8 \cdot 10^9$ yrs with an RMS scatter of $0.7 \cdot 10^9$ yrs.

In the middle left panel the CO data comes from BIMA SONG alone. This allows us to plot the data at a slightly higher resolution of 500 pc and check the robustness of our results to changing CO maps and resolution. All other data and plot parameters are identical to the top left panel. We obtain an identical slope compared to that in the top left panel, $N = 1.01$ versus $N = 1.03$, with a similar coefficient and scatter.

The top and middle right panels show Monte Carlo realizations, where we compute $\Sigma_{\rm SFR}$ using $\Sigma_{\rm gas}$ from the data and the fit parameters quoted in the left panels including the measured lognormal scatter. The agreement between the left and right panels provides a qualitative check that a single power law is a good description of our data in this regime.

The bottom left and right panels show how the choice of star formation tracers affects the derived molecular Schmidt law. We use the HERA/BIMA-SONG maps (at 750 pc resolution) and replace our $\Sigma_{\rm SFR}$ maps with maps derived from Hα emission (bottom left plot) and a combination of Hα and 24 μm emission (bottom right plot, Calzetti et al., 2007). The Hα includes a 1.1 magnitude correction for internal extinction. For these data we fit $N = 1.11$ and $N = 1.18$ respectively. As in Figure 4.8, the choice of a specific SFR tracer has only marginal impact on our results.

We thus derive a best fit molecular Schmidt law of

$$\Sigma_{\rm SFR} = 10^{-2.1\pm0.2} \Sigma_{\rm H2}^{1.0\pm0.2}. \quad (4.2)$$

for the ensemble, identical to within the uncertainties to $N = 1.0 \pm 0.2$ and $A = -2.1 \pm 0.2$ found for individual galaxies (see S 4.2.1). The uncertainties of 0.2 take into account variations in SF tracers, substitution of CO maps and scatter in the data. They do not reflect variations in the CO-to-H_2 conversion factor, the IMF or systematics in our methodology.

4.4 The SF Law and Environment

We saw above that there are strong variations in the SFE within many spiral galaxies and between spirals and HI-dominated galaxies. In this section we attempt to link variations in the $\Sigma_{\rm SFR}$-$\Sigma_{\rm gas}$ relation outside the H_2 dominated regime to variations in

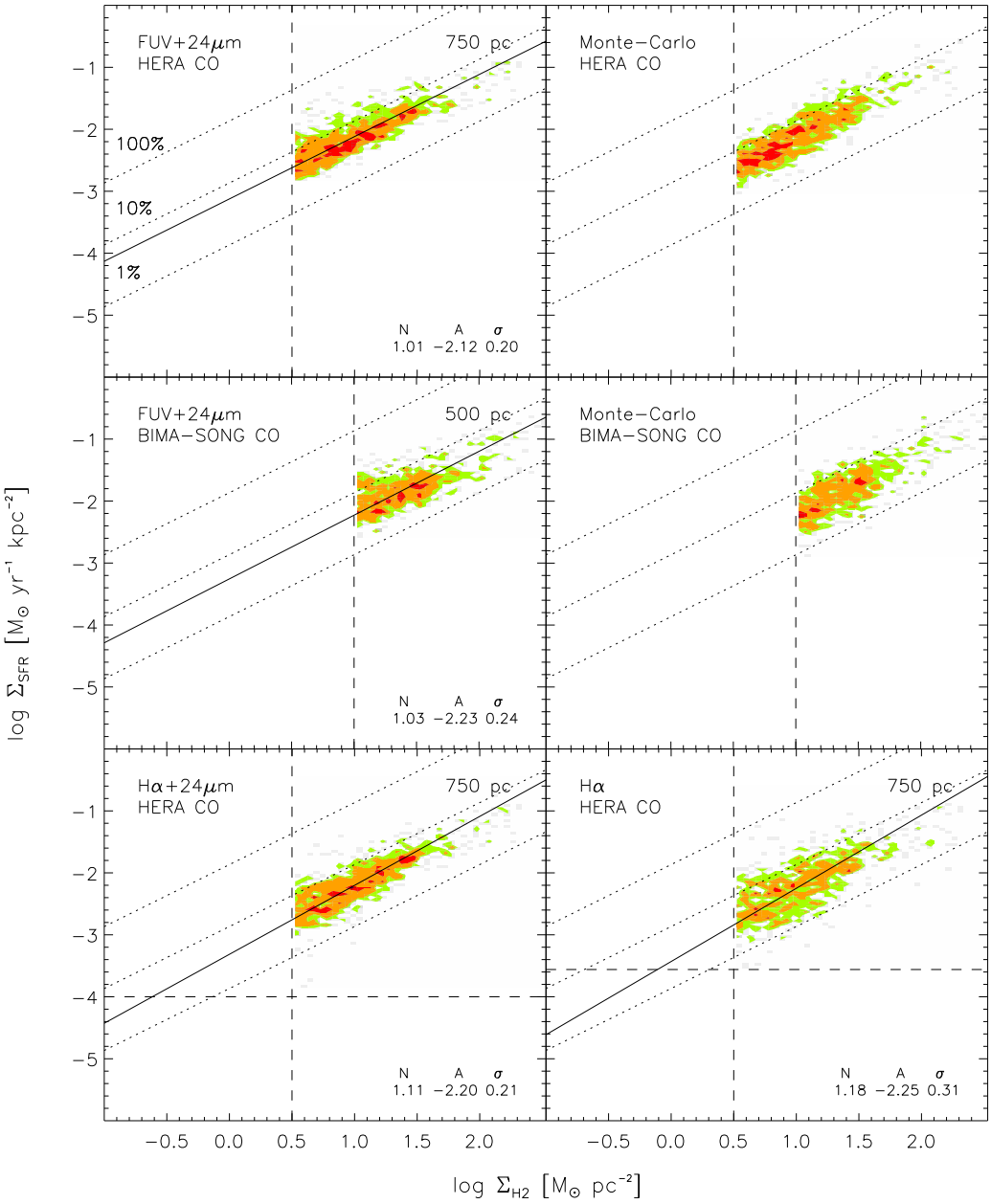

Figure 4.10: The molecular Schmidt law ($\Sigma_{\rm SFR}$ versus $\Sigma_{\rm H2}$) in spiral galaxies. Green, orange and red cells show contours of 1, 2 and 5 data points per cell. The black solid line shows the best fit power law, which has $N = 1.01$ and $A = -2.12$. The top and middle right-hand panels shows a Monte Carlo realization of the best fit power law using data values for $\Sigma_{\rm gas}$, observed scatter and best fit parameters.

environment. We approach this in two ways: by measuring how the star formation efficiency changes with radius within spiral galaxies and by comparing HI-dominated galaxies to spirals.

4.4.1 The Radial Dependence of the SFE

Our data show that below $\Sigma_{\rm gas} \sim 9$ M$_\odot$ pc^{-2}, the efficiency with which gas forms star varies dramatically at a given gas surface density. An obvious explanation is that star formation thresholds of the sort discussed by, e.g. Kennicutt (1989), Martin & Kennicutt (2001), Schaye (2004) or Leroy et al. (2008) are affecting the relationship between gas and star formation. We sample out to r_{25} and Martin & Kennicutt (2001) find that the last HII region often falls within or near this radius. The thresholds described by various authors stem from a variety of physics. Shear, Coriolis forces, pressure, metallicity, and passage through spiral arms may all play key roles in the formation of gravitationally bound molecular clouds, the necessary prerequisite to star formation.

An exhaustive investigation of all of these other quantities is beyond the scope of this paper Leroy et al. (but see discussion in 2008). However, most of the quantities that have been proposed as critical to star formation vary *radially*. Therefore, in Figure 4.11 we show a scatter plot $\Sigma_{\rm SFR}$ vs. $\Sigma_{\rm gas}$ with color showing the galactocentric radius of each sampling point. The plotted data are otherwise identical to the middle right plot in Figure 4.8 and the plot in Figure 4.9. The deprojected galactocentric radius of each point, normalized to the optical radius of the galaxy, determines the color of the point: points within $0.25\,r_{25}$ are black; sampling points between 0.25–0.5 r_{25} are red, those between 0.5–0.75 r_{25} are yellow; and sampling points from 0.75–1.0 r_{25} are green.

Figure 4.11 shows that in the centers of galaxies, where the gas is often molecular, the H_2 depletion time is nearly constant at $1.8 \cdot 10^9$ yrs. Outside this radius, where the ISM is dominated by HI, the SFE of gas at a particular surface density depends on the galactocentric radius of that point. The further out in the disk a point lies, the lower its SFE.

Figure 4.12 separates the data in Figures 4.8 – 4.11 into plots of $\Sigma_{\rm SFR}$ versus $\Sigma_{\rm gas}$ for specific ranges of galactocentric radius. We use the same radius bins as in Figure 4.11 and show a separate contour plot for each bin. Levels of 1, 2, 5 and 10 points per cell appear as green, yellow, red and magenta contours. The upper left panel shows the black sampling points ($< 0.25\ r_{25}$) from Figure 4.11, the upper right plot for the red points (0.25–0.5 r_{25}), the lower left for the yellow (0.5–0.75 r_{25}), and the lower right for the green sampling points (0.75–1.0 r_{25}). In the plots, we quote the mean SFE in that bin and its RMS scatter.

Figure 4.12 shows that where $\Sigma_{\rm HI} > \Sigma_{\rm H2}$, $\Sigma_{\rm SFR}$ is a function not only of $\Sigma_{\rm gas}$, but also of local conditions that vary strongly with galactocentric radius.

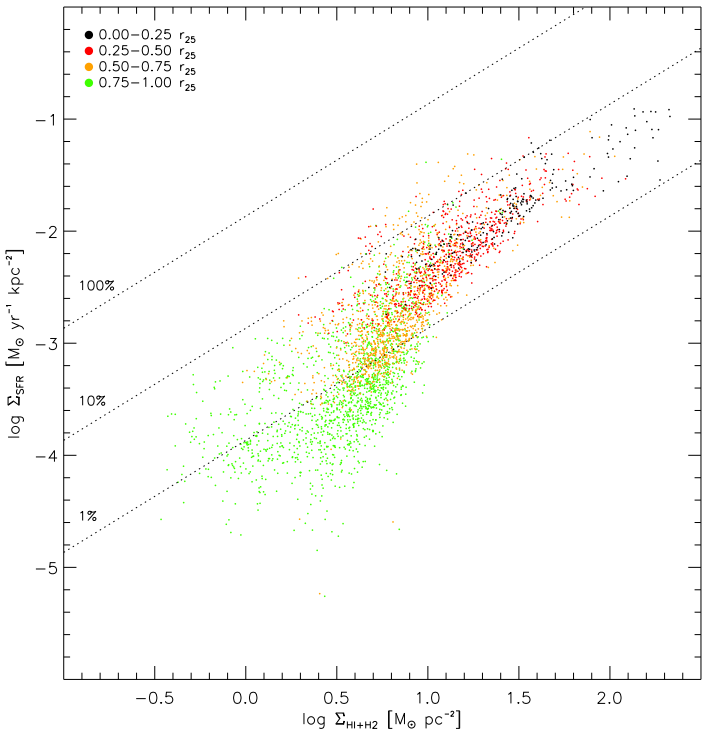

Figure 4.11: $\Sigma_{\rm SFR}$ versus $\Sigma_{\rm gas}$ for spiral galaxies with data colored by galactocentric radius. Every data point represents one sampling point; the data are the same as in Figures 4.8 and 4.9. We show the normalized galactocentric radius of every sampling point via its color. In units of r_{25} colors correspond to: black < 0.25; red 0.25–0.5; yellow 0.5–0.75; and green > 0.75. Other markings as Figure 4.4 – 4.9. The data clearly break up according to galactocentric radius, with low SFE/high depletion time points corresponding to the outer parts of galaxies.

4.4.2 HI-dominated Galaxies and the Outer Disks of Spirals

We saw in § 4.2.6 that the efficiency in HI-dominated galaxies is lower than that in spiral galaxies. In the previous section, we showed that the SFE varies dramatically within a spiral galaxy as a function of radius. Here we compare the two findings.

Figure 4.13 shows the combined distribution of $\Sigma_{\rm SFR}$ versus $\Sigma_{\rm HI}$ for all dwarf irregular galaxies in our sample (i.e. the HI-dominated galaxies from Table 4.1, omitting NGC 925 and NGC 2403 that would otherwise dominate the distribution). Green, yellow and red contours show 1, 2, and 5 points per cell. We show the same data for HI-dominated galaxies in all 4 panels. In each panel, we overplot a black contour that shows $\Sigma_{\rm SFR}$ versus $\Sigma_{\rm gas}$ for spiral galaxies in a particular radial bin. The black contour in Figure 4.13 corresponds to the lowest (green) contour in Figure 4.12 and the four panels show the contours from the same 4 radial bins as in Figure 4.12.

The distribution of $\Sigma_{\rm SFR}$ versus $\Sigma_{\rm gas}$ in dwarf galaxies overlaps to the distribution in the outer disk of spiral galaxies, shown in the bottom right panel of Figure 4.13. Many conditions are similar in the two regimes — low metallicities, low dust to gas ratios, high atomic gas fractions, and comparatively weak stellar potential

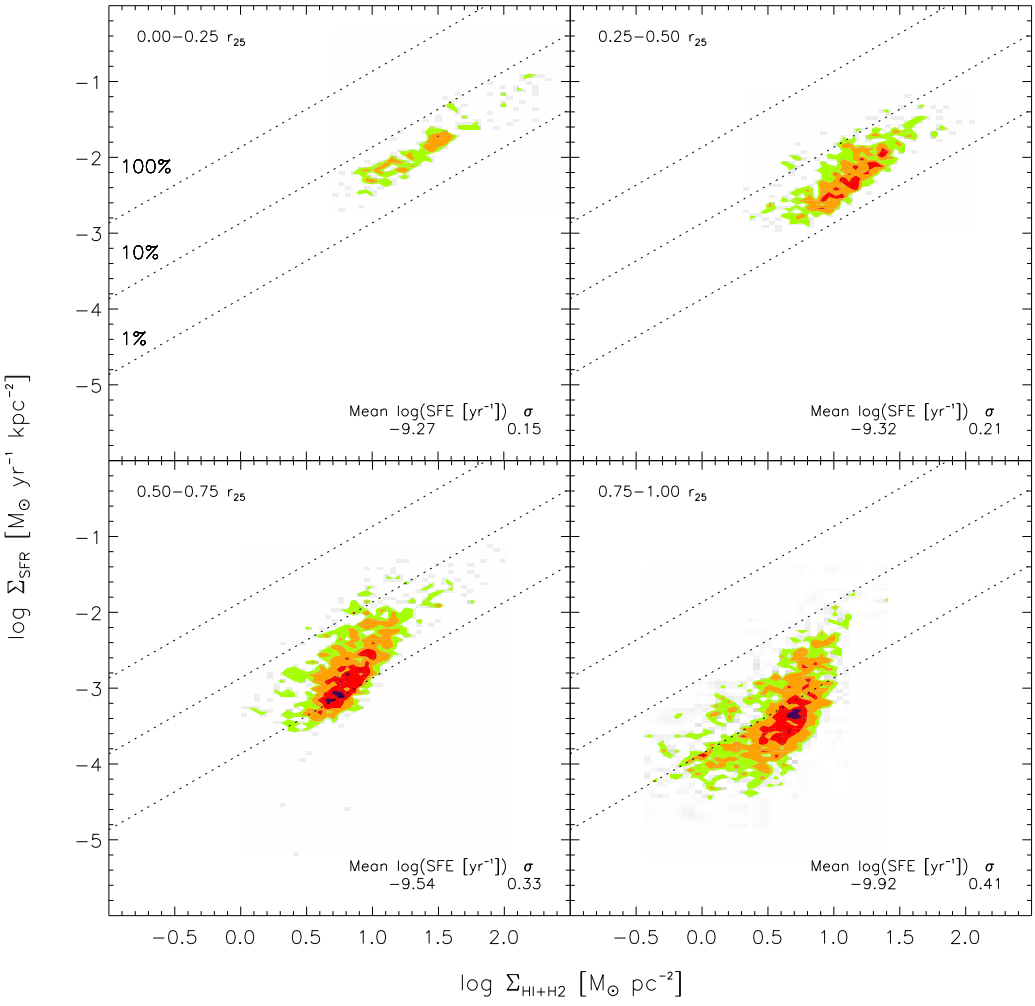

Figure 4.12: Variations of $\Sigma_{\rm SFR}$ versus $\Sigma_{\rm gas}$ with radius in spiral galaxies. Levels of 1, 2, 5 and 10 points per cell are shown as green, yellow, red and magenta contours. Every plot represents only sampling data from a certain range in normalized galactocentric radius, corresponding to a particular color of points in Figure 4.11: (upper left) $< 0.25\ r_{25}$, black points; (upper right) 0.25–0.5 r_{25}, red points; (lower left) 0.5–0.75 r_{25}, yellow points; (lower right) 0.75–1.0 r_{25}, green points. Data from outer galaxy disks display lower $\Sigma_{\rm SFR}$ for the same $\Sigma_{\rm gas}$ compared to points in the inner disks.

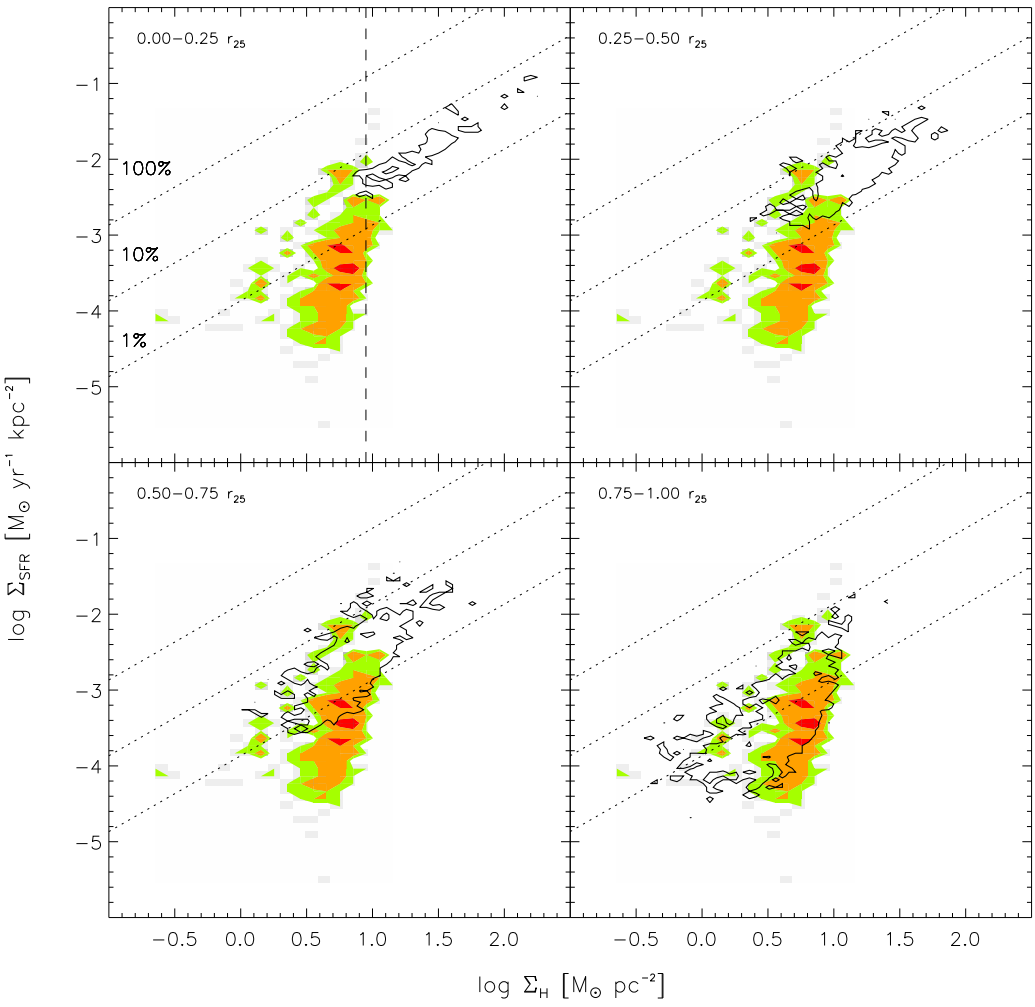

Figure 4.13: A comparison between dwarf irregular galaxies and the different regions of spiral galaxies. All four panels show $\Sigma_{\rm SFR}$ versus $\Sigma_{\rm HI}$ for dwarf irregular galaxies. Green, yellow, and red contours show 1, 2, and 5 points per cell. All four panels show the same distribution. Plotted over the dwarf distribution is the lowest contour from the corresponding panel in Figure 4.12. Thus each panel compares the distribution of data to that in spiral galaxies from a particular radial range. The best agreement is seen in the bottom right panel, in which the black contour shows data from 0.75–1.0 r_{25} in spiral galaxies.

wells. This plot suggests that these shared environmental factors lead to a similar relationship between gas and star formation in the two regimes.

We note that one environmental fact that dwarf irregulars do not share with the outer disks of spiral galaxies is differential rotation. Dwarf galaxies tend to have nearly solid body rotation curves and correspondingly low shear, whereas rotation curves tend to be flat in the outer parts of spirals. This implies that shear alone may not be the driving force regulating the SFE.

4.4.3 The Molecular-to-Atomic Gas Ratio Σ_{H2} /Σ_{HI} as a Function of Radius

In § 4.3.4 we saw that where $\Sigma_{HI} > \Sigma_{H2}$, the SFE varies strongly with radius and that $\Sigma_{SFR} \propto \Sigma_{H2}$. This leads us to expect that the H_2-to-HI ratio also varies strongly with radius (see e.g. Wong & Blitz, 2002). The right panel in Figure 4.14 shows Σ_{H2}/Σ_{HI} as a function of normalized galactocentric radius for all 8 spiral galaxies. The color cells show 2, 5 and 10 sampling points per cell in green, orange and red respectively (cell sizes: $\Delta x = 0.02\ r_{25}$, $\Delta y = 0.08$ dex). The filled black circles show the median Σ_{SFR} in radial bins of 0.1 r_{25}. The error bars indicate the 1σ scatter in the respective bin.

We find that the H_2-to-HI ratio decreases as function of radius. But the sensitivity

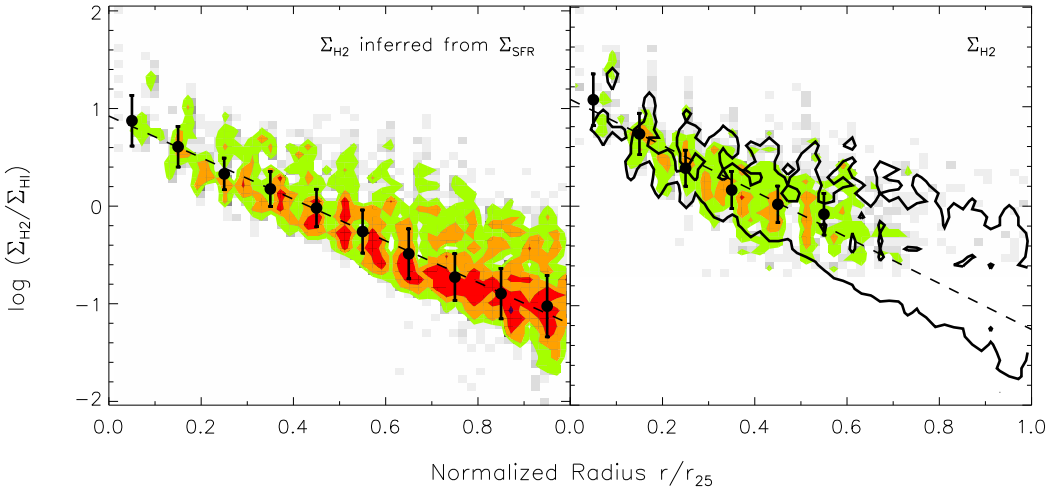

Figure 4.14: The ratio of molecular to atomic gas, Σ_{H2} / Σ_{HI}, as a function of galactocentric radius for spiral galaxies. In the left panel Σ_{H2} is inferred from Σ_{SFR} using the direct proportionality between the two that we have established in § 4.3.4. In the right panel Σ_{H2} from HERA is used directly. The black contour in the right panel is identical to the green contour in the left panel. Green, orange, red cells show contours of 2, 5 and 10 sampling points per cell. The filled black circles show the median Σ_{SFR} per 0.1 r_{25} radial bin, the error bars give the 1σ scatter in the bin. We carry out fits to both distributions. The solid black line shows a power law fit, the dashed black line shows an exponential fit.

of our CO data limit the measurement beyond $0.5r_{25}$. An alternate approach is to extrapolate Σ_{H2} from Σ_{SFR} using the direct proportionality between the two that we have established in § 4.3.4 for the inner part of the optical disk. The FUV and 24 μm data are more sensitive than our CO maps and so offer more measurements in the outer disk. For this approach, we assume that the relationship that we fit between Σ_{SFR} and Σ_{H2} holds across the disk of a galaxy. In this case, we infer the ratio of H_2-to-HI for each sampling point, $\Sigma_{H2}(\Sigma_{SFR})/\Sigma_{HI}$. This is shown in the left panel. The green contour in the left panel is overplotted in the right panel as a black contour.

The two approaches agree reasonably well; the ratio measured from CO overlaps the ratios inferred from Σ_{SFR}.

Both panels show that the phase of the ISM is a well-defined function of local conditions that vary with radius. A detailed investigation is beyond the scope of this paper but we explore this topic (often referred to as 'star formation thresholds') further in Leroy et al. (2008). Here we show that even an exponential fit, which is shown by the solid black line in both panels, can provide a good description of the relationship between H_2, HI and SF where $\Sigma_{HI} > \Sigma_{H2}$. The exponential fit yields a scale length of 0.2 in both panels. The coefficients on the fits give the radius where $\Sigma_{H2} = \Sigma_{HI}$. This is identical in both cases: 0.43 r_{25} in the left panel and 0.46 r_{25} in the right panel respectively.

4.5 Summary & Discussion

4.5.1 Results

Using data from THINGS, the IRAM 30m, BIMA SONG, the GALEX NGS and SINGS, we derive Σ_{HI}, Σ_{H2}, and Σ_{SFR} at 750 pc resolution across the optical disks of 8 nearby spiral galaxies with H_2-dominated centers and 11 HI-dominated late-type galaxies. We use these datasets to make the first pixel-by-pixel analysis of the star formation law in a significant sample of nearby galaxies.

We find two relationships common throughout our data. First, a molecular Schmidt law with index $N = 1.0 \pm 0.2$ relates Σ_{H2} to Σ_{SFR} in our sample of spirals. This may also be described as a total gas Schmidt law inside 0.4 r_{25}, where the ISM of all of our spiral galaxies are H_2 dominated. The average molecular gas (including helium) depletion time is $1.8 \cdot 10^9$ years with an RMS scatter of $0.7 \cdot 10^9$ years. This relationship holds for individual galaxies and the combined distribution and is robust to substituting BIMA SONG for HERA data, using different SFR tracers or changing resolution from $\sim$ 300 pc to $\sim$ 1 kpc.

The second common feature of our data is that Σ_{HI} saturates at a surface density of ≈ 9 $M_\odot$ pc^{-2}; gas in excess of this value is found in the molecular phase in the spirals. This saturation is common to spiral and HI-dominated galaxies. This is somewhat surprising because conditions in HI-dominated galaxies (such as dwarf galaxies) should be less favorable to the formation of H_2, which may lead one to expect a higher saturation value, a situation that is not observed.

We do *not* observe a universal relationship between *total* gas surface density and $\Sigma_{\rm SFR}$. Outside the H_2-dominated region, i.e. at $r \gtrsim 0.5r_{25}$, the relationship between gas and star formation varies both within and among galaxies. In some cases, a single power law relates total gas and SFR over many orders of magnitudes in gas surface density. In other cases, we find a wide range of star formation rates at almost the same gas column. As a result of this variation, our best-fit power law index, N, for the total gas in spiral galaxies ranges from 1.0 to 2.7. This agrees well with the range of indices found in the literature, but does not hint at a universal total gas Schmidt law.

We describe variations in the total gas-SFR relation in terms of the star formation efficiency (SFE), i.e. star formation rate per unit gas mass, and the H_2-to-HI ratio. We show that the SFE has a strong gradient with radius, where the highest efficiency points come from the inner disk, and the lowest efficiency points are at larger radii. We also show that the properties of late-type, HI-dominated galaxies overlap those of the outer disks of the spirals in our sample in $\Sigma_{\rm SFR}$-$\Sigma_{\rm gas}$ parameter space. This implies that the similar conditions, i.e. low metallicities, weak potential wells and low dust content, might drive the SFE.

We argue that these observations show a clear link between environment and the relationship between gas and star formation. We suggest the following scenario: The observational star formation 'law' as it is now understood (e.g. K98), is a molecular phenomenon. The transition from HI to H_2 and the subsequent formation of stars is not purely a function of the total gas surface density. Instead, other physics sets the ratio of HI to H_2. The critical quantity for these processes is a strong function of radius and appears to be common to both dwarf irregular galaxies and the outer regions of spiral disks. This agrees quantitatively with the findings of Wong & Blitz (2002) and qualitatively with the ideas of star formation thresholds discussed by e.g. Kennicutt (1989); Martin & Kennicutt (2001); Leroy et al. (2008) and many others.

We test the robustness of these results in several ways and find that our conclusions are robust against variations in the star formation tracer, spatial resolution or working with radial profiles or global averaging instead of pixel-by-pixel sampling.

4.5.2 The Molecular Schmidt Law In Various Regimes

We find $\Sigma_{\rm SFR} \propto \Sigma_{\rm H2}^{1.0\pm0.2}$, while e.g. K98 found a power law with slope $N = 1.40 \pm 0.15$ relating $\Sigma_{\rm SFR}$ and $\Sigma_{\rm gas}$. The fit of K98 depended on the contrast between normal spirals, $\Sigma_{\rm H2} \sim 20$ $M_\odot$ pc^{-2}, and high surface density starbursts, $\Sigma_{\rm H2} \sim 1000$ $M_\odot$ pc^{-2}. A power law index $N \approx 1.5$ relating SFR to CO emission has been well-established in starbursts by a number of authors (e.g. Gao & Solomon, 2004; Riechers et al., 2007). There may be reasons to expect different values of N in starburst environments and in our data. Starburst galaxies have average surface densities far in excess of a Galactic GMC (e.g. Gao & Solomon, 2004; Rosolowsky & Blitz, 2005). We have no such regions in our own sample, instead we make our measurements in the regime where $\Sigma_{\rm H2} = 3-50$ $M_\odot$ pc^{-2}. In starbursts, the changes in molecular surface density must reflect real changes in the physical conditions being observed.

In our data, $\Sigma_{\rm H2}$ is likely to be a measure of the filling factor of GMCs rather than real variations in surface density. For our resolution (750 pc) and sensitivity, $\Sigma_{\rm H2} = 3$ M$_\odot$ pc^{-2}, the minimum mass we can detect along a line of sight is $\sim 1.5 \cdot 10^6$ M$_\odot$. Most of the mass in Galactic GMCs is in clouds with $M_{H2} \approx 5 \cdot 10^5 - 10^6$ M$_\odot$ (e.g. Blitz, 1993). Consequently, wherever we detect H_2 we expect at least a few GMCs in our beam. On the other hand, most of our data have $\Sigma_{\rm H2} \lesssim 50$ M$_\odot$ pc^{-2}. The typical surface density of a Galactic GMC is 170M$_\odot$ pc^{-2} (Solomon et al., 1987). These surface densities are much lower than those observed in starbursts and are consistent with Galactic GMCs filling $\lesssim 1/3$ of the beam. If GMC properties are the same in all spirals in our sample, then for this range of surface densities we expect a power-law index of $N = 1$ as $\Sigma_{\rm H2}$ just represents the beam filling fraction of GMCs. Averaging over at least a few clouds may wash out cloud-cloud variations in the SFE. A test of this interpretation is to measure GMC properties in a wide sample of spirals. We note that Local Group spirals display similar scaling relations and cloud mass distribution functions so that it is hard to distinguish GMCs in M 31 or M 33 from those in the Milky Way (e.g. Blitz et al., 2007). If this holds for all spirals, then we may indeed expect $N = 1$ whenever GMCs represent the dominant mode of star formation. The next generation of mm-arrays should soon be able to measure GMC properties beyond the Local Group and shed light on this topic. In that sense, our measurement of $N = 1.0 \pm 0.2$ represents a prediction that GMC properties are more or less universal in nearby spiral galaxies.

For our results to be consistent with those from starbursts, the slope must steepen near $\Sigma_{\rm H2} \sim 200$ M$_\odot$ pc^{-2}. This might be expected on both observational and physical grounds. CO is optically thick at the surface of molecular clouds. Therefore, as the filling fraction of such clouds increases beyond ≈ 1, CO will become an increasingly poor measure of the true $\Sigma_{\rm H2}$. Even if such clouds have Galactic SFEs, the observed relationship between CO and an optically thin SF tracer, e.g far infrared (FIR), will steepen. It is also likely that physical conditions inside the molecular gas change as surface densities exceed that of a typical GMC. If the density increases, e.g., the free fall time within the gas will decrease, possibly leading to more efficient star formation (Krumholz & McKee, 2005). See Krumholz & Thompson (2007) for a full treatment of theoretical expectations for changing Schmidt laws.

Indeed, Gao & Solomon (2004) may observe the transition directly; in their Figure 3 they show that CO scales linearly with FIR emission, a SFR tracer, below $M_{H2} \approx 10^{10}$ M$_\odot$ and then with a steeper power law index above it. This value is about the upper limit of molecular gas masses observed in our sample of spiral galaxies (see Table 5 in Leroy et al., 2008). Based on our results, we suggest that the former regime corresponds to star formation organized into normal spiral GMCs.

If this sketch is correct, then care must be taken relating the SFR to CO measurements. The efficiency with which gas forms stars will depend on what regime one considers. Perhaps more excitingly, the reverse is also true: by measuring the SFE one can place a region or galaxy in either the 'starburst' or "GMC/disk" regime. This offers the intriguing prospect, for example, of diagnosing the dominant mode of star formation in surveys of star formation and molecular gas at high redshift that will be a major component of ALMA science. Even with the current generation of millimeter-wave telescopes such comparisons are possible. For example, Daddi et al.

(2008) recently showed that molecular gas in 'BzK'-selected galaxies at $z = 1.5$ has the same FIR-to-CO ratio (and thus presumably SFE) as local spiral galaxies. For comparison, sub-millimeter ('SCUBA') galaxies display dramatically higher SFEs, as traced by their FIR-to-CO ratios (e.g. Greve et al., 2005). A suggestive link to this work is that the BzK galaxies show signs of larger stellar disk and more extended CO emission; completely consistent with star formation proceeding mostly in a disk populated by GMCs analogous to those in nearby galaxies.

This chapter is submitted for publication.

Co-Investigators on this project are:
Adam Leroy (MPIA), Fabian Walter (MPIA), Elias Brinks (University of Hertfordshire), W.J.G. de Blok (University of Cape Town), B. Madore (OCIW), M. D. Thornley (Bucknell University)

Chapter 5

The Relation between Gas and Star Formation in Outer Galaxy Disks

The outer disks of galaxies are a distinctly different environment as compared to the optical disks or even the H_2 dominated centers of galaxies. In the outer disks, one finds less dust, implying lower metallicities, and a relatively rarified and totally HI dominated interstellar medium. In this chapter, the approach of studying the relation between gas and star formation at high resolution *spatially resolved* in the optical disks is extended into the outer disks of galaxies (out to $2\times r_{25}$). This allows to compare the results on the SFR-gas relations that were established in § 4 for the optical disks of galaxies to results of similar measurements in the outer disk environments.

A spatially resolved study of the SF law in these more extreme enviroments can only be adressed, because the GALEX data provide robust measurements of the faint emission from low-level star formation in outer galaxy disks and because THINGS detects HI emission out to the largest radii. Nevertheless, it is the sensitivity of the UV data that limits this study to galactocentric radii within $2\times r_{25}$. New GALEX observations, which are currently carried out, will yield new UV data on 8 nearby galaxies, which will be a factor of 3 more sensitive than current data. These new observations will allow to push further out into the extended UV and HI disks of galaxies and to study star formation in even more extreme environments (see § 7).

5.1 Data

The sample for this analysis consists of 26 galaxies: 19 spiral and 7 dwarf galaxies. This sample is constructed from the overlap of THINGS (Walter et al., 2008) and the GALEX NGS (Gil de Paz et al., 2007). We further require the HI and UV maps to have constant and good signal-to-noise (S/N) ratios within two optical radii r_{25}. Table 5.1 lists our sample along with their adopted properties: distance, inclination, position angle, optical radius r_{25} and morphology. We correct all maps for inclination using the inclination angles given in table 5.1. In order to put all

maps on the same angular resolution, we convolve all HI and UV maps to a common resolution of 15"(the best common resolution of all HI maps) by convolving with a circular Gaussian beam (on the sky) and take no account of the inclination of the galaxy. We place all maps on the THINGS astrometric grid (pixel scale: 1.5").

We use the THINGS maps to derive HI surface densities, Σ_{HI}, and we assume $\Sigma_{gas} \approx \Sigma_{HI}$ in the outer disks of galaxies, i.e. we neglect the contribution of molecular gas in such environments. We make this approximation because CO detections in such low metallicity environments are faint, and deep, extended observations covering large parts of the outer disks do not exist to date. The GALEX FUV maps are used to derive FUV intensities, I_{FUV}, and from these intensities we derive SFR surface densities, Σ_{SFR}. In this chapter, the relationship between Σ_{SFR} and Σ_{HI} in the outer disks of galaxies will be assessed. The regime in galactocentric radius that is studied in this chapter (1-2 r_{25}) is illustrated in Figure 5.1 using NGC 2403 as an example. The left panel shows the THINGS HI and the right panel the GALEX far UV map. The overplotted annuli indicate 1 and 2 r_{25} respectively.

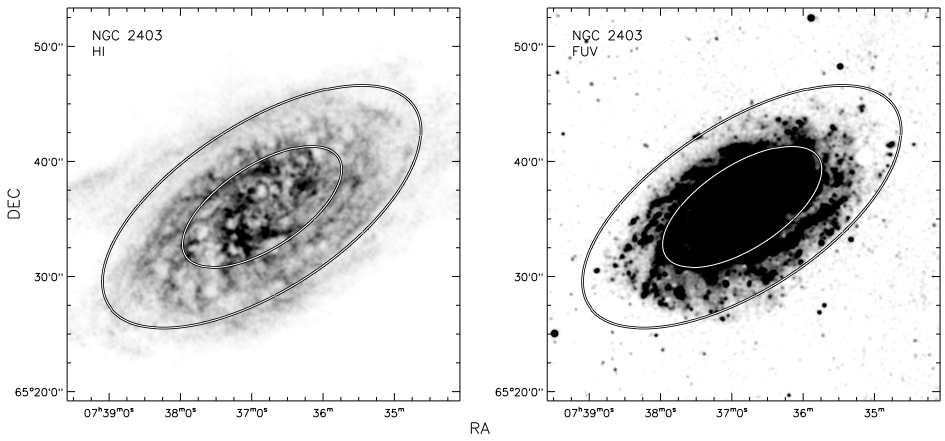

Figure 5.1: THINGS HI and GALEX far UV map for NGC 2403 in the left and right panel respectively. The two overlaid circles represent 1 and 2 optical radii r_{25}. How the HI and far UV emission from inbetween these annuli are related for all 26 galaxies in our sample is the topic of this chapter.

5.2 Deriving SFRs in the Outer Disks

For this analysis, we derive $\Sigma_{\rm SFR}$ from the GALEX FUV maps alone. Unlike in § 4 and Leroy et al. (2008), where we assessed the relation between gas and SF within the optical disks of nearby galaxies, we do not combine the FUV data from GALEX with *Spitzer* 24 μm data to correct for internal extinction. Because emission from warm dust is extremely faint in outer disks, the signal-to-noise (S/N) ratios for 24 μm emission are typically extremely low in these regimes and it thus becomes problematic to disentangle background sources from true outer disk emission. We illustrate below that a gas based estimate for the internal extinction in outer disks

Galaxy	D [Mpc]	i [deg]	PA [deg]	r_{25} [arcmin]	r_{25} [kpc]	Hubble type
			Dwarfs			
DDO 53	3.56	31	132	0.39	0.40	Irr
DDO 154	4.30	66.0	229.7	0.97	1.22	Irr
Ho I	3.84	12	50	1.66	1.85	Irr
Ho II	3.39	41	177	3.30	3.26	Irr
IC 2574	4.02	53.4	55.7	6.44	7.53	SABm
NGC 1569	1.95	63	112	1.99	1.13	Irr
NGC 2366	3.44	63.8	39.8	2.18	2.18	Irr
			Spirals			
NGC 0628	7.30	7	20	4.89	10.38	Sc
NGC 0925	9.16	66.0	286.6	5.36	14.28	Scd
NGC 2403	3.22	62.9	123.7	7.92	7.42	SABc
NGC 2841	14.10	73.7	152.6	3.46	14.19	Sb
NGC 2903	8.90	65.2	204.3	5.87	15.21	SABb
NGC 3184	11.10	16	179	3.71	11.97	SABc
NGC 3198	13.80	71.5	215.0	3.23	12.96	Sc
NGC 3351	10.05	41	192	3.62	10.59	Sb
NGC 3521	10.70	72.7	339.8	4.16	12.94	SABb
NGC 3621	6.64	64.7	345.4	4.89	9.44	SBcd
NGC 3627	9.25	61.8	173.0	5.12	13.77	SABb
NGC 4736	4.66	41.4	296.1	3.88	5.26	Sab
NGC 5055	10.10	59.0	101.8	5.87	17.26	Sbc
NGC 5194	8.00	20	172	3.88	9.03	Sbc
NGC 5236	4.47	24	225	7.74	10.07	Sc
NGC 5457	7.38	18	39	11.99	25.75	SABc
NGC 6946	5.90	32.6	242.7	5.74	9.85	SABc
NGC 7331	14.72	75.8	167.7	4.56	19.53	Sbc
NGC 7793	3.91	49.6	290.1	5.24	5.95	Scd

Table 5.1: Galaxy sample. See Walter et al. (2008) for further information on individual galaxies and for references to the values quoted in this table.

shows that an extinction correction is negligible for our purposes and thus, that the FUV alone, i.e. not corrected for internal extinction, provides a reliable tracer for $\Sigma_{\rm SFR}$ in outer disks.

To convert the FUV intensities into SFR surface densities, we adopt the conversion factor from Salim et al. (2007) (Equation 10 in their paper), which was calibrated for the GALEX FUV bandpass. For compatibility with previous work (see § 4, Leroy et al., 2008), we divide by a factor of 1.59 (Calzetti et al., 2007) to go to a Kroupa-type IMF (a two-component IMF that extends to 120 $\rm M_\odot$), the default IMF in STARBURST99 (Leitherer et al., 1999). The FUV-SFR calibration we apply thus becomes

$$\Sigma_{\rm SFR}\left[\rm M_\odot\ yr^{-1}\ kpc^{-2}\right] = 0.68 \times 10^{-28} I_{FUV}\left[\rm ergs\ s^{-1}\ Hz^{-1}\ kpc^{-2}\right]. \quad (5.1)$$

This calibration from Salim et al. (2007) was derived for ∼50,000 galaxies in the local universe by fitting population synthesis models to GALEX UV and SDSS optical multiband photometry. This emission will be dominated by the emission from the optical, i.e. starforming, disks of these galaxies. We assume that the same calibration is applicable to resolved outer disks, although they do not dominate the emission that was used by Salim et al. (2007) to calibrate equation 5.1.

To facilitate comparison between different plots in this work, we will only quote $\Sigma_{\rm SFR}$, and not $\rm I_{\mathit{FUV}}$, throughout this paper. *We stress that* $\Sigma_{\rm SFR}$ *is obtained from* I_{FUV} *through the simple linear transformation above (Equation 5.1), and is thus equivalent to the directly measured FUV intensity* I_{FUV}. Where we show data from inside the optical disks as well (see e.g. the radial profiles in § 5.3.2), $\Sigma_{\rm SFR}$ does not represent a true SFR surface density, because we do not correct for the effects of internal extinction (see § 5.2.1 below).

5.2.1 Gas Column based Extinction Estimate for the Outer Disks

In order to find out whether our FUV measurements in the outer disks of galaxies have to be corrected for internal extinction, we assess these effects in the following. An estimate based on UV color, following e.g. (Salim et al., 2007), is not feasible in our case due to the low S/N ratios of the UV emission in the outer disks. Because our HI based gas measurements are much more sensitive in these regimes, we estimate the extinction based on measured typical gas columns in outer disks.

Bohlin et al. (1978) relate the mean ratio of total neutral hydrogen to reddening via $\rm N(HI)/E(B-V) = 5.8 \times 10^{21}\,atoms\,cm^{-2}\,mag^{-1}$ in the Galaxy. We introduce a factor of 0.5 to account for the fact that most of the SF occurs approximately in the midplane of galaxies, and associated emission is thus only affected by approximately half the dust compared to what is inferred from the gas column along a line-of-sight. With $\rm A_{FUV}/E(B-V) = 8.24$ (Wyder et al., 2007), we get $\rm A_{FUV} = N(HI) \times 6.9 \times 10^{-22}$. Thus, the FUV intensity corrected for internal extinction can be calculated via

$$\rm I_{FUV,corr} = I_{FUV} \times 10^{N(HI)} \times 2.8 \times 10^{-22}. \quad (5.2)$$

For the outer disks of spirals, we use our radial profiles to derive mean HI columns for four radial bins from $1 - 2\,r_{25}$ in steps of $0.25\,r_{25}$. Using 5.2 and an average HI column in outer disks, $3\,M_{\odot}pc^{-2}$, we estimate factors to correct the FUV emission for internal extinction. For this HI column, the average correction factor is 1.27. This value decreases for larger radii, as the average gas densities become increasingly lower. This estimate assumes a galactic dust-to-gas ratio, which is almost certainly an overestimate in the outer disks, so that this correction factor is an upper limit. We therefore quote the factor of 1.27 as an upper limit to correct our FUV measurements from the outer disks for the effects of internal extinction.

5.3 Results

We observe that both, the average $\Sigma_{\rm gas}$ and $\Sigma_{\rm SFR}$, decline more or less smoothly in outer galaxy disks (see Figure 5.2). In the following we address the question of whether it is the diminished gas supply at large galactocentric radii that causes the drop in $\Sigma_{\rm SFR}$, or whether other physical mechanisms, like e.g. gas thresholds for SF, can be held responsible for this behavior. We use several approaches to assess the gas-SFR relationship at large galactocentric radii: Radial profiles out to $2 \times r_{25}$ and derived exponential scalelengths, $\Sigma_{\rm SFR}$ as a function of $\Sigma_{\rm gas}$, the dependence of the rank correlation between $\Sigma_{\rm SFR}$ and $\Sigma_{\rm gas}$ on galactocentric radius and pixel-by-pixel sampling of the outer disk, which we use to study the SF law at large radii and to compare to a previous pixel-by-pixel analysis of the optical disks of galaxies (see § 4).

5.3.1 Outer Disk Profiles

Figure 5.2 shows the HI and FUV radial profiles for all 26 target galaxies in our sample. These profiles represent azimuthal averages in tilted rings as a function of galactocentric radius. The tilted rings are constructed using inclination and position angles from table 5.1. Shown are the $\Sigma_{\rm gas}$ and $\Sigma_{\rm SFR}$ profiles in black and grey respectively out to 2 optical radii r_{25}. The error bars in the profile represent the 1σ scatter in each radial bin, which is half a beam width or 7.5" wide. In order to be able to compare the decline of both profiles in these plots qualitatively, the $\Sigma_{\rm SFR}$ profile is scaled to match the $\Sigma_{\rm gas}$ profile at the radius where the $\Sigma_{\rm gas}$ profile begins to decline (vertical black line). The fits from these reference points to $2\,r_{25}$ provide good approximations to the respective profiles (see S 5.3.2 for a description of the fitting procedure).

The 2 horizontal lines indicate the sensitivity limits, solid for $\Sigma_{\rm gas}$ and dotted for $\Sigma_{\rm SFR}$, down to which we carry out our exponential fits. These limits are $0.1\,M_{\odot}pc^{-2}$ for $\Sigma_{\rm gas}$, which is usually not reached in the regime we probe, i.e. within $2\times r_{25}$, and $1.8\times10^{-5}\,M_{\odot}yr^{-1}kpc^{-2}$, which is the 1σ sensitivity of the FUV maps (see § 5.2) converted to units of $M_{\odot}yr^{-1}kpc^{-2}$. Because the maps are convolved to 15"and emission is averaged within tilted rings to construct the radial profiles, one could push the fits towards lower $\Sigma_{\rm SFR}$ in most cases. We find that the conservative cutoffs

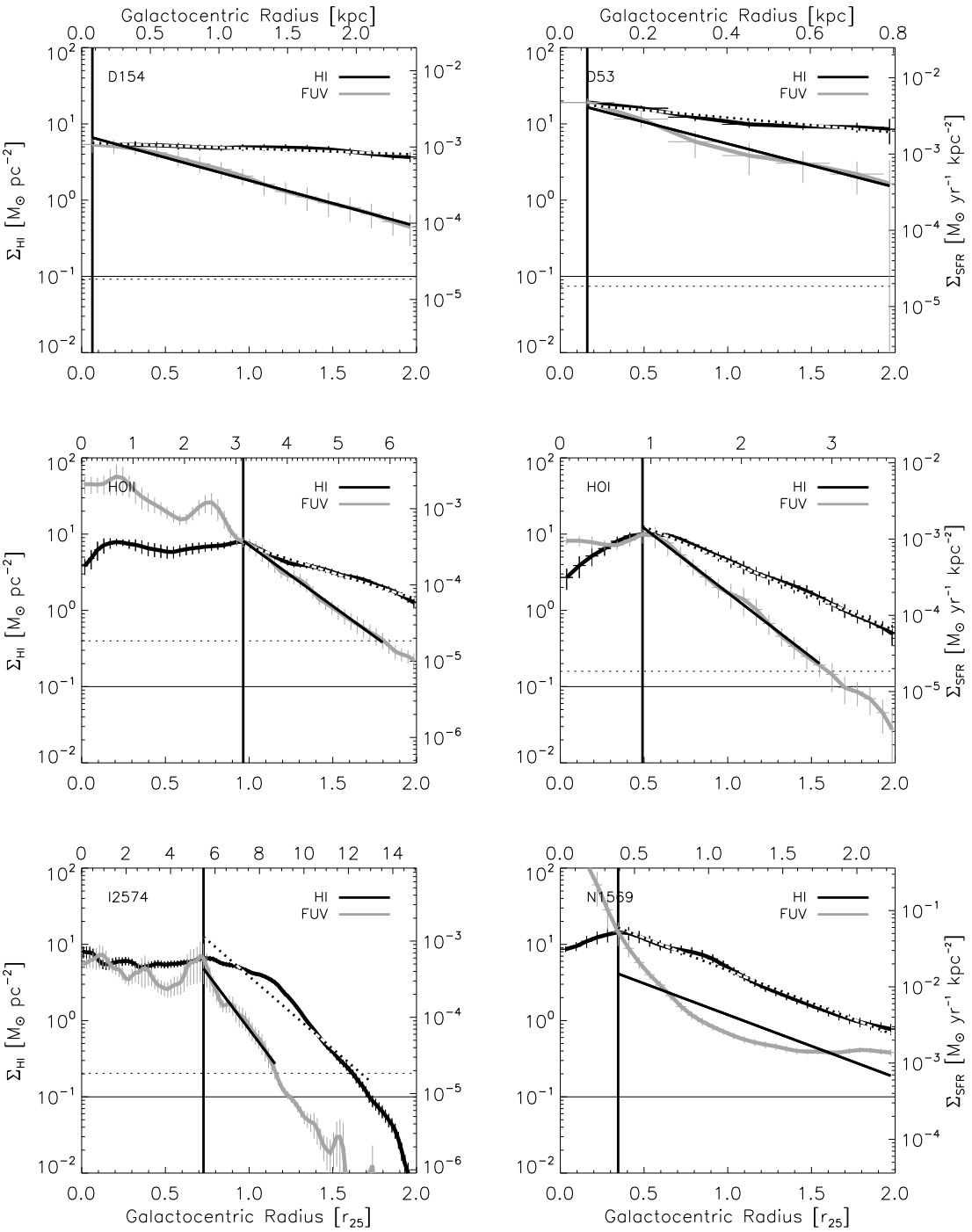

Figure 5.2: Shown are the $\Sigma_{\rm SFR}$ (grey) and $\Sigma_{\rm gas}$ (black) radial profiles for the galaxies in our sample. The vertical line indicates the radius at which the $\Sigma_{\rm gas}$ profiles begin to decline. We fit the decline of both, the $\Sigma_{\rm SFR}$ and $\Sigma_{\rm gas}$ profiles with exponentials. These fits are shown by the black solid and black and white dotted lines respectively. The horizontal lines represent the sensitivity cutoffs we use to constrain our fits (the dotted line for $\Sigma_{\rm SFR}$ and the solid line for $\Sigma_{\rm gas}$).

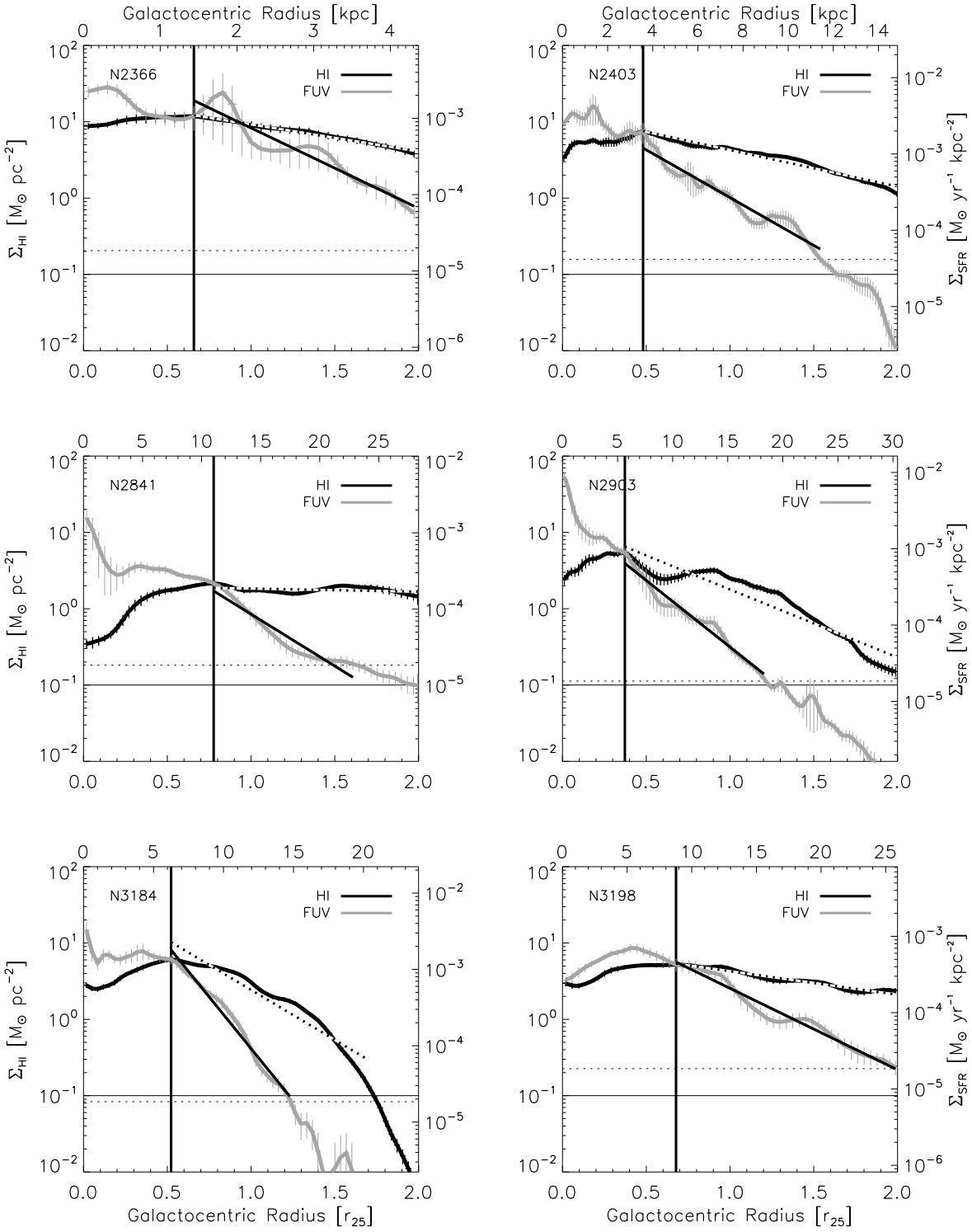

Figure 5.2: continued.

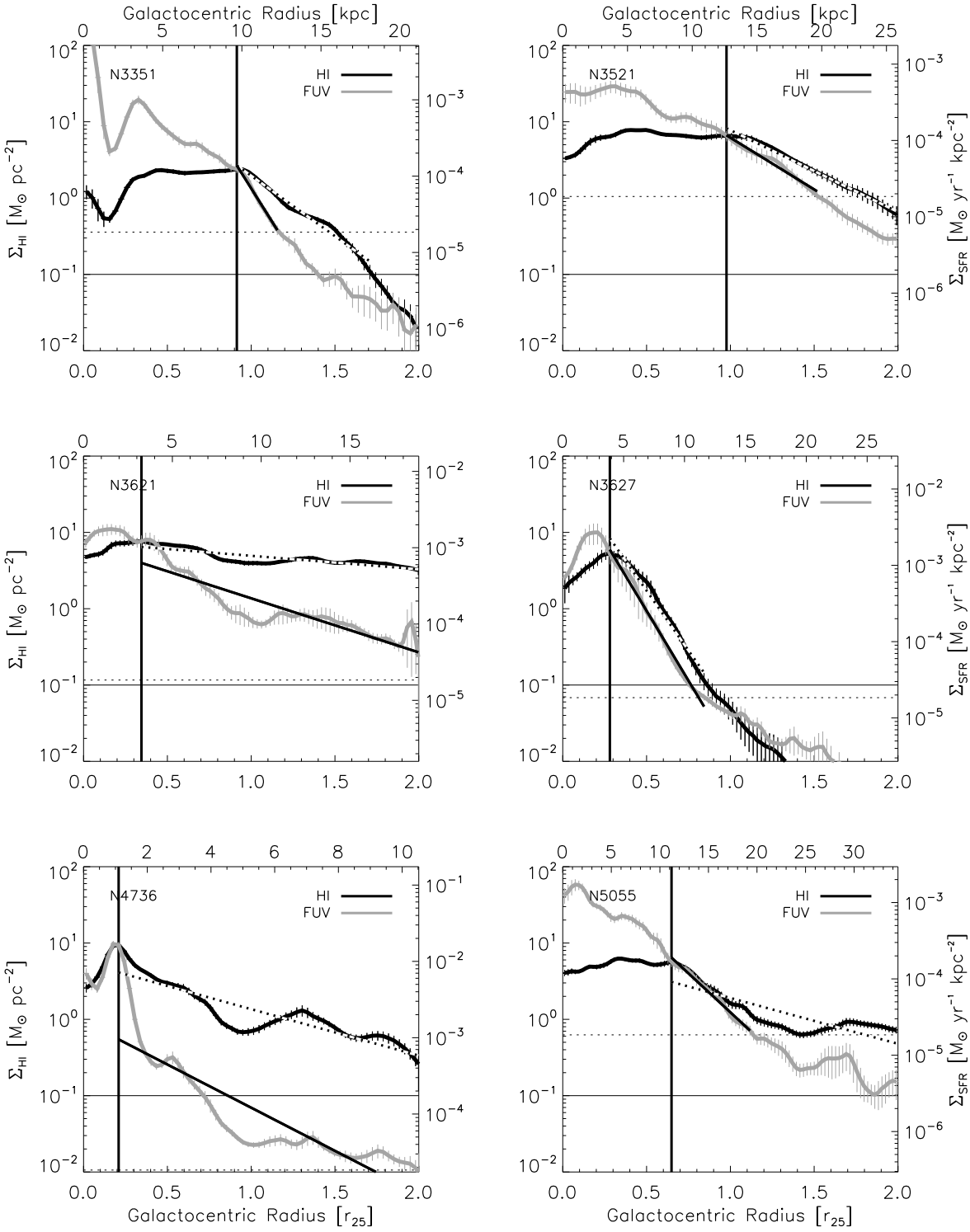

Figure 5.2: continued.

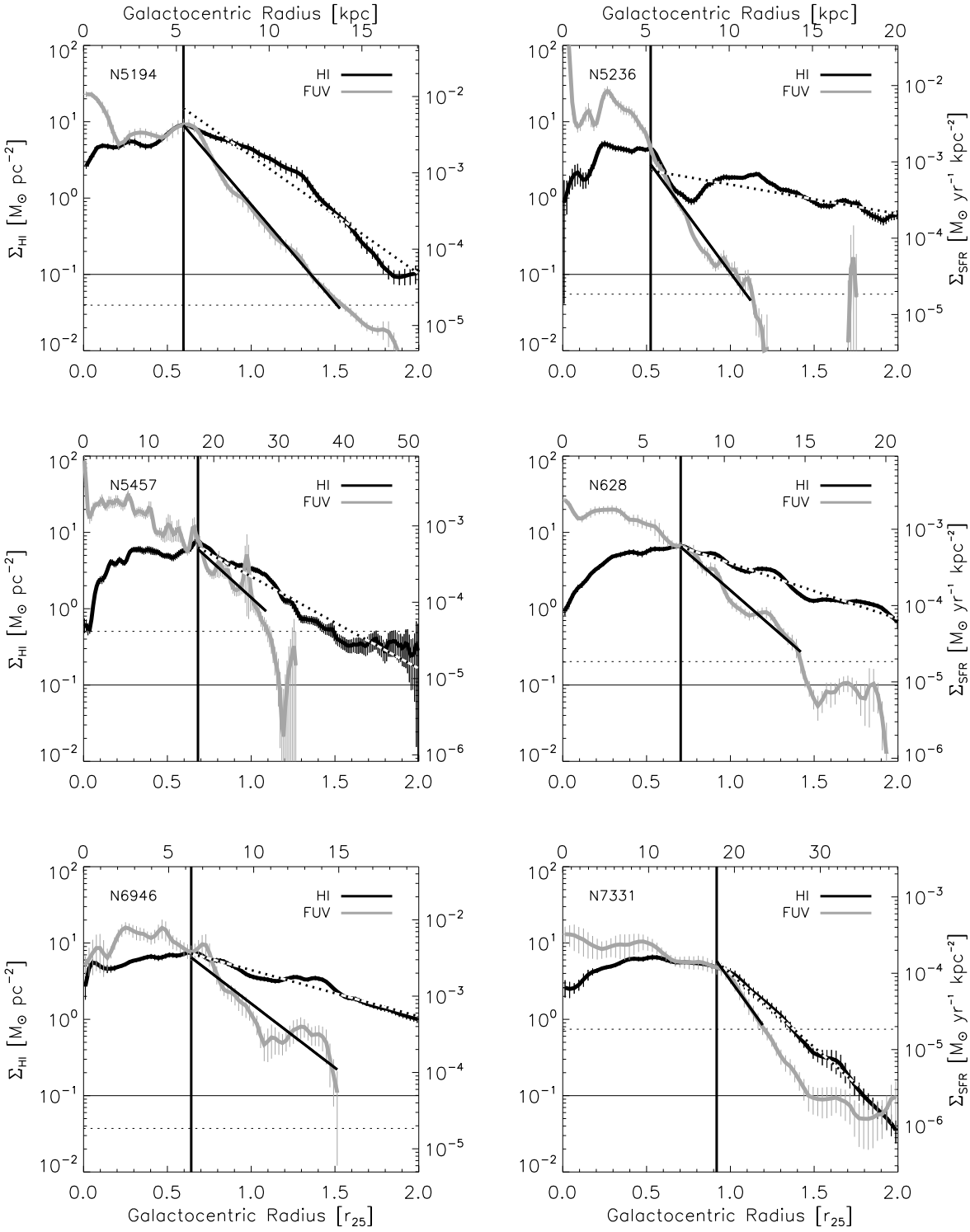

Figure 5.2: continued.

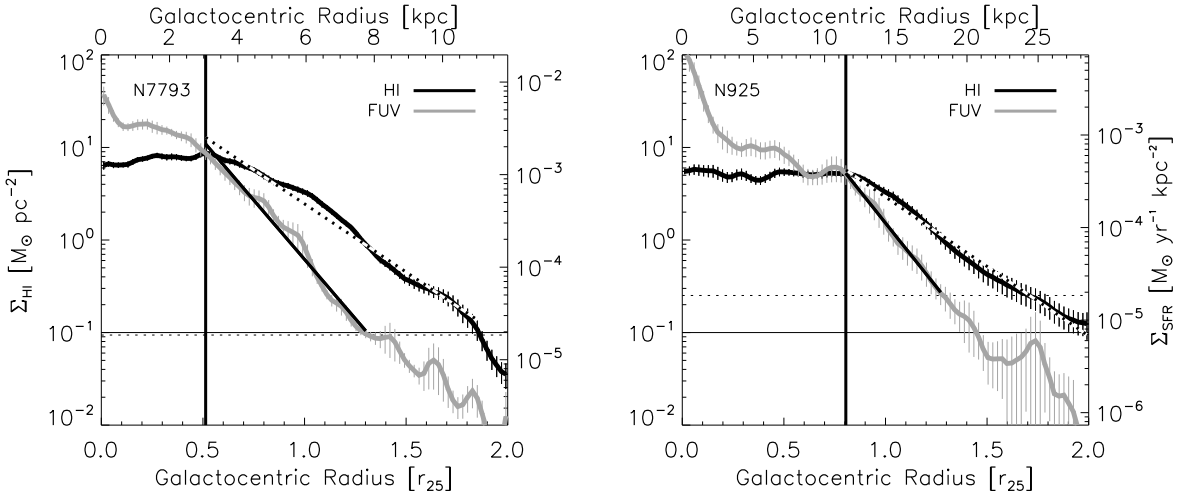

Figure 5.2: continued.

we apply are sufficient though to allow us to carry out well constrained fits in most cases.

5.3.2 Radial Profiles and Exponential Scalelengths

In order to quantify the radial decline of $\Sigma_{\rm SFR}$ and $\Sigma_{\rm gas}$, we fit exponentials to the outer parts of both profiles. 'Exponential Scalelengths' in this context are a useful way to parameterize the drop of the radial profiles.

The exponential fits themselves are shown as a straight solid black line for $\Sigma_{\rm SFR}$ and as a black and white dotted line for $\Sigma_{\rm gas}$ in Figure 5.2. We fit the radial profiles inbetween the reference point (the vertical solid black line) and $2\times r_{25}$ and only consider emission above the sensitivity cutoffs mentioned above. Because the exponential fit is carried out as a linear fit in $\Sigma_{\rm SFR}$-$\Sigma_{\rm gas}$ semi-log space, we estimate the stability of the fits by considering the variation of the fit parameters when applying ordinary least-squares (OLS) fits Y versus X, X versus Y and a bisector fit. The actual fit results, i.e. the exponential scalelengths, we quote are from the bisector fit. On top of the statistical errors on the scalelengths, we have estimated the systematic uncertainty to be $\sim$0.1 r_{25} by varying the radial range to fit over and the sensitivity cuts. In most cases, this systematic error dominates the total error. Table 5.2 provides the fit results: Given is the galactocentric radius outside of which we fit the exponentials to the profiles and the derived exponential scalelengths with errors.

The radial profiles show that for the vast majority of galaxies in our sample the UV profiles decline much more steeply than the HI profiles. This is shown more quantitatively in Figure 5.3. Plotted are the $\Sigma_{\rm SFR}$ exponential scalelengths versus the $\Sigma_{\rm gas}$ scalelengths for 22 galaxies from our sample. The scalelengths are derived from the exponential fits to the radial profiles (see above). Spirals are plotted in black and dwarfs in grey. The error bars represent the errors to the fit including

Galaxy	r_{fit} [arcmin]	r_{fit} [kpc]	Σ_{gas} Scalelength [r_{25}]	Σ_{gas} Scalelength [kpc]	Σ_{SFR} Scalelength [r_{25}]	Σ_{SFR} Scalelength [kpc]
Dwarfs						
DDO 53	0.06	0.06	2.22 ± 0.20	0.89 ± 0.08	0.76 ± 0.11	0.31 ± 0.04
DDO 154	0.06	0.08	5.56 ± 0.61	6.79 ± 0.74	0.72 ± 0.10	0.88 ± 0.13
Ho I	0.81	0.91	0.48 ± 0.10	0.88 ± 0.19	0.26 ± 0.10	0.47 ± 0.19
Ho II	3.19	3.14	0.63 ± 0.11	2.05 ± 0.34	0.27 ± 0.10	0.89 ± 0.33
IC 2574	4.69	5.48	0.23 ± 0.11	1.72 ± 0.80	0.15 ± 0.10	1.12 ± 0.77
NGC 1569	0.69	0.39	0.51 ± 0.10	0.57 ± 0.12	0.53 ± 0.17	0.60 ± 0.19
NGC 2366	1.44	1.44	1.23 ± 0.11	2.68 ± 0.23	0.41 ± 0.12	0.90 ± 0.26
Spirals						
NGC 628	3.44	7.30	0.60 ± 0.11	6.18 ± 1.18	0.23 ± 0.10	2.35 ± 1.09
NGC 925	4.31	11.49	0.29 ± 0.10	4.13 ± 1.45	0.16 ± 0.10	2.25 ± 1.43
NGC 2403	3.81	3.57	0.91 ± 0.12	6.74 ± 0.86	0.35 ± 0.11	2.57 ± 0.82
NGC 2841	2.69	11.02	10.54 ± 32.50	149.52 ± 461.04	0.32 ± 0.11	4.53 ± 1.59
NGC 2903	2.19	5.66	0.49 ± 0.13	7.42 ± 1.97	0.25 ± 0.10	3.78 ± 1.58
NGC 3184	1.94	6.26	0.33 ± 0.11	3.97 ± 1.37	0.16 ± 0.10	1.92 ± 1.21
NGC 3198	2.19	8.77	1.41 ± 0.13	18.28 ± 1.73	0.41 ± 0.11	5.27 ± 1.38
NGC 3351	3.31	9.68	0.27 ± 0.10	2.90 ± 1.09	0.12 ± 0.10	1.31 ± 1.06
NGC 3521	4.06	12.64	0.40 ± 0.10	5.24 ± 1.31	0.32 ± 0.10	4.15 ± 1.35
NGC 3621	1.69	3.26	2.45 ± 0.54	23.14 ± 5.13	0.61 ± 0.16	5.78 ± 1.55
NGC 3627	1.44	3.87	0.14 ± 0.10	1.91 ± 1.40	0.12 ± 0.10	1.63 ± 1.38
NGC 4736	0.81	1.10	0.71 ± 0.18	3.76 ± 0.94	0.38 ± 0.16	2.02 ± 0.83
NGC 5055	3.81	11.20	0.72 ± 0.24	12.48 ± 4.14	0.21 ± 0.10	3.67 ± 1.75
NGC 5194	2.31	5.38	0.28 ± 0.11	2.54 ± 0.96	0.17 ± 0.10	1.53 ± 0.91
NGC 5236	4.06	5.28	1.13 ± 0.39	11.37 ± 3.96	0.15 ± 0.10	1.46 ± 1.05
NGC 5457	8.19	17.58	0.36 ± 0.11	9.27 ± 2.90	0.22 ± 0.14	5.59 ± 3.56
NGC 6946	3.69	6.33	0.71 ± 0.12	7.04 ± 1.16	0.26 ± 0.12	2.54 ± 1.23
NGC 7331	4.19	17.93	0.23 ± 0.10	4.39 ± 1.97	0.14 ± 0.10	2.79 ± 1.98
NGC 7793	2.69	3.06	0.29 ± 0.10	1.75 ± 0.61	0.17 ± 0.10	1.01 ± 0.61

Table 5.2: Results from the exponential fits to the declining parts of the Σ_{gas} and Σ_{SFR} profiles. Presented are obtained scalelengths in units of the respective optical disk radius r_{25} and in kpc. r_{fit} denotes the radius outside of which exponentials are fit to the profiles. This specific radius is marked by the vertical black lines in Figure 5.2.

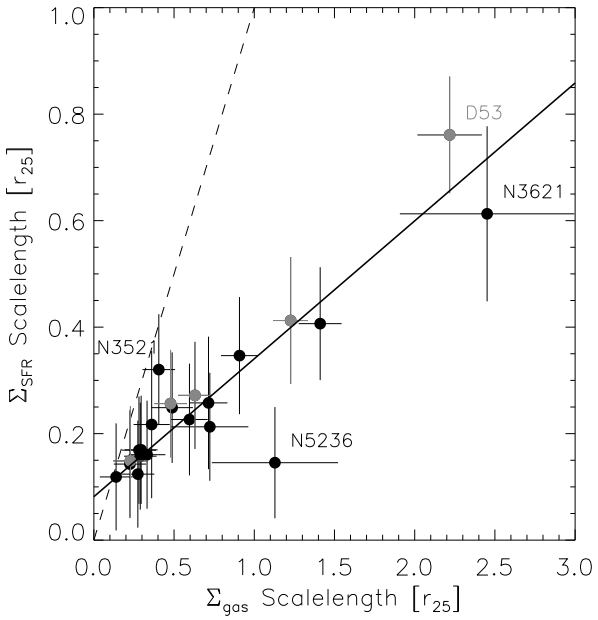

Figure 5.3: Plotted are the exponential scalelengths that are derived from fits to the declining outer parts of the $\Sigma_{\rm SFR}$ and $\Sigma_{\rm gas}$ radial profiles (the exact numbers are given in Table 5.2). The spirals are plotted in black, the dwarfs in grey. The solid line represents an OLS bisector fit to the data which yields a slope of 0.26±0.03, the dashed line indicates a slope of unity. One finds that all galaxies show larger scalelengths for $\Sigma_{\rm gas}$ than for $\Sigma_{\rm SFR}$.

systematics as described above. The dashed line represents a slope of unity. Four galaxies are excluded from Figure 5.3, because the radial profiles for these galaxies do not allow to derive reasonable scalelengths: For DDO 154 and NGC 2841 the $\Sigma_{\rm gas}$ profiles are flat within $2\,r_{25}$, and for NGC 1569 and NGC 4736 the $\Sigma_{\rm SFR}$ profiles do not resemble an exponential drop but rather a show more complicated behavior in the outer disk (see Figure 5.2).

One finds that the $\Sigma_{\rm gas}$ scalelengths are larger than the $\Sigma_{\rm SFR}$ scalelengths for every galaxy we plot. In fact, Figure 5.3 shows that the $\Sigma_{\rm SFR}$ scalelengths appear to scale with the $\Sigma_{\rm gas}$ scalelengths, as illustrated by an OLS bisector fit to the data (black solid line). Galaxies that appear as outliers are labelled with their respective name, and they all have relatively large errors (compare Table 5.2 and the radial profiles in the Appendix): DDO 53 has a relatively flat HI profile, leading to a not well constrained HI scalelength estimate; NGC 3621 has a relatively flat $\Sigma_{\rm gas}$ profile and a $\Sigma_{\rm SFR}$ profile that is not ideally fit by an exponential (leading to large error bars); NGC 3521 has a truncated HI disk and is one of only 2 galaxies in our sample where the $\Sigma_{\rm SFR}$ profile traces the $\Sigma_{\rm gas}$ profile in the outer disk (NGC 3627 is the other one), leading to similar scalelengths of the 2 profiles and placing the respective datapoint near the line of unity; NGC 5236 with its very extended UV emission and tidal HI features does not allow to derive well constrained fits to the profiles either. The first two galaxies, i.e. DDO 53 and NGC 3621, are compatible with our fit within their

errors however. NGC 3521 is slightly off, whereas NGC 5236 is the only galaxy that is relatively far off the fit.

We include these outliers in the OLS bisector fit to the data nevertheless and find a slope of 0.26±0.03. This implies that between 1 and 2×r_{25}, the scalelength for Σ_{gas} of a galaxy in our sample is on average four times larger than the respective scalelength for Σ_{SFR}. This indicates quite strongly that it is not the diminishing average gas surface density quenching SF at large radii. Instead, other physical mechanisms that vary with galactocentric radius, like e.g. the SFE or metallicity, must suppress SF in the outer disks. Interestingly, the dwarfs appear to follow the same trend as the spirals.

5.3.3 Rank Correlation

We have assessed the radial distributions of Σ_{SFR} and Σ_{gas} and how they relate to each other. Now we look at how well these distributions correlate spatially *at a given galactocentric radius*. The aim of this analysis is to find out whether the peaks of both, Σ_{SFR} and Σ_{gas}, coincide, and if and how the correlation varies as a function of galactocentric radius. We therefore compute Spearman rank correlation coefficients for Σ_{SFR} and Σ_{gas} in 10 equally wide radial bins between the center of each galaxy out to 2×r_{25}. In the process of computing rank correlation coefficients, the data, i.e. the Σ_{SFR} and Σ_{gas} pixels within a radial bin, are sorted by value. The rank correlation coefficient then describes how well both distributions match up and therefore also how well they correlate spatially. Perfect positive correlation between both sorted distributions corresponds to a coefficient of +1, a perfect negative correlation to a coefficient of -1, and if both distributions are independent, the coefficient is 0.

In our analysis, we treat spirals and dwarfs separately to look for differences or similarities between both samples regarding the radial distribution of rank correlation coefficients. Figure 5.4 shows these Spearman coefficients as a function of normalized galactocentric radius for the spiral galaxies. Each grey datapoint represents the derived coefficient for one galaxy in one radial bin. The horizontal error bars correspond to the width of the radial bins ($0.2\,r_{25}$). The vertical error bars represent the estimated error on the correlation coefficient. We estimate this error as follows: We assign a random order to the individual Σ_{SFR} and Σ_{gas} pixel values of one particular galaxy in one particular radial bin. This is done independently for Σ_{SFR} and Σ_{gas}. We then compute the correlation coefficient and repeat this procedure iteratively 100 times. The median based 1σ RMS scatter of this distribution of 100 rank correlation coefficients serves as our error estimate for each rank correlation measurement (i.e. for each grey datapoint). The black line represents the median values of all individual correlation coefficients (grey points) in each radial bin. The black error bars show the median-based 1σ RMS scatter of correlation coefficients in each bin.

The median correlation coefficients for the Σ_{SFR} and Σ_{gas} distributions range from 0.1 in the center to 0.7 at the edge of the optical disk and then drop again to 0.3 towards $2\,r_{25}$. In order to assess whether the moderate correlation coefficients in the very inner and outer radial regimes in Figure 5.4 are significant, we apply the same procedure that was used to estimate the errors for the correlation coefficients of the

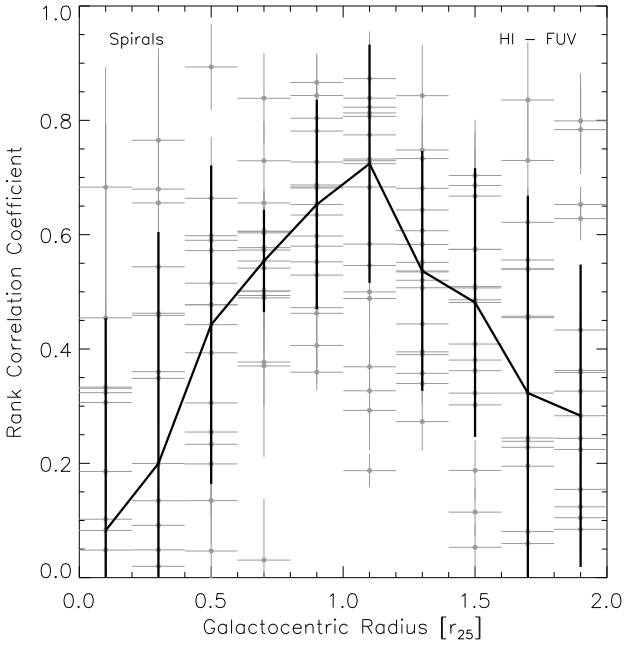

Figure 5.4: We show the Spearman rank correlation coefficients for the $\Sigma_{\rm SFR}$ and $\Sigma_{\rm gas}$ distributions in 10 radial bins (between the centers of the galaxies and $2\times r_{25}$) for the spiral galaxies in our sample. Each grey datapoint represent a correlation coefficient for one particular galaxy in one particular radial bin. The black line represents the median values of the correlation coefficients in each radial bin. The derived correlation coefficients indicate a significant correlation outside of $0.4\,r_{25}$. The coefficients vary with radius, however, peaking at the edge of the optical disk (r_{25}).

individual galaxies above: We use the $\Sigma_{\rm SFR}$ and $\Sigma_{\rm gas}$ pixel values from all galaxies in a particular radial bin and randomly and independently reorder both distributions. We then derive the rank correlation coefficient and repeat this procedure 100 times. The median value one obtains is 0 in each radial bin with a median based 1σ RMS scatter of 0.1 or less. This result shows that two randomly ordered samples (of the same size as the number of data pixels in each radial bin) in fact yield a rank correlation coefficient of 0, quite as expected. The low 1σ scatter of only 0.1 though implies that the median rank correlation coefficients we derive in the outer disks of 0.3 or more reflect a significant spatial correlation between $\Sigma_{\rm SFR}$ and $\Sigma_{\rm gas}$. Only within $0.4\,r_{25}$, where extinction is extremely high and molecular gas often dominates the ISM budget, are the distributions compatible with the hypothesis that they are independent, i.e not correlated. Elsewhere, even weak coefficients reflect a significant association between FUV and HI emission.

As mentioned above, the median rank correlation becomes stronger with increasing radius inside the optical disk, i.e. within r_{25}, and peaks at around r_{25}. The correlation then becomes weaker again at increasingly larger radii out to $2\,r_{25}$. As one goes from the edge of the optical disk at r_{25} to progressively *smaller* radii, the increasing presence of dust will lead to increasingly severe extinction (recall that

the FUV based $\Sigma_{\rm SFR}$ is not corrected for internal extinction). Furthermore, in the centers of many spirals the hydrogen gas is predominantly molecular, which leads to more or less extended HI depressions. Thus, the drop of the correlation coefficient towards smaller radii does most likely not reflect a true decrease in the strength of the correlation between $\Sigma_{\rm SFR}$ and $\Sigma_{\rm gas}$ across the optical disk, but rather is due to a combination of not considering molecular gas and the absence of a correction for internal extinction. Thus, an extinction correction and the inclusion of molecular gas (CO) data is absolutely necessary if one wants to study the relation between gas and SF in the optical disks of galaxies.

Both these issues, molecular gas and internal extinction, are negligible in the outer disks though (see § 5.1 and § 5.2.1). The decrease of the correlation coefficient from the peak at the edge of the optical disk towards larger galactocentric radii is therefore most likely real. To assess whether systematic spatial offsets at our working resolution of 15" between the peaks of $\Sigma_{\rm SFR}$ and $\Sigma_{\rm gas}$ are responsible for the weakening of the correlation at large radii, we produced maps convolved to 30" and repeated the analysis. We find almost identical results though (not shown). The declining correlation coefficient thus indicates that the beautiful correlation that is seen around r_{25} progressively breaks down as one moves further into the outer disk. We will see in § 5.3.5 that the reason for this is that, as one moves to larger radii, more and more lines of sight with significant HI have no associated significant FUV emission.

Figure 5.5 shows the equivalent plot to Figure 5.4 for the dwarf galaxies. This plot clearly suffers from the small number of only 7 dwarfs in our galaxy sample. This leads to enormous scatter about the median (black curve), which makes it hard to draw statistically significant conclusions. The median correlation coefficients between 0.25 and 0.65 out to $\sim$1.4 r_{25} indicate nevertheless a significant correlation of $\Sigma_{\rm SFR}$ and $\Sigma_{\rm gas}$ in the dwarfs. Adding more dwarfs to the sample will clearly help to improve the situation and to be able to make robust statements about the variation of the correlation coefficient with radius in dwarf galaxies.

5.3.4 $\Sigma_{\rm SFR}$–$\Sigma_{\rm gas}$ Scaling

The analysis of the rank correlation between $\Sigma_{\rm SFR}$ and $\Sigma_{\rm gas}$ above showed that both surface densities are significantly correlated in outer galaxy disks. In order to study the relation between these 2 quantities directly, we look at how $\Sigma_{\rm SFR}$ scales with $\Sigma_{\rm gas}$ in outer disks. For this analysis, we use all data between 1 and 2 r_{25} and bin $\Sigma_{\rm SFR}$ according to $\Sigma_{\rm gas}$ between 0 and 30 $M_\odot$ pc^{-2} in 10 equally wide bins (see Figure 5.6). Spirals and dwarfs are treated separately.

The histograms in the left panel of Figure 5.6 show the distribution of the number of pixels per $\Sigma_{\rm gas}$ bin for the spirals (grey) and the dwarfs (black). Not surprisingly, very low gas surface densities dominate in outer galaxy disks. The rather high $\Sigma_{\rm gas}$ values of up to 30 $M_\odot$ pc^{-2} in the histogram for the spirals come almost exclusively from the (very gas rich) outer disks of NGC 5457 (M 101) and NGC 6946. Other than that, both histograms show quite similar distributions for the dwarfs and the spirals.

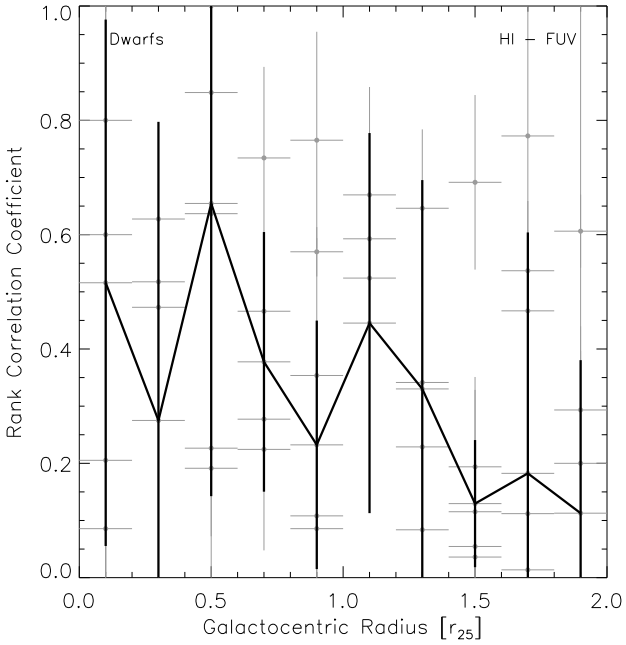

Figure 5.5: Shown are the Spearman rank correlation coefficients for the $\Sigma_{\rm SFR}$ and $\Sigma_{\rm gas}$ distributions as a function of radius for the 7 dwarf galaxies. This plot is otherwise identical to Figure 5.4. There is a significant correlation of $\Sigma_{\rm SFR}$ and $\Sigma_{\rm gas}$ out to $\sim$1.4 r_{25}, but statements about the radial behavior of the average correlation coefficient are hard to make due to the small number of dwarfs in our sample.

The right panel shows the SFE, i.e. $\Sigma_{\rm SFR}$ normalized to $\Sigma_{\rm gas}$, as a function of $\Sigma_{\rm gas}$. Studying the SFE, instead of $\Sigma_{\rm SFR}$, allows to look for intrinsic variations in $\Sigma_{\rm SFR}$, rather than simple scaling with $\Sigma_{\rm gas}$. The mean SFE in each $\Sigma_{\rm gas}$ bin is shown as a grey filled circle for the spirals and as a black triangle for the dwarfs. The error bars represent the 1σ RMS scatter in each bin. The number of pixels that contribute to each datapoint (modulo the oversampling factor of $\sim$100, which we derive from the ratio of beam area and pixel area) can be read off directly from the histograms in the left panel.

A simple but important result from this plot is that in the lowest $\Sigma_{\rm gas}$ bin, the SFE for the spirals become virtually zero. *Regions with low gas column densities in outer disks are extremely inefficient at forming stars.* This is true even when compared to higher gas columns in the outer disks. This is extremely suggestive of the kind of threshold behavior predicted by Schaye (2004).

To investigate how the SFE depends on gas column above the possible gas threshold, we carry out power-law fits to the SFE-$\Sigma_{\rm gas}$ distributions of the spirals and the dwarfs. We only fit where we measure significant SFEs and therefore exclude the lowest bin. The fits are overplotted as the grey solid (spirals) and the black solid line (dwarfs). For comparison, a linear relation, i.e. a power-law index of unity, is indicated by the dotted black line. The fits yield power law slopes of 1.09$\pm$0.04 for the spirals and 0.79$\pm$0.30 for the dwarfs. As can bee seen in the right panel of Figure 5.6, the fit for the dwarfs is much less constrained than for the spirals,

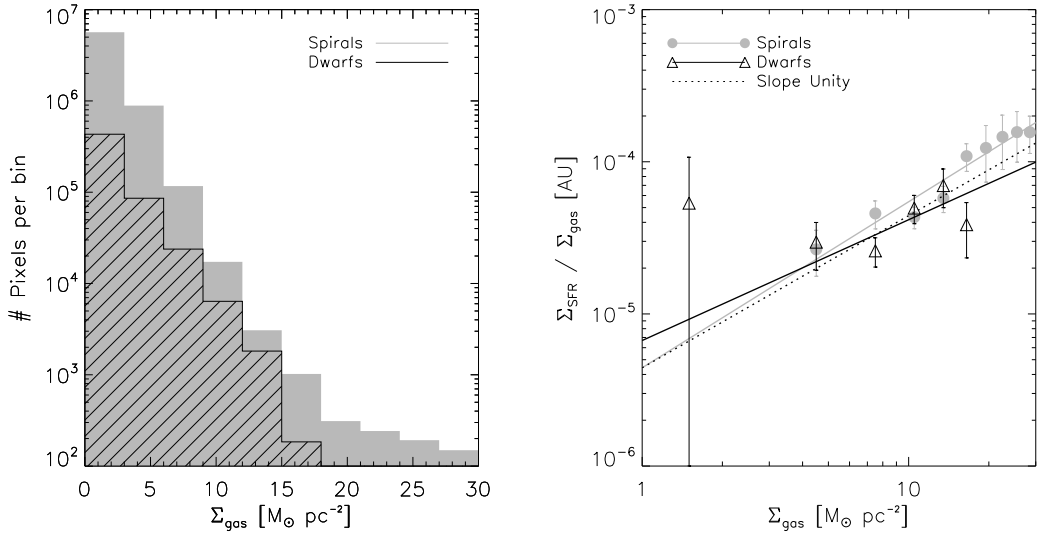

Figure 5.6: The histograms in the left panel show the distribution of the number of pixels per $3\,M_\odot$ pc^{-2} wide $\Sigma_{\rm gas}$ bin. The grey histogram represents the spirals, the black histogram the dwarfs respectively. The right panel shows the mean values of the normalized $\Sigma_{\rm SFR}$ per $\Sigma_{\rm gas}$ bin. The error bars represent the 1σ RMS scatter. Power law fits to the data are indicated by the grey (spirals) and black (dwarfs) lines. A slope of unity is indicated by the dotted line, which roughly resembles both of the fits within their errors.

because the individual data points in the plot show much more scatter about the fit for the dwarfs. Slopes of around unity indicate a roughly linear relationship between the SFE and $\Sigma_{\rm gas}$, i.e. SFR increases roughly as $\Sigma^2_{\rm gas}$. The slightly smaller slope for the dwarfs is not significantly deviant from the slope for the spirals, as both values overlap within their errors. The increase of the SFE with $\Sigma_{\rm gas}$ is is in good qualitative agreement with the behavior of $\Sigma_{\rm SFR}$ and $\Sigma_{\rm gas}$ in the radial profiles and the derived scalelengths (see § 5.3.2), where we find both quantities decreasing with radius. Because $\Sigma_{\rm SFR}$ was found to decrease faster with radius than $\Sigma_{\rm gas}$, the SFE should also decrease with radius, i.e. with decreasing $\Sigma_{\rm gas}$. We will come back to this when we derive similar slopes considering individual pixels and radial profiles in § 5.3.5.

In order to assess how the SFE varies not only with $\Sigma_{\rm gas}$ but also with radius, we repeat the above analysis (see Figure 5.6) for three distinctly different radial bins: 0.5 - 1 r_{25}, 1 - 1.5 r_{25} and 1.5 - 2 r_{25}. The histograms in Figure 5.7 show the distribution of number of pixels per $\Sigma_{\rm gas}$ bin for these 3 radial regimes (left panel for the spirals and right panel for the dwarfs): The thick black line histogram represents the inner, the black hashed histogram the intermediate, and the filled grey histogram the outer radial bin. The histograms show for both, spirals and dwarfs, that the $\Sigma_{\rm gas}$ distribution changes significantly depending on the radial regime. With increasing galactocentric radius, the fraction of pixels with low gas surface densities increases strongly at the expense of pixels with high gas surface densities. This is particularly prominent for the dwarfs, where in the outer radial bin (thick black line) $\sim$90% and

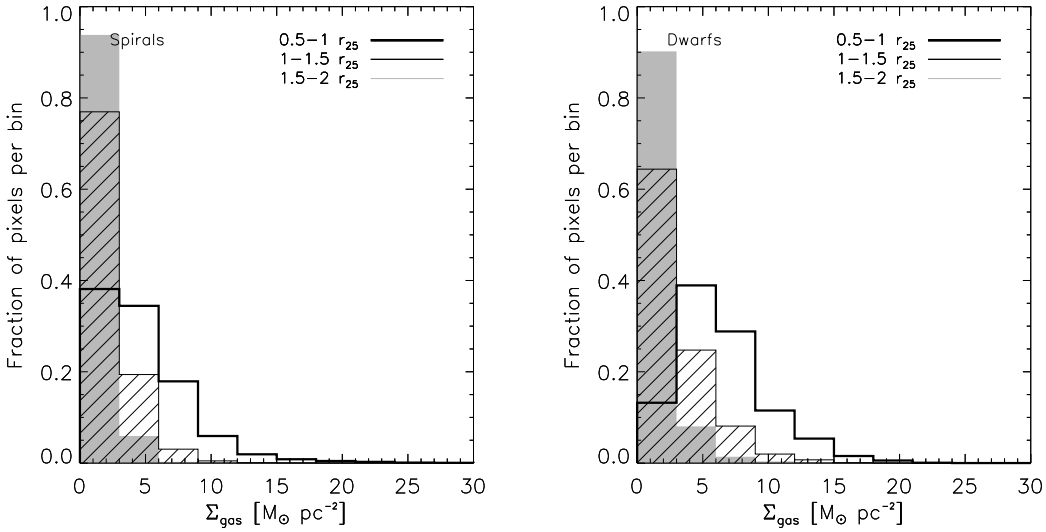

Figure 5.7: The 3 histograms in each panel (left panel: spirals; right panel:dwarfs) show the distribution of number of pixels per $\Sigma_{\rm gas}$ bin for 3 different radial regimes: 0.5 - 1 r_{25} (thick black line), 1 - 1.5 r_{25} (black hashed) and 1.5 - 2 r_{25} (filled grey). One finds that with increasing radius, the fraction of pixels with low $\Sigma_{\rm gas}$ increases strongly at the expense of high $\Sigma_{\rm gas}$ pixels. This is particularly prominent for the dwarfs (right panel).

in the inner radial bin (grey filled) only $\sim$15% of the pixels are in the lowest $\Sigma_{\rm gas}$ bin. This also matches to the radial profiles (see Figure 5.2), where on average $\Sigma_{\rm gas}$ decreases with radius (and has particularly small scalelengths for the dwarfs).

Figure 5.8 shows the SFE plotted against $\Sigma_{\rm gas}$ (the spirals in the left and the dwarfs in the right panel), similarly to the right panel in Figure 5.6. Instead of using data from 1 - 2 r_{25} like in Figure 5.6, we sample pixels from the three radial bins we introduced above: Grey filled circles represent the mean SFE per $\Sigma_{\rm gas}$ bin from 0.5 - 1 r_{25}, black filled circles from 1 - 1.5 r_{25} and black triangles from 1.5 - 2 r_{25}. All other plot parameters, e.g. bin widths and error bars, are like in Figure 5.6. We note that, particularly for the spirals, the data from the inner radial bin (grey circles) may be, to a varying degree and depending on radius, affected by internal extinction. Also, the contribution of the molecular gas to the total gas census becomes increasingly important for pixels that are sampled close to 0.5 r_{25}. For many of the spirals in our sample, see e.g. § 4 or Leroy et al. (2008), we derive average radii between 0.4 and 0.5 r_{25} for which the HI surface density equals the H_2 surface density.

As mentioned earlier, the high gas columns at intermediate radii come mainly from NGC 5457 and NGC 6946. The high gas column densities in the outer disks of these galaxies form stars similarly to high gas columns found in inner disks.

The main conclusion from Figure 5.8 is that in both dwarfs and spirals at intermediate to low $\Sigma_{\rm gas}$, which make up the vast majority of lines of sight in the outer disk, *the galactocentric radius appears absolutely critical in setting the SFE.* This is qualitatively what we found also for the inner disks of galaxies (see § 4, Leroy et al.,

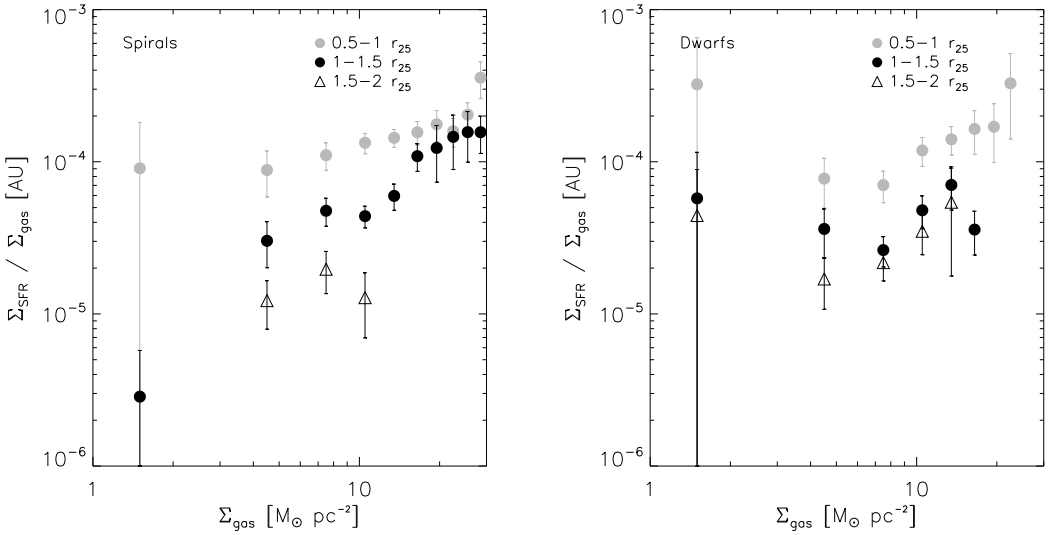

Figure 5.8: The left and right panel show, for the spirals and the dwarfs respectively and similarly to Figure 5.6, the mean values of the SFE per $\Sigma_{\rm gas}$ bin for 3 different radial regimes: Grey filled circles represent data from radii 0.5 - 1 r_{25}, black filled circles from 1 - 1.5 r_{25} and black triangles from 1.5 - 2 r_{25}. The error bars represent the 1σ RMS scatter. The plots show that for all radial regimes the SFE increases with $\Sigma_{\rm gas}$ and that for a given $\Sigma_{\rm gas}$ the galactocentric radius sets the SFE.

2008). The interpretation was that the ability to form star forming clouds out of HI is a sensitive function of environment. As one moves out in the disk, increasing coriolis forces and decreasing interstellar pressure make it more and more inefficient for a given parcel of gas to form stars.

5.3.5 The Star Formation Law in Outer Disks

Based on our work in § 4, which we will refer to as B08 in the following, where we studied the SF law across the optical disks of galaxies on a pixel-by-pixel basis, we use the same approach here to extend these studies into the outer disks. In the case of B08, we extracted individual resolution elements (i.e. independent beams) from the optical disks of 7 nearby spiral galaxies, which are also part of the galaxy sample of this analysis. For this analysis, we sample the outer disks between 1 - 2 r_{25} of our HI and FUV maps. The FUV intensities are converted into SFR surface densities again (see § 5.2). We refer the reader to B08 for a more elaborate description of the sampling procedure. We turn this distribution of sampling points into a 2D density distribution, and the colored contours represent the density of sampling points per cell. Green, orange, red and magenta and black cells represent contour levels of 1, 2, 5, 15 and 40 sampling points per cell respectively. Each cell is 0.05 dex wide in both axes. Individual cells that are not connected and contain only 1 sampling point are grey. Lines of constant gas depletion time, i.e. the inverse of the SFE, are shown as dotted lines and the depletion times associated with each line are given in the plot in units of years. These values include helium and so are true depletion times. The

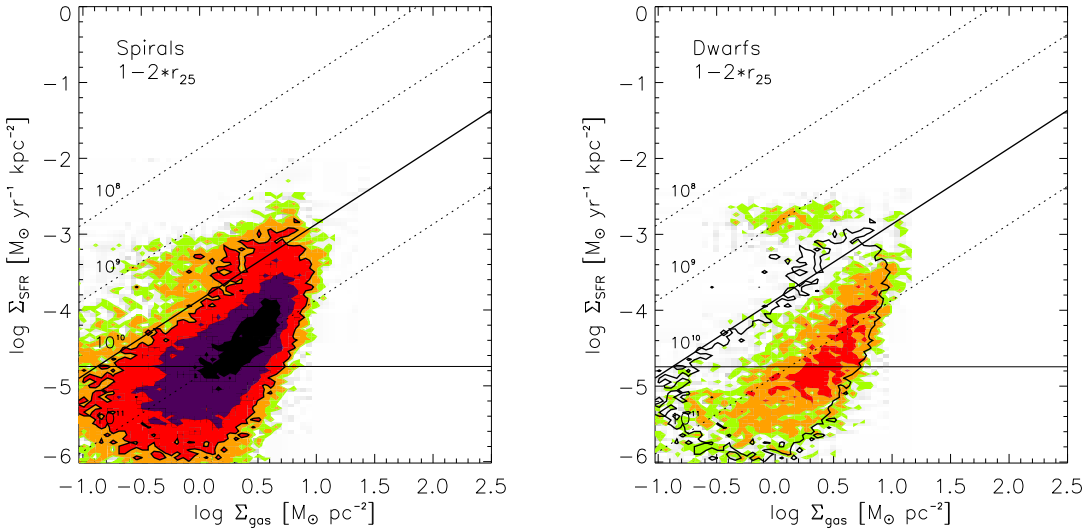

Figure 5.9: We show the results from a pixel-by-pixel analysis of the outer disks (between 1 - 2 r_{25}) of spirals (left panel) and dwarfs (right panel). Displayed is a 2D density plot of Σ_{SFR} versus Σ_{gas}. The colored contours represent the density of sampling points, where green, orange, red and magenta and black cells represent contour levels of 1, 2, 5, 15 and 40 sampling points per cell respectively. The dotted lines show constant gas depletion times, i.e. constant SFEs, of 10^8 to 10^{11} yrs. The horizontal black line indicates the 1σ sensitivity limit on Σ_{SFR}. The thick black line shows an upper envelope to the pixel distribution of the spirals following a line of constant SFE.

horizontal black line indicates the average 1σ sensitivity ($1.8\times10^{-5}\,M_\odot yr^{-1}kpc^{-2}$), which is derived directly from the 1σ sensitivity of the FUV maps (see § 5.2). The average 1σ sensitivity for Σ_{gas} is $0.1\,M_\odot$ pc^{-2} (see2) and coincides with the y-axis. This Σ_{SFR}-Σ_{gas} distribution is shown in the left panel of Figure 5.9 for the spirals and in the right panel for the dwarfs. To be able to compare to the distribution of the spirals, the black contour from the left panel is also shown overplotted on the dwarf distribution in the right panel.

In the distribution for the dwarfs, the cloud of datapoints at rather high Σ_{SFR} of $10^{-3}\,M_\odot yr^{-1}kpc^{-2}$ and above is solely from NGC 1569. These Σ_{SFR} equal the highest values we find for the spirals. Whereas for the spirals these high Σ_{SFR} are associated with rather high Σ_{gas}, NGC 1569 shows such Σ_{SFR} even at relatively low Σ_{gas}. Letting aside NGC 1569, one finds that both distributions are quite similar, i.e. the relationship between Σ_{SFR} and Σ_{gas} in outer galaxy disks does not appear to depend significantly on whether we consider the dwarf or the spiral galaxies in outer sample. The solid black line marks a constant gas depletion time of 10^{10} yrs, which for the spirals in the left panel, also approximately indicates a lower limit on the gas depletion time, i.e. an upper limit on the SFE, for the bulk of the data. In fact, almost all of the data in the left panel at slightly higher SFEs come from only 2 galaxies: NGC 3627 and NGC 6946. The distribution for the dwarfs in the right panel in turn appears to reflect lower SFEs on average,

but the distribution does scatter up to the black line, however. Nevertheless, the mean gas depletion time in the outer disks of the dwarfs (excluding NGC 1569) of 3.9×10^{10} yrs (1σ scatter 6.6×10^{10} yrs) is about a factor of 2 lower than the mean for the spirals (1.8×10^{10} yrs with a 1σ scatter of 4.5×10^{10} yrs). The scatter on both mean depletion times is very large though, which makes them compatible within their errors.

In Figures 5.10 and 5.11, we divide the outer disk between 1 - 2 r_{25} into 4 equally sized radial bins. The four panels show pixel-by-pixel 2D density plots of Σ_{SFR} versus Σ_{gas} for these four radial bins. Otherwise, these plots are identical to Figure 5.9. The black contour shows the distribution of the data between 1 - 2 r_{25} and thus corresponds to the respective black contour in Figure 5.9. Because these are log-log plots, as is Figure 5.9, negative and zero values have to be discarded. In order to assess how many pixels actually pass our sensitivity cuts in the outer disks, i.e. what the numbers of pixels above and below our sensitivity cuts on Σ_{SFR} and Σ_{gas} actually is, and how these numbers vary with radius, we print four numbers in the lower right corner of each plot. The lower left number represents the number of pixels before taking the log below both cuts, the lower right number above the Σ_{gas} but below the Σ_{SFR} cut, the upper right number above both cuts and the upper left number gives the number of pixels below the Σ_{gas} but above the Σ_{SFR} cut.

Considering how the distributions change with increasing radius in Figures 5.10 and 5.11, one finds that for the spirals and the dwarfs likewise, the bulk of data moves towards lower Σ_{SFR} and Σ_{gas}. Also, focussing on the data above our sensitivity cuts (horizontal black line for Σ_{SFR} and the y-axis for Σ_{gas}), the average SFEs become lower for increasing radii. For the spirals, quite surprisingly, the datapoints exhibiting the highest Σ_{SFR} (the 'tip' of the distribution in the upper left panel of Figure 5.10) appear to decrease in Σ_{gas} while remaining relatively constant in Σ_{SFR} with increasing radius. These data are almost exclusively from the outer disks of NGC 3627 and NGC 6946. As opposed to the general trend, this leads to increasing SFEs with increasing radius. For the dwarfs in Figure 5.11, NGC 1569 shows the same behavior (see the cloud of datapoints at high Σ_{SFR}).

Comparing the numbers in the bottom right corner of each plot (describing the numbers of pixels that pass either none, one or both of the sensitivity cuts), one finds for the spirals and the dwarfs likewise that the Σ_{SFR} cut dominates at all radii, i.e. only very few pixels are above the Σ_{SFR} but below the Σ_{gas}. Also, the number of pixels that pass both cuts (in upper right number in all panels) drops quite strongly with radius. While for the spirals in the inner radius bin (upper left plot in Figure 5.10) more than half the pixels are above both cuts, only about 20% pass these cuts in the outermost radial bin (bottom right plot). The situation is quite similar for the dwarfs. Thus, we continue to detect many lines of sight even in the outer disk, but fewer and fewer of them show significant FUV emission.

In order to characterize the relationship between Σ_{SFR} and Σ_{gas} more quantitatively, we fit our data with a power law. We have seen above that a considerable fraction of the pixels from the outer disks do not represent significant measurements (see discussion above and Figures 5.10 and 5.11), which nevertheless have to be included in the fit. We thus fit the radial profile data (see Appendix) instead of the pixel-by-pixel data, to make use of the increased sensitivity from radial binning, and

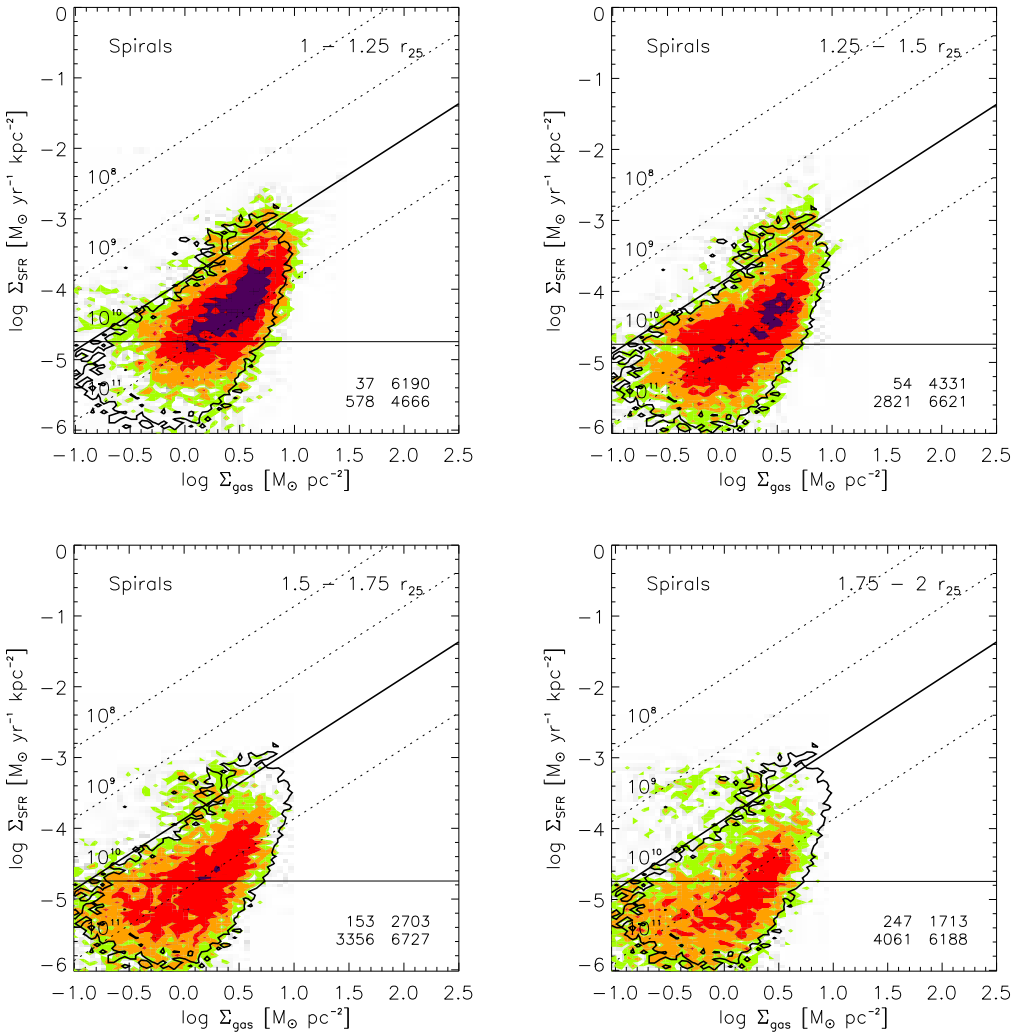

Figure 5.10: Similarly to the left panel in Figure 5.9, the four panels show pixel-by-pixel 2D density plots for Σ_{SFR} versus Σ_{gas} for the spiral galaxies. The four panels display data from four radial bins: 1 - 1.25, 1.25 - 1.5, 1.5 - 1.75 and 1.75 - 2 r_{25}. All other plot parameters are identical to Figure 5.9. The four numbers in the bottom right corner indicate the number of pixels that pass either one, both or none of the sensitivity cuts on Σ_{SFR} and Σ_{gas} (see text for more details). The distributions in the different panels show that, on average, the SFE decreases with radius and that the number of pixels representing significant measurements decreases strongly with radius as well.

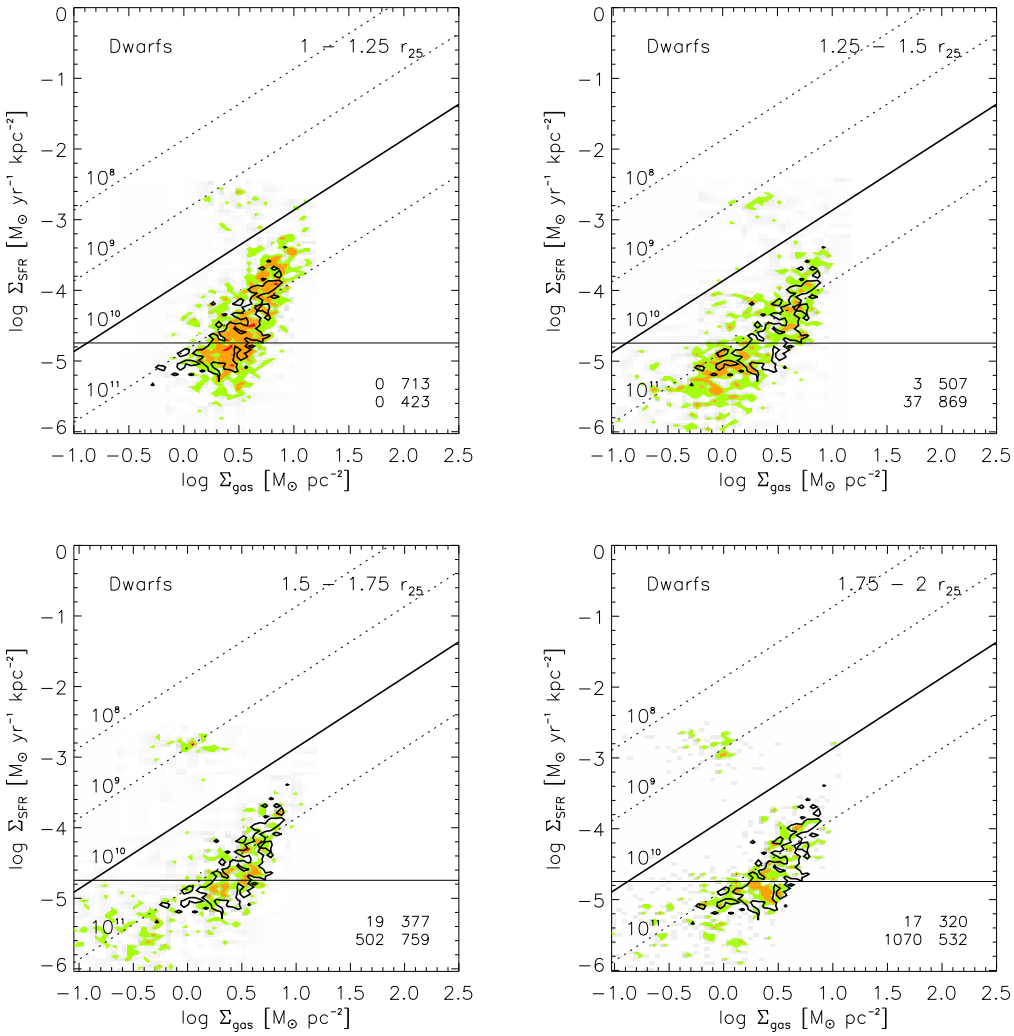

Figure 5.11: Shown are pixel-by-pixel 2D density plots for Σ_{SFR} versus Σ_{gas} for the dwarf galaxies. The four panels represent four different radial bins between 1 - 2 r_{25} the data was sampled in. See Figures 5.10 and 5.9 for more details on the plots.

furthermore restrict our fit to the regime $\Sigma_{gas} > 1\,M_\odot$ pc^{-2}, which ensures that a large fraction of the radial profile datapoints represent significant measurements. Figure 5.12 shows the fitted data along with the obtained power-law fit. The colored contours and all other plot parameters in both panels are identical to the respective panels in Figure 5.9 (i.e. pixel-by-pixel outer disk data from 1 - 2 r_{25} for the spirals in the left panel and for the dwarfs in the right panel). Each overplotted black circle represents a tilted ring averaged mean from the radial profiles. Only radial profile datapoints above $\Sigma_{gas} = 1\,M_\odot$ pc^{-2} are shown. The power-law fit (i.e. the OLS bisector fit in log-log space) to these datapoints is indicated by the black line. We obtain a power-law index of 2.42 ± 0.46 for the spirals and 2.38 ± 0.15 for the dwarfs (excluding NGC 1569 which is also not shown in the plot). We also fit the data in several other ways, like directly fitting the pixel-by-pixel data in linear space by a power-law or binning the data according to Σ_{gas} and fitting by power-law. All methods yield consistent power-law indices between 2.3 and 2.9, strongly indicating a non-linear relationship between Σ_{SFR} and Σ_{gas}. This matches to our previous observations in § 5.3.2 and § 5.3.4 that the SFE is roughly linearly proportional to Σ_{gas} in the outer disks of spirals and dwarfs.

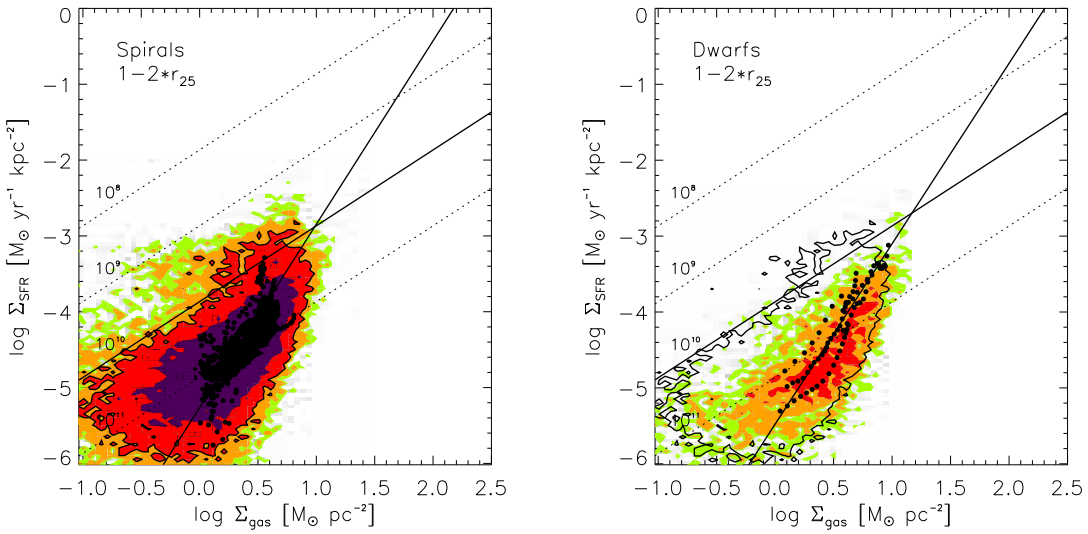

Figure 5.12: Shown are the pixel-by-pixel 2D density distributions of Σ_{SFR} versus Σ_{gas} between 1 - 2 r_{25} (for the spirals in the left panel, for the dwarfs in the right panel). Plot parameters and colored contours in both panels are identical to the respective panels in Figure 5.9. Overplotted as black circles are datapoints from the radial profiles (see Appendix) above $\Sigma_{gas} > 1\,M_\odot$ pc^{-2}. These data are fit by a power-law which yields an index of ∼2.4 for the spirals and the dwarfs. The fit is indicated by the black line.

5.3.6 Comparison to Measurements from inside r_{25}

In the following we compare the pixel-by-pixel 2D distribution from the outer disks of spirals, i.e. between 1 - 2 r_{25}, to data from B08. We sampled the optical disks, i.e. within r_{25}, pixel-by-pixel for 7 nearby spirals which are also part of our sample. The left panel in Figure 5.13 shows this distribution from B08 (their Figure 8). In the left panel, green, orange, red and magenta cells represent contour levels of 1, 2, 5 and 10 sampling points per cell respectively. In the right panel of Figure 5.13, we show the new data from the outer disks (from all 19 spirals in our sample) combined with the optical disk data from B08 (comprising 7 spirals). Green, orange, red, magenta and black cells represent contour levels of 1, 2, 5, 15 and 40 sampling points per cell respectively (like in the previous figures). The black contour is identical in both panels and indicates the distribution of sampling points from within the optical disks. All other plot parameters are identical to the previous figures.

We note that for the analysis in B08, Σ_{SFR} was derived using a combination of FUV emission, to trace SF unobscured by dust, and 24 μm emission from *Spitzer*, to trace SF obscured by dust, i.e. to correct for internal extinction. Σ_{SFR} in this paper is in turn based solely on FUV emission, because, as indicated in § 5.2.1, internal extinction appears negligible in the outer disks on average.

Looking at the combined distribution in the right panel, one finds a smooth continuation of the distribution that was obtained within r_{25} (black contour) towards lower

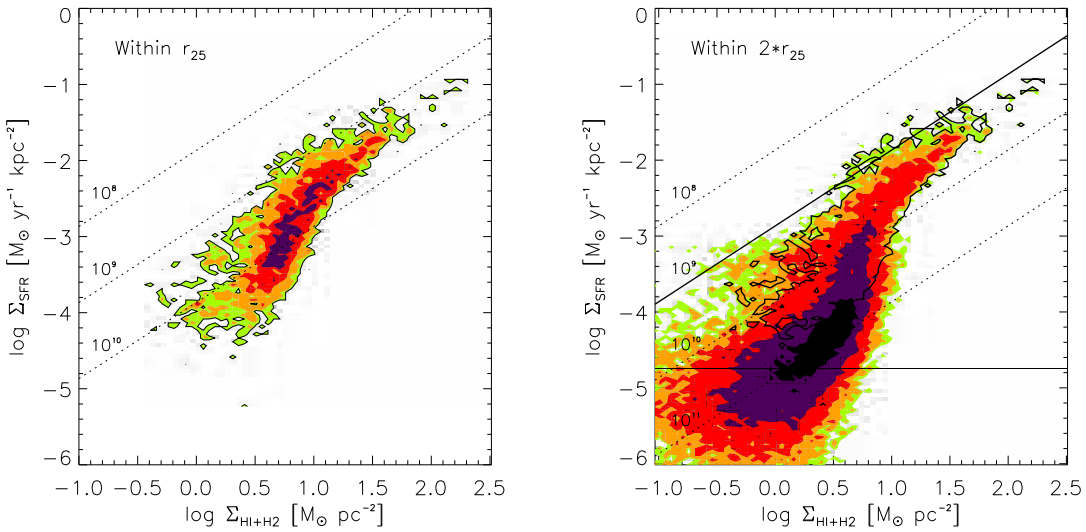

Figure 5.13: The left panel shows the pixel-by-pixel 2D distribution obtained from the optical disks (i.e. within r_{25}) of 7 spiral galaxies that are also part of the sample of this paper (Figure 8 in B08). The right panel shows these optical disk data combined with the outer disk data from Figure 5.9. For further details on the plots see the text or Figure 5.9. The black line indicates an upper limit on the SFE, i.e. a lower limit on the gas depletion time of $\sim 10^9$ yrs, that seems to hold for both distributions, i.e. from the centers of spirals out to 2 r_{25}.

Σ_{gas} and Σ_{SFR} in the outer disks. In B08, we identified 2 distinctly different regimes: At low Σ_{gas}, up to about $10\,M_\odot$ pc^{-2}, the hydrogen gas is mostly atomic and the distribution of sampling points for the *atomic* gas saturates at this value; above this 'threshold', the hydrogen gas is mostly molecular and the pixel distribution for the molecular gas follows a power-law with a slope 1.0 ± 0.2, i.e. Σ_{SFR} is proportional to Σ_{H2} in this regime.

Including the new data from the outer galaxy disks, and following the distribution down to the lowest Σ_{gas}, one finds that, despite strongly increasing scatter, the combined distribution may resemble an 'S-like shape'. Quite unfortunately, most of these data are below our sensitivity cut for Σ_{SFR} and thus not significant.

Above, we found that the bulk of the pixel-by-pixel distribution of the outer disk data shows gas depletion times below $\sim 10^{10}$ yrs, but that depletion times scatter down to $\sim 10^{9}$ yrs (compare Figure 5.9). The right panel in Figure 5.13 shows that a gas depletion time of $\sim 10^{9}$ yrs appears to be indeed a good description of a lower limit for depletion times, i.e. an upper limit on the SFEs, not only in the outer disks, but also within r_{25}. Even though the average depletion times in the outer disks are longer as compared to the optical disks, the lower limit of $\sim 10^{9}$ yrs appears to be relatively universal from the centers of spirals out to $2\,r_{25}$.

To assess the SFEs not only in the outer disks of dwarfs (see right panel of Figure 5.9), but also in the inner parts, we sample the regime within r_{25} pixel-by-pixel and combine these data with the outer disk data from figure 5.9. We note that

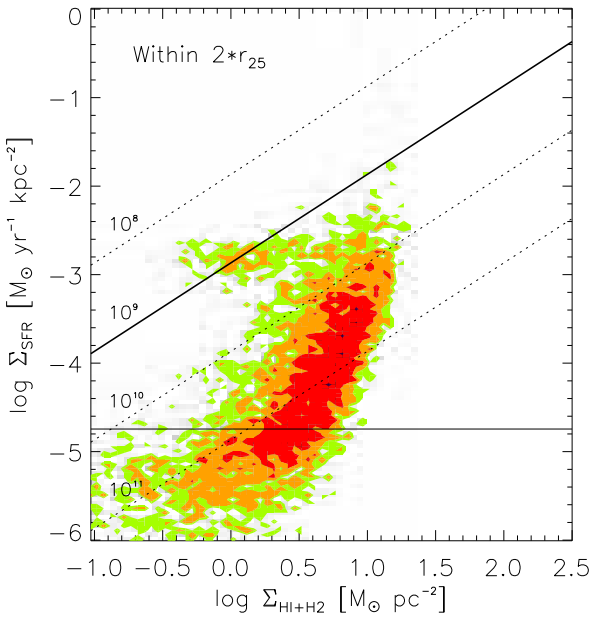

Figure 5.14: Displayed is the pixel-by-pixel 2D distribution between the centers and $2\,r_{25}$ for the dwarfs in our sample. See the previous figures for further details to the plot parameters. Like the distribution for the spirals over the same radial range (compare the right panel of Figure5.13), the distribution for the dwarfs shows the same upper limit on the SFE (indicated by the black line).

these new data are not corrected for internal extinction. Figure 5.14 shows the combined distribution. All plot parameters, like e.g. contour levels, are identical to the previous plots.

The plot shows that, apart from the datapoints from NGC 1569, the same upper limit on the SFEs that was found across the optical and outer disks of the spirals apparently holds across the optical disks of the dwarfs as well. One finds that the SFEs scatter almost as high in the dwarfs as in the spirals, but the bulk of the data lies clearly at significantly lower average SFEs than in the spirals.

5.4 Summary & Discussion

From sensitive maps of HI from THINGS and FUV from GALEX we study the relationship between gas and star formation in the outer disks of galaxies in several ways. Both decline radially. The FUV radial profile declines significantly steeper than the HI profile. We quantify this by fitting exponentials to the declining parts of the radial profiles and find that on average the HI scalelength is four times larger than the FUV scalelength, so that the ratio of FUV to HI is decreasing steadily with increasing radius. Equivalently, the star formation efficiency, i.e. the SFR per unit gas, declines with increasing radius.

We furthermore examine how HI and FUV emission correlate at a given radius using the rank correlation coefficient. Around the edge of the optical disk (r_{25}), HI and FUV emission are strongly correlated. In this radial regime, internal extinction is small, HI dominates the ISM and THINGS and GALEX maps detect significant emission for most lines of sight. Towards smaller radii, the correlation becomes weaker and less significant. This is due to a combination of an increasing fraction of gas in the molecular phase and differential extinction affecting the FUV within a radial bin. The correlation also becomes weaker as radius increases outside of r_{25}. This is probably due to a decreasing fraction of lines of sight having significant FUV emission.

In the outer disk, we look at how the SFE, traced by the ratio of FUV to HI emission, varies as a function of HI column and radius. The majority of lines of sight in the outer disk have HI columns below $3\,M_\odot\ pc^{-2}$ and very low SFEs, much lower than lines of sight in the subsequent bin (3-6 $M_\odot\ pc^{-2}$) and above. The simplest interpretation is that at these low HI columns conditions in the ISM are hostile to the formation of gravitationally bound, star forming clouds. A power-law fit to data with surface densities above $3\,M_\odot\ pc^{-2}$ yields SFE$\sim \Sigma_{HI}$. Comparing the SFEs in bins with the same HI column at different radii, we observe a strong dependence with SFE on galactocentric radius. We interpret this as evidence that quantities covariant with galactocentric radius exert a strong influence on the ability of the ISM to form star forming clouds. This qualitatively confirms that the steadily declining SFE as a function of radius that we observed in § 4 and Leroy et al. (2008) for the optical disks continues out to large galactocentric radii.

Eventually, we study the pixel-by-pixel distribution of FUV intensity versus HI column. Combining radial profile, pixel-by-pixel and binned data, we derive a power-law index between 2 and 3 relating FUV intensity and HI column between 1 and

$2\,r_{25}$. We show that the pixel-by-pixel distribution of the outer disk is a smooth extension of what we observed in the inner disk. We find a typical HI depletion time of $\sim 2 \times 10^{10}$ yrs for the outer disks, i.e. about a Hubble time. We see the same sort of radial dependence of the SFE in the pixel-by-pixel data that we saw in the binned data.

Co-Investigators on this project are:
Adam Leroy (MPIA), Fabian Walter (MPIA) et al.

Chapter 6

Summary

Previous studies on the star formation law in nearby galaxies, using almost exclusively integrated measurements over whole galaxy disks or radial profiles, derived a diverse range of scaling relations between gas and star formation surface densities ($\Sigma_{\rm SFR}$ and $\Sigma_{\rm gas}$ respectively). In order to systematically assess this relationship *spatially resolved*, i.e. by pixel-by-pixel sampling the optical disks *and* the outer disks of a large sample of nearby starforming galaxies at unprecedented resolution, high resolution and very sensitive HI data from THINGS, CO data from IRAM and BIMA, 24 μm data from the *Spitzer* Space Telescope, and UV data from GALEX are combined. The analyses presented in this thesis thus assess the questions of how the star formation law differs between the H_2 dominated centers of spiral galaxies, their HI dominated outskirts and HI rich late type/dwarf galaxies.

The following key results were obtained in this work:

- A Schmidt-type power-law with index N=1.0±0.2 relates the star formation rate surface density and the H_2 surface density across the optical disks of the spiral galaxies.

- Most galaxies show only little or no correlation between the HI and the star formation rate surface density within the optical disks. This, and the fact that there is excellent agreement between star formation and H_2 leads to the conclusion that the star formation law is a molecular gas law within $\sim r_{25}$. This addresses directly one of the open key questions of star formation in other galaxies.

- These results hold for a pixel-by-pixel analysis as well as for radial profiles using several different star formation tracers and on spatial scales from 300 pc to more than 1 kpc. This implies that H_2 forms stars with nearly constant efficiency in the optical disks of spirals. An average gas depletion time of $\sim 2\times10^9$ yrs is derived for the molecular gas.

- The relationship between $\Sigma_{\rm SFR}$ and $\Sigma_{\rm gas}$, and therefore also the star formation efficiency $\Sigma_{\rm SFR}/\Sigma_{\rm gas}$ (SFE), varies dramatically within the optical disks of individual galaxies. It could be shown that this variation is a strong function of environment: In spirals the SFE is a clear function of galactocentric radius,

while dwarf galaxies show the same (low) SFEs as the outer edges of the optical disks of spirals.

- Within r_{25}, the HI surface density shows a sharp saturation at $\sim$9 $M_\odot$ pc^{-2} in every system. Gas in excess of this limit is observed to be molecular. Despite very different properties of the ISM (e.g. metallicity), the same saturation level is observed in dwarfs and spirals.

- In the outer disks (i.e. between 1 and $2\,r_{25}$) of 26 nearby galaxies, the HI scalelength is found to be four times larger than the FUV scalelength, so that the ratio of FUV to HI (and thus the SFE) is decreasing steadily with increasing radius.

- Below an HI surface density of $\sim$3 $M_\odot$ pc^{-2}, most lines of sight have extremely low SFEs. At higher surface densities, the SFEs increases strongly. A likely interpretation is that gas at low column densities inhibits star formation in outer disks.

- For higher gas columns than $\sim$3 $M_\odot$ pc^{-2}, the SFE is a strong function of galactocentric radius in the outer disks: the SFE is observed to decrease with increasing radius. This implies that the SFE continues its trend to decrease with radius from the outer parts of the optical disk (see above) to much larger radii.

- Around the edge of the optical disk, HI and FUV emission are strongly correlated. This correlation becomes weaker with increasing radius, most likely because the number of lines of sight with significant FUV emission decreases.

- The pixel-by-pixel distribution of the outer disks is found to be a smooth extension towards lower $\Sigma_{\rm gas}$ and $\Sigma_{\rm SFR}$ of what was observed for the pixel-by-pixel distribution of the optical disks. An average outer disk HI depletion time of $\sim 2 \times 10^{10}$ yrs was derived, which corresponds to about a Hubble time.

Chapter 7

Outlook

The analyses in this thesis explored a reasonable fraction of the gas-SFR phase space covered by normal starforming galaxies. By using very sensitive state-of-the-art data and extending these investigations from the optical disks (see § 4) into the outer disks of galaxies (see § 5), the relation between gas and SF in a much larger regime of this phase space could be studied. Thus, it seems as a natural consequence to fill the remaining gaps of phase space, which are either not populated with data at all or only populated with low resolution data, like measurements integrating over whole galaxies. Filling these 'blank regions', where 'blank' refers to the lack of spatially resolved data, of the gas-SFR phase space requires high-resolution observations of starburst galaxies, LIRGs and ULIRGs on the one hand, and very high sensitivity measurements of the extremely extended outer disks of galaxies on the other hand (compare Figure 7.2 below). Studying the SF law in such distinctly different environments will allow to clarify the dominant role of environment in the SF process in galaxies and allow *for the first time* to assess the SF law spatially resolved over many orders of magnitude in gas and SFR surface densities.

7.1 Star Formation in the Outskirts of Galaxies

The outer edges of galaxies allow to probe the SF law in an environment that is distinctly different from the inner/optical disks of galaxies (see § 5). This analysis was limited mainly by the sensitivity of the UV maps. To push to significantly lower SFRs, much more sensitive UV observations are required. For that purpose, a GALEX program was initiated (PI: F. Bigiel) to obtain UV observations at unprecedented depth (10 times more integration time than the 'standard' observations in the 'GALEX Nearby Galaxy Survey', NGS, Gil de Paz et al., 2007). This program is currently observed, and observations for one target galaxy, M 83, were completed just recently. The right panel in Figure 7.1 shows *for the first time the deepest GALEX Far UV (FUV) image for NGC 5236 (M83) ever taken.* The FUV image reveals a stunning amount of extremely extended star formation far away from the optical disk of the galaxy (the two overplotted annuli indicate distances of r_{25} and $3 \times r_{25}$). Also, the FUV emission appears highly correlated with the HI as indicated by the overplotted contours in the right panel (also see the left panel for the full THINGS HI image).

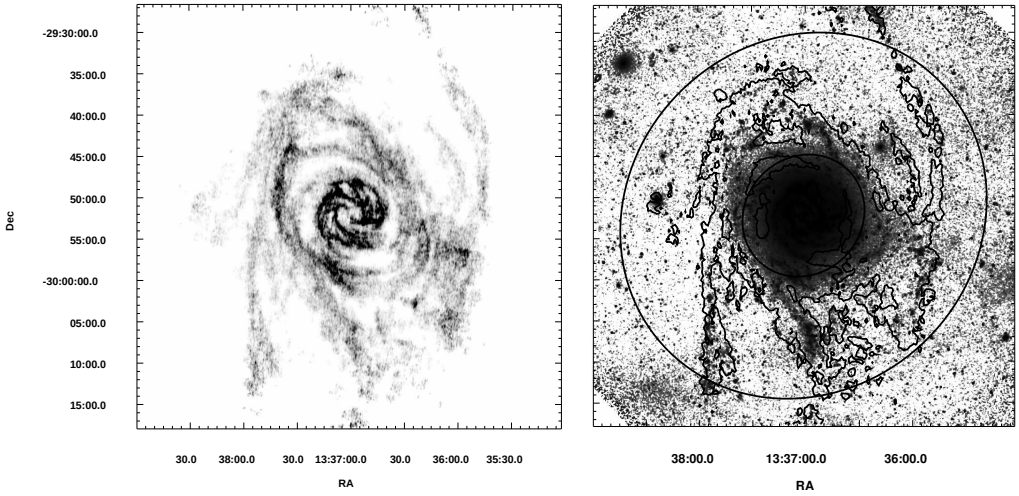

Figure 7.1: The left panel shows the THINGS HI intensity map for NGC 5236(M83). The right panel shows *for the first time* the just recently completed extremely deep GALEX FUV map (unpublished, PI: F. Bigiel). Overplotted is an HI contour of 5×10^{19}cm^{-2}. The two ellipses represent projected galactocentric distances of r_{25} (optical radius) and $3\times r_{25}$. One recognizes extended star formation across the entire field and an extremely tight correlation of the FUV and the HI. Particularly striking is the SF region in the north-west (at the tip of the western 'HI arm') at a galactocentric distance of more than 3 optical radii.

Ultimately, in order to study star forming regions in the extremely outer disks directly, very sensitive and very high-resolution observations of molecular gas in the outskirts of galaxies need to be obtained as well. This can be done with millimeter radio interferometers, like e.g. CARMA or the IRAM Plateau de Bure interferometer. Zooming in on individual star forming regions in the very extended UV disks will allow to assess the conditions of the ISM and the processes leading to SF in such extreme environments.

7.2 The Star Formation Law in Starbursts and (U)LIRGs

On the more extreme side of galaxy activity, studying the spatially resolved SF law in starburst galaxies is another logical next step. Figure 7.2 shows the necessity of such studies more quantitatively. Shown is a key result from this thesis: the result of the pixel-by-pixel analysis for 26 nearby (normal star forming) spiral galaxies (colored contours) at sub-kpc resolution. Overplotted are data points from Kennicutt (1998, see Figure 6). The latter data represent integrated measurements across the optical disks of normal starforming galaxies and across the central molecular disks of starburst galaxies. Every datapoint thus represents one galaxy (filled circles: spirals, filled squares: starburst galaxies).

It is obvious from Figure 7.2, that a significant part of the critical Σ_{SFR}–Σ_{gas} phase

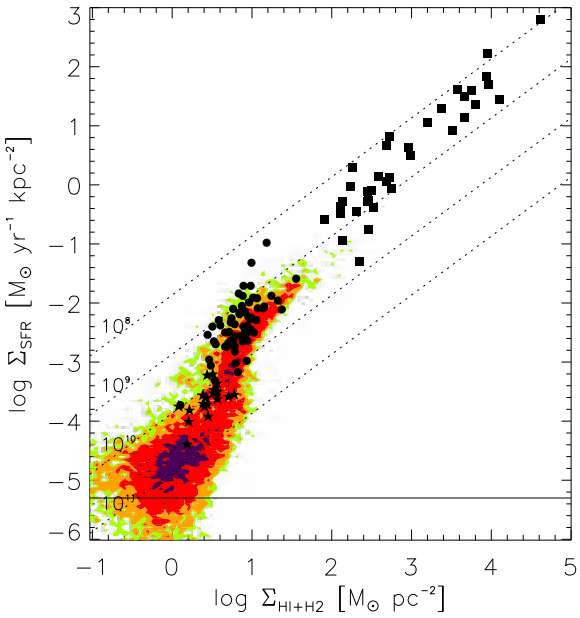

Figure 7.2: Shown are contour plots for Σ_{SFR} versus $\Sigma_{gas} = \Sigma_{HI+H2}$ of the pixel-by-pixel analysis of 26 nearby galaxies from this thesis. The overplotted stars indicate integrated measurements from low surface brightness galaxies (Wyder et al., 2007). Overplotted are furthermore data points from Kennicutt (1998, compare their Figure 6). Each data point represents an integrated measurement across the optical disk (across the central molecular disk for starburst galaxies respectively) of an individual galaxy (Filled circles: spirals, filled squares: starburst galaxies). The figure illustrates the need for spatially resolved data in the high gas column and high SFR regime to constrain properties of the SF law for starburst galaxies and ULIRGs.

space corresponding to very high gas columns and SFRs is not populated with resolved data yet. In the light of discoveries of extremely dust and gas rich maximally star forming populations of submillimeter galaxies at high redshifts (e.g. Tacconi et al., 2006; Bouché et al., 2007) and gas detections in quasar host galaxies at extremely high redshifts (e.g. Walter et al., 2003), extending studies of the resolved SF law to progressively higher SFRs and gas columns appears indispensable and comes as a natural consequence of the work presented in this thesis. Such studies would for the first time systematically assess the SF law in an environment that is distinctly different from normal star forming galaxies and that is of great importance for interpreting observations at high redshift. Furthermore, such observations would lay the foundation for future observations with the millimeter interferometer ALMA. Its superior resolution and sensitivity will allow to study the relation between gas and star formation on a spatially resolved basis out to the earliest epochs.

Bibliography

Blitz, L. 1993, Protostars and Planets III, 125

Blitz, L., Fukui, Y., Kawamura, A., Leroy, A., Mizuno, N., & Rosolowsky, E. 2007, Protostars and Planets V, 81

Bohlin, R. C., Savage, B. D., & Drake, J. F. 1978, ApJ, 224, 132

Bouché, N., et al. 2007, ApJ, 671, 303

Boissier, S., & Prantzos, N. 1999, MNRAS, 307, 857

Boissier, S., Prantzos, N., Boselli, A., & Gavazzi, G. 2003, MNRAS, 346, 1215

Boissier, S., et al. 2007, ApJS, 173, 524

Boselli, A., Gavazzi, G., Lequeux, J., Buat, V., Casoli, F., Dickey, J., & Donas, J. 1995, A&A, 300, L13

Braine, J., Combes, F., Casoli, F., Dupraz, C., Gerin, M., Klein, U., Wielebinski, R., & Brouillet, N. 1993, A&AS, 97, 887

Braine, J., & Herpin, F. 2004, NATURE, 432, 369

Braine, J., Ferguson, A. M. N., Bertoldi, F., & Wilson, C. D. 2007, ApJL, 669, L73

Braun, R. 1995, A&AS, 114, 409

Briggs, D. 1995, Ph.D. thesis, New Mexico Institute of Mining and Technology

Brinks, E., & Bajaja, E. 1986, A&A, 169, 14

Buat, V., Deharveng, J. M., & Donas, J. 1989, A&A, 223, 42

Buat, V. 1992, A&A, 264, 444

Calzetti, D., Kinney, A. L., & Storchi-Bergmann, T. 1994, ApJ, 429, 582

Calzetti, D., et al. 2005, ApJ, 633, 871

Calzetti, D., et al. 2007, ApJ, 666, 870

Cardelli, J. A., Clayton, G. C., & Mathis, J. S. 1989, ApJ, 345, 245

Chabrier, G. 2003, PASP, 115, 763

Crosthwaite, L. P., & Turner, J. L. 2007, AJ, 134, 1827

Cuillandre, J.-C., Lequeux, J., Allen, R. J., Mellier, Y., & Bertin, E. 2001, ApJ, 554, 190

Daddi, E., Dannerbauer, H., Elbaz, D., Dickinson, M., Morrison, G., Stern, D., & Ravindranath, S. 2008, ApJL, 673, L21

Dame, T. M., Hartmann, D., & Thaddeus, P. 2001, ApJ, 547, 792

de Blok, W. J. G., & Walter, F. 2003, MNRAS, 341, L39

Deharveng, J.-M., Sasseen, T. P., Buat, V., Bowyer, S., Lampton, M., & Wu, X. 1994, A&A, 289, 715

de Vaucouleurs, G., et al. 1991, Springer, Volume 1-3, XII, 2069

Erwin, P., Beckman, J. E., & Pohlen, M. 2005, ApJL, 626, L81

Ewen, H. I., & Purcell, E. M. 1951, NATURE, 168, 356

Federman, S. R., Glassgold, A. E., & Kwan, J. 1979, ApJ, 227, 466

Ferguson, A. M. N., Wyse, R. F. G., Gallagher, J. S., & Hunter, D. A. 1998, ApJL, 506, L19

Gardan, E., Braine, J., Schuster, K. F., Brouillet, N., & Sievers, A. 2007, A&A, 473, 91

Gao, Y., & Solomon, P. M. 2004, ApJ, 606, 271

Gil de Paz, A., et al. 2005, ApJL, 627, L29

Gil de Paz, A., et al. 2007, ApJS, 173, 185

Gil de Paz, A., et al. 2007, ApJ, 661, 115

Gordon, K. D., et al. 2005, PASP, 177, 503

Greve, T. R., et al. 2005, MNRAS, 359, 1165

Hamajima, K., & Tosa, M. 1975, PASJ, 27, 561

Hartwick, F. D. A. 1971, ApJ, 163, 431

Helfer, T. T., Thornley, M. D., Regan, M. W., Wong, T., Sheth, K., Vogel, S. N., Blitz, L., & Bock, D. C.-J. 2003, ApJS, 145, 259

Heyer, M. H., Corbelli, E., Schneider, S. E., & Young, J. S. 2004, ApJ, 602, 723

Högbom, J. A. 1974, A&AS, 15, 417

Hunter, D. A., Elmegreen, B. G., & Baker, A. L. 1998, ApJ, 493, 595

Isobe, T., Feigelson, E. D., Akritas, M. G., & Babu, G. J. 1990, ApJ, 364, 104

Jorsater, S., & van Moorsel, G. A. 1995, AJ, 110, 2037

Kamphuis, J., Sancisi, R., & van der Hulst, T. 1991, A&A, 244, L29

Karachentsev, I. D., et al. 2002, A&A, 383, 125

Karachentsev, I. D., et al. 2003, A&A, 398, 479

Kennicutt, R. C. 1989, ApJ, 344, 685

Kennicutt, R. C. 1998, ApJ, 498, 541

Kennicutt, R. C., Jr. 1998, ARA&A, 36, 189

Kennicutt, R. C., Jr., et al. 2003, PASP, 115, 928

Kennicutt, R. C., Jr., et al. 2007, ApJ, 671, 333

Kim, S., Dopita, M. A., Staveley-Smith, L., & Bessell, M. S. 1999, AJ, 118, 2797

Kroupa, P., 2001, MNRAS, 322, 231

Krumholz, M. R., & McKee, C. F. 2005, ApJ, 630, 250

Krumholz, M. R., & Thompson, T. A. 2007, ApJ, 669, 289

Lee, J. C., 2006, PhD Thesis, University of Arizona

Leitherer, C., et al. 1999, ApJS, 123, 3

Lelièvre, M., & Roy, J.-R. 2000, AJ, 120, 1306

Leroy, A., Bolatto, A. D., Simon, J. D., & Blitz, L. 2005, ApJ, 625, 763

Leroy, A., et al. 2008, AJ, submitted

Madore, B. F., van den Bergh, S., & Rogstad, D. H. 1974, ApJ, 191, 317

Madore, B. F. 1977, MNRAS, 178, 1

Martin, C. L., & Kennicutt, R. C., Jr. 2001, ApJ, 555, 301

Matteucci, F., Panagia, N., Pipino, A., Mannucci, F., Recchi, S., & Della Valle, M. 2006, MNRAS, 372, 265

Misiriotis, A., Xilouris, E. M., Papamastorakis, J., Boumis, P., & Goudis, C. D. 2006, A&A, 459, 113

Morrissey, P., et al. 2005, ApJ, 619, L7

Moustakas, J., et al. 2006, ApJ, 651, 155

Newton, K. 1980, MNRAS, 190, 689

Pérez-González, P. G., et al. 2006, ApJ, 648, 987

Pohlen, M., Dettmar, R.-J., Lütticke, R., & Aronica, G. 2002, A&A, 392, 807

Pohlen, M., & Trujillo, I. 2006, A&A, 454, 759

Popescu, C. C., & Tuffs, R. J. 2003, A&A, 410, L21

Prugniel, P. & Heraudeau, P. 1998, A&AS, 128, 299

Riechers, D. A., Walter, F., Carilli, C. L., & Bertoldi, F. 2007, ApJL, 671, L13

Rieke, G., et al. 2004, ApJS, 154, 25

Rohlfs, K., & Wilson, T. L. 1996, Tools of Radio Astronomy (Springer)

Rosolowsky, E., & Blitz, L. 2005, ApJ, 623, 826

Roussel, H., Gil de Paz, A., Seibert, M., Helou, G., Madore, B. F., & Martin, C. 2005, ApJ, 632, 227

Salim, S., et al. 2007, ApJS, 173, 267

Salpeter, E. E., 1955, ApJ, 121, 161

Sanduleak, N. 1969, AJ, 74, 47

Schaye, J. 2004, ApJ, 609, 667

Schlegel, D. J., Finkbeiner, D. P. & Davis, M. 1998, ApJ, 500, 525

Schmidt, M. 1959, ApJ, 129, 243

Schuster, K.-F., et al. 2004, A&A, 423, 1171

Schuster, K. F., Kramer, C., Hitschfeld, M., Garcia-Burillo, S., & Mookerjea, B. 2007, A&A, 461, 143

Skaya, E. J., & Federman, S. R. 1987, ApJ, 319, 76

Solomon, P. M., Rivolo, A. R., Barrett, J., & Yahil, A. 1987, ApJ, 319, 730

Spitzer, L. 1978, Physical Processes in the Interstellar Medium (Wiley and Sons)

Springel, V., & Hernquist, L. 2003, MNRAS, 339, 289

Staveley-Smith, L., Sault, R. J., Hatzidimitriou, D., Kesteven, M. J., & McConnell, D. 1997, MNRAS, 289, 225

Strong, A. W., & Mattox, J. R. 1996, A&A, 308, L21

Swaters, R. A., van Albada, T. S., van der Hulst, J. M., & Sancisi, R. 2002, A&A, 390, 829

Tacconi, L. J., et al. 2006, ApJ, 640, 228

Tamburro, D., et al. 2008, AJ, submitted

Tan, J. C., Silk, J., & Balland, C. 1999, ApJ, 522, 579

Taylor, C. L., Kobulnicky, H. A., & Skillman, E. D. 1998, AJ, 116, 2746

Thilker, D. A., et al. 2005, ApJL, 619, L79

Thilker, D. A., et al. 2007, ApJS, 173, 538

Thornley, M. D., & Wilson, C. D. 1995, ApJ, 447, 616

Tosa, M., & Hamajima, K. 1975, PASJ, 27, 501

Van de Hulst, H. C. 1945, Ned. Tijdschr. Natuurk., 11, 210

Walter, F., & Brinks, E. 1999, AJ, 118, 273

Walter, F., Taylor, C. L., Hüttemeister, S., Scoville, N., & McIntyre, V. 2001, AJ, 121, 727

Walter, F., et al. 2003, NATURE, 424, 406

Walter, F. 2008, AJ, submitted

Wilson, C. D. 1995, ApJL, 448, L97

Wong, T. & Blitz, L. 2002, ApJ, 569, 157

Wyder, T. K., et al. 2007, ApJS, 173, 293

Young, J. S., et al. 1995, ApJS, 98, 219

Acknowledgments

The last page of this thesis is dedicated to all the people who contributed to the successful completion of this thesis. I would like to mention in particular

- Fabian Walter, for offering me the opportunity to work on exciting and interesting THINGS (seemed like the right spot for one final THINGS pun ...). His support (in many ways!) exceeded all my expectations. The atmosphere in our group was just great, and I had fantastic 3 years at the MPIA. I couldn't have wished for a better advisor! I can only imagine what it is like to supervise a student who gets really everything done super last-minute for 3 years. Believe it or not, these times are gone!

- Adam 'IDL' Leroy, whose encyclopedic IDL and ISM wisdom made most of the results in this thesis possible. I don't know what my thesis would have looked like without his help!

- Elias Brinks for his help and many very useful comments, telephone conferences and emails on many thesis related issues at various day and night times. I'm more than ever convinced that you don't sleep ...

- Erwin de Blok for his support with my thesis work and for introducing me to (some of) the secrets of deriving galaxy rotation curves and for his hospitality in Canberra. I still can't believe you refused to drink that last Sambuca!

- Ralf Klessen, who provided me with theoretical background for my work and agreed to referee this thesis on very short timescales.

- Barry Madore for many useful discussions and comments regarding my thesis work and for his hospitality during my visit to Pasadena and the great time at Las Campanas.

- Leo Blitz for his support and his hospitality at Berkeley.

- John Cannon, who was a great help getting me startet ...

- meine gesamte Familie. Ohne Eure Unterstützung über die vielen Jahre wäre sicher nichts von all dem möglich gewesen. Den beruflichen Weg einschlagen zu dürfen der mir am meisten Freude bereitet ist ein grosses Privileg, das Ihr mir ermöglicht habt. Vielen Dank!